Theoretical Interpretation of Scanning Probe Microscopy Images Involving Organic Molecules

Andrew J. Lakin

The University of Nottingham

Thesis submitted to the University of Nottingham
for the degree of Doctor of Philosophy, March 2014

Abstract

Scanning probe microscopy allows the investigation and manipulation of matter at the atomic and molecular level, and is crucial in the development of new and novel techniques within nanoscience. However, to understand the information obtained from the various forms of scanning probe microscopy, a thorough theoretical understanding is necessary. Often this theoretical background is provided through density functional theory, which, while incredibly powerful, has limitations with regards to the size and complexity of the systems in which it can investigate. Thus, for more complicated systems, alternative techniques are desirable to be used both independently and alongside density functional theory.

In this work, theoretical techniques are constructed that allow the information obtained from both scanning tunnelling microscopy and atomic force microscopy to be investigated for a variety of systems. These techniques are all based around Hückel molecular orbital theory or extended Hückel molecular orbital theory, and use a simple linear combination of atomic orbital basis, that allows rapid analysis of various systems.

The main focus of the work is the scanning probe microscopy of the C_{60} fullerene molecule. Theoretical scanning tunnelling microscopy images are constructed for the cases where C_{60} is adsorbed on both the substrate and the scanning probe in the form of a functionalised tip, as well as when a tip-adsorbed molecule interacts with a sample-adsorbed molecule. The atomic force microscopy images of surface adsorbed C_{60} are considered, with the main focus centred on the repulsive interaction observed due to the Pauli exclusion principle. The structure of the scanning probe, and the effect this has on this imaging is examined, as well as

considering the atomic force microscopy images obtained when two C_{60}s interact. Molecules other than C_{60} are also considered, with the techniques developed used to interpret and understand the atomic force microscopy images obtained when a pentacene and a PTCDA molecule interact with a carbon monoxide functionalised tip.

The theoretical work is accompanied throughout by a variety of experimental work, both from previously published work, and from unpublished work obtained by the University of Nottingham nanoscience group. Much focus is given to the interaction between C_{60} and the Si(111)-(7x7) reconstruction, both in the sense of a functionalised tip interacting with the surface, and with the interactions present where a C_{60} is adsorbed onto a surface. In doing so, previously postulated bonding sites for C_{60} on this surface have been verified.

Acknowledgements

Firstly, I would like to thank my supervisor Dr Janette Dunn, for her unwavering support and guidance over the course of the PhD, and for always showing confidence in me. I would also like to thank my second supervisor Professor Philip Moriarty, for his guidance, expertise and enthusiasm for the work. It has been a pleasure to work alongside them both during this research period. I would also like to thank the other members of the group who I have enjoyed working with, in particular Dr Ian Hands, who provided excellent support in the early part of the work, along with the late Professor Colin Bates, with whom I am grateful to have had the opportunity to work with, and is sadly missed. I also express my gratitude to Haifa Al-Qannas, for many insightful conversations, and Rob and Dr Dan for making the time enjoyable.

I am also especially grateful to my wonderful family. My fiancée Elisa for all the sacrifices she has made over the last few years, and for always being there for me. Our beautiful daughter Isabel who makes every day so enjoyable for me, and has doubled my productivity by making sure I work through the night. My parents and my brother to whom I will always be thankful for everything they have done and the sacrifices they have made. All my family and friends in Australia for keeping me entertained during the long nights sat in front of Mathematica, in particular Scott, Nick and Julie. Finally, a special thanks to Dr Christine Creagh at Murdoch. I will always be grateful for the confidence you gave me.

List of Publications

A.J. Lakin, I.D. Hands, C.A. Bates, J.L. Dunn, The Quadratic $p^3 \otimes h$ Jahn-Teller System as a Model for the C_{60}^{3-} Anion, *Vibronic Interactions and the Jahn-Teller Effect: Theory and applications, Vol:23*, Springer, Dordrecht, *eds. M. Atanasov, C. Daul, P.L.W. Tregenna-Piggott*, 231-243, (2012)

C. Chiutu, A.M. Sweetman, A.J. Lakin, A. Stannard, S. Jarvis, L. Kantorovich, J.L. Dunn, P. Moriarty, Precise Orientation of a Single C_{60} Molecule on the Tip of a Scanning Probe Microscpe, *Physical Review Letters*, **108**, 26, 268302, (2012)

J.L. Dunn, A.J. Lakin, I.D. Hands, Manifestation of Dynamic JahnTeller Distortions and Surface Interactions in Scanning Tunnelling Microscopy Images of the Fullerene Anion C_{60}, *New Journal of Physics*, **14**, 8, (2012)

A.J. Lakin, H.S. Alqannas, J.L. Dunn, Theoretical Modelling of Jahn-Teller Distorted C_{60} anions on a surface, *Journal of Physics: Conference Series*, **428**, 1, 012001, (2013)

A.J. Lakin, C. Chiutu, A.M. Sweetman, P. Moriarty, J.L. Dunn, Recovering Molecular Orientation from Convoluted Orbitals, *Physical Review B*, **88**, 3, 035447, (2013)

H.S. Alqannas, A.J. Lakin, J.A. Farrow, J.L. Dunn, Interplay between Coulomb and Jahn-Teller Effects in Icosahedral Systems with Triplet Electronic States Coupled to h-type Vibrations, *Physical Review B*, **88**, 16, 165430, (2013)

Contents

Theoretical Interpretation of Scanning Probe Microscopy Images Involving Organic Molecules

Theoretical Interpretation of Scanning Probe Microscopy Images Involving Organic Molecules

Chapter 1

Introduction

To understand the way in which atoms and molecules interact with each other it is of fundamental importance to understand their electronic properties. Electrons are fermions, and as such they obey the Pauli exclusion principle, which is the cause of the electron shell structure that is present in all matter. Thus, the electron forms the basis of properties such as chemical bond formation, and is essential for physical phenomena such as electricity, magnetism and thermal conductivity. There is therefore great advantage in being able to investigate and probe these properties at the atomic and molecular levels.

One rapidly advancing field that looks to take advantage of these various traits is that of nanoscience, which aims to investigate and manipulate single atoms and molecules. In doing so, not only is it possible to get a deeper insight into a vast array of properties, the possibilities of novel techniques is also brought closer to reality. One such area is that of molecular electronics, with molecular devices having the potential to far out-perform their silicon counterparts, as well as providing novel functionality that would not be possible using current semiconductor devices.

Amongst the most commonly utilised tools for probing at such a small scale is the scanning tunnelling microscope (STM) and the atomic force microscope (AFM), that between them, allow a variety of properties to be explored. However, to benefit from these tools, a thorough theoretical understanding of the

physics that underlies them is a necessity. The majority of the techniques used require computationally expensive calculations to be undertaken for the majority of systems investigated. Thus, there is much benefit in alternative methods that would allow easier analysis of the data obtained.

The aim of this work is to provide a simple theoretical technique to model the data obtained during STM and AFM for a variety of applicable systems. The main focus of the work will be to resolve a range of images obtained for the C_{60} Buckminsterfullerene molecule, where particular attention will be given to the case where the molecule is adsorbed on to the Si(111)-(7x7) reconstruction. In addition, considerable work will be shown modelling the images where C_{60} adsorbs onto the scanning probe. However, before this an overview of the central features of the work will be given.

1.1 Scanning Probe Microscopy

Scanning probe microscopy (SPM) is the name given to a variety of techniques that produce topographical maps of a certain position-dependent property of a sample. Most commonly, an atomically sharp probe is used which is then scanned over the sample in two dimensions detecting a particular variable. An image may then be produced in false colour using the data obtained at each point. While the resolution of the different techniques varies, it can be at a scale as small as picometers.

SPM has allowed for huge advances in nanoscience, and allowed for the manipulation of matter at the single atomic level, as shown by the pioneering work by Eigler and Schweizer [1] where single xenon atoms were manipulated on a Ni(110) surface to spell out the “IBM” company logo. Amongst the different forms of SPM perhaps the most commonly used are the STM, which measures the tunnelling current between the sample and probe, and the AFM, which measures the force between the two. These related techniques have driven the advancement of the field, particularly with respect to molecular electronics and the

potential formation of molecular devices. As early as 1991, Don Eigler produced single atomic switches using an STM [2]. Since then, the STM and AFM have played crucial roles in the development within this area.

1.1.1 Scanning Tunnelling Microscopy

SPM began in 1981, when Gerd Binnig and Heinrich Rohrer developed the STM [3], a microscope capable of atomic level resolution which would win them the 1986 Nobel Prize in Physics [4]. The basic principle behind the operation of this instrument is the quantum mechanical tunnelling of electrons between a conducting sample and a sharp tip, usually, although not by necessity, within a vacuum. The current that is produced from this tunnelling is then used to create a topographical map of the local density of states (LDOS) of the sample [5].

Good resolution for an STM is considered to be around 1Å laterally, and around 0.1Å in the depth [6]. The scanning probe is most commonly made from tungsten or platinum-iridium alloy, and is situated on a cantilever. Recent advances have allowed an increase in the resolution through functionalisation of this probe through deliberate adsorption of a species (commonly a CO molecule) on to the tip apex [7]. This leads to a well defined tip-structure, that is useful when interpreting the SPM data.

The uses of STM both as a research tool and within industry are widespread. The first time STM was used to resolve the structure of a surface was with the Si(111)-(7x7) reconstruction [8], which had previously not been investigated in real space. Since this point, STM has been used for investigating numerous surfaces, and an array of molecules to understand their properties. However, applications of STM are not just within research, with uses found in fields such as data storage and biological imaging [9].

There are two main modes in which the STM may be operated, namely constant height and constant current modes. The simplest, and quickest, of these is constant height mode, where the tip is scanned over the sample while being kept a fixed distance away from the surface, usually between an Angstrom and

a nanometre [10]. A bias is applied to the tip which allows electrons to tunnel either to or from the sample (depending on the bias), and it is this tunnelling current that is used to construct the image.

The alternative mode of operation is constant current mode, where a feedback loop incorporating a piezoelectric crystal is utilised which adjusts the tip height accordingly to maintain a fixed tunnelling current [10]. In this mode it is the deviation of the tip which is used to construct the images, as opposed to the change of current. An extension of this, known as dynamic STM (dSTM), may also be used which allows even greater detail to be observed. Again, a feedback loop is utilised to maintain a constant current by adjusting the tip height, but rather than the tip being fixed, the cantilever is driven to induce an oscillation of a set frequency. This allows the tip to penetrate closer to the sample, providing a more detailed image.

1.1.2 Atomic Force Microscopy

Following from the development of the STM in 1981, the AFM was devised by Binnig, Quate and Gerber in 1986 [4]. This closely related technique does not require a bias to be applied, and as such can be used on any surface, irrespective of the conductivity. Like the STM, the AFM consists of a sharp probe that scans over a sample. However, unlike the STM, it is not the tunnelling current, but the force exhibited between the probe and the sample that is used to construct the image. This generally involves bringing the tip in much closer to the sample than would be usual in STM.

The basic modes of operation for the AFM can be divided into two main categories, contact and non-contact. In contact mode, the tip is static (i.e. does not oscillate), and is pushed in sufficiently close to the surface such that a repulsive force is produced through the Pauli exclusion principle. The tip is then dragged along the surface, and the force mapped. In non-contact mode, the tip is oscillated much further away from the sample, such that the force experienced is van der Waals (vdW) in nature, and hence attractive. Again the force is used

to produce the image, although as the vdW force is much weaker than the Pauli repulsion, it is often detected through changes in frequency of the tip.

Similarly to STM, the AFM finds uses both within research and industry. There are clearly numerous applications within surface science and related disciplines. However, the technique has also found use in a medical context, where one of the early uses of AFM was to investigate the entire process of a living cell infected by a virus [11]. More recently, Gross *et al.* utilised functionalisation of the AFM probe to produce striking images of the pentacene molecule showing the individual bonds [7]. This same technique was used to unambiguously determine the chemical structure of cephanadole A for the first time, a molecule with interesting biological properties. Like the STM it has found use in industry, where it has particular uses in microelectronics, and like the STM, data storage [9].

1.2 The Fullerene Molecule, C_{60}

Since its discovery by Kroto *et al.* in 1985 [12], the C_{60} Buckminsterfullerene (often referred to simply as fullerene) molecule has undergone considerable experimental and theoretical research investigating a variety of the properties associated with it and its related systems. The molecule itself is made from sixty carbon atoms with each carbon bonded to three others, and has a truncated icosahedron structure, with 20 hexagonal faces, and ten pentagons, where no two pentagons are adjacent. This is shown by the ball and stick model in figure 1.1, where the 6-6 bonds (between two hexagons) are shown in cyan and the 5-6 bonds (between a pentagon and a hexagon) are shown in orange. These bonds are around 1.38Å and 1.45Å [13], and are commonly referred to as double (6-6) and single (5-6) bonds respectively. In fact the Pauling bond orders of the two bonds are 0.44 for the 6-6 bonds, and 0.28 for the 5-6 bonds, and so they are not true double and single bonds (which would have Pauling bond orders of 1 and 0) [13].

C_{60} is one of numerous fullerene molecules, the name given to molecules composed of carbon that form closed structures or tubes. Part of the interest in C_{60} stems from its unusually high symmetry, with the undistorted molecule being described by the icosahedral, I_h, point group, the highest form of point group symmetry found in nature [14]. This high symmetry prescribes the molecule with intriguing properties, and makes it an ideal candidate for investigating symmetry lowering interactions. One such interaction is the Jahn-Teller effect, which is relevant to the charged ions of C_{60}, and is believed to play a role in the surprising result that when combined with an alkali metal, compounds of the form A_2C_{60} and A_4C_{60} (which contain the C_{60}^{2-} and C_{60}^{4-} ions respectively) are mott insulating [15], whereas those of the form A_3C_{60} which contains the C_{60}^{3-} ion, are superconducting [16].

There are many other properties of C_{60} that have made it a useful tool for scientific research. It is stable at high temperature and pressure [17], while it is also common for endohedral fullerenes, fullerenes that contain a second chemical species inside the cage structure, to be formed using C_{60} [18]. It has also played a key role in fundamental research, in particular in the work by Arndt [19], which showed the wave-particle duality of C_{60} molecules.

Many practical applications of C_{60} exist away from research, including possible use as a hydrogen storage device [20] due to the high electron affinity of the molecule, and also within medicine, where it has been utilised in numerous aspects [21]. However, at present, interest on C_{60} is heavily focused on uses in

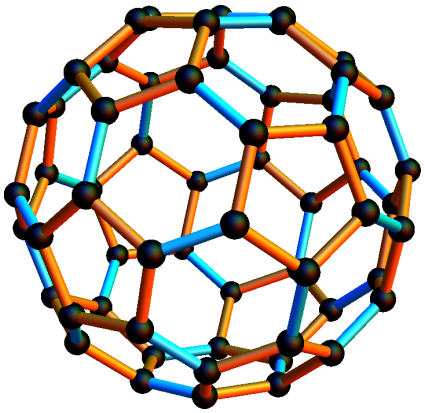

Figure 1.1: Ball & stick model of the C_{60} Buckminsterfullerene molecule. The 5-6 (single) bonds are shown in orange, and the 6-6 (double) bonds are shown in cyan

molecular electronics. Among numerous works in this field, it has been shown that C_{60} can act as a single molecule transistor [22], as well as work investigating C_{60} contacts [23, 24], C_{60} electrodes [25], and C_{60} junctions [26].

Chapter 2

Background

Due to its size and stability, C_{60} is an ideal candidate for STM and AFM related studies. In addition, the high symmetry it possesses makes it ideal for investigating external interactions that distort the molecular cage, and lowers this symmetry. The role C_{60} plays in various applications, and its potential use in molecular electronics means it is important that the electronic properties are understood, particularly when interacting with other molecules. It is therefore crucial that theoretical techniques continue to develop to interpret and understand the information obtained during STM and AFM for the complicated systems with which it can be associated.

In this chapter, some of the physics behind the various methods and techniques will be discussed, alongside a thorough review of the literature in the relevant areas. Firstly, the physics that forms the basis of STM and AFM will be described, before the idea of tip functionalisation will be introduced, and what benefits it brings. The various theoretical techniques that may be used when modelling STM and AFM will be considered, and the benefits of these discussed. Then, the commonly used Si(111)-(7x7) reconstruction will be described, before, finally, an overview of the literature will be given showing the links between C_{60}, STM, and AFM.

2.1 The Physics of STM

The fundamental principle which forms the basis of operation of the STM, is the quantum mechanical tunnelling of electrons between the STM tip and the sample under investigation. This occurs due to the fact that when an electron approaches a finite potential barrier, there is a non-zero probability that it will be found beyond this barrier. If the simple one-dimensional case is considered, the wavefunction of an electron approaching such a barrier decays exponentially within the barrier region according to the general expression:

$$\psi(z) = \psi(0)\, e^{\pm \kappa z}, \tag{2.1}$$

where $\psi(z)$ is the wavefunction at position z within the barrier, κ is the rate at which the wavefunction decays, which is dependant on the height of the potential barrier. The $\pm$ sign in the exponent is chosen such that the wavefunction decays for either positive or negative z. Relating this to the STM, the potential barrier can be considered as the (usually) vacuous region between the tip and sample. When no bias is applied, the height of this barrier is given by the work function associated with the electron under consideration. To construct an image, a current needs to be detected by the tip, so it is therefore necessary for a net flow of electrons to occur between the tip and sample. In order for tunnelling to occur, the tip needs to be brought sufficiently close to the sample so that the wavefunction has not decayed such that the flow would be too weak to detect. However, even if the tip and sample are close enough for sufficient tunnelling to occur, with them both considered at the same energy, the electrons would tunnel equally in both directions, resulting in no net current being observed. It is for this reason a bias is applied to the sample, in order to favour the flow of electrons in one direction or the other, and is why insulating samples can not be imaged through STM. If a negative sample bias is applied, the Fermi level of the sample electrons will be increased, favouring a flow from the sample to the tip. If a positive sample bias is applied, the Fermi level will be decreased, and the net current will be in the opposite direction.

There are two main modes of operation of the STM, constant height, and constant

current. The simplest mode of operation is constant height mode, where the probe is maintained at a fixed height above the sample during the scan, and it is the observed tunnelling current that is used to construct the final image. Scans in constant height mode can be undertaken at quicker speeds than constant current scans, although they suffer from a lack of detail. This is due to the exponential decay of the electron wavefunction (shown in equation (2.1)), which causes the current to have a similar exponential relationship [27] (this will be discussed in greater depth in chapter 3), and hence, only the uppermost parts of the sample are imaged in constant height mode. Additionally, it is only useful for very smooth surfaces, as the fixed height means that there is an increased chance of the tip crashing in to the surface. It is therefore only commonly used on flat samples, where this risk is reduced.

The second mode of operation is constant current mode, where the tunnelling current is maintained at a fixed value, and the height of the tip allowed to vary. It is this change in tip height that is then used to construct the final image. This has the advantage that the change is linear, and hence, a considerably more detailed image can be constructed than in constant height mode. However, the additional complication involved in maintaining the correct current, means that the scan rate is slower. Related to this mode is dynamic STM (dSTM), where a constant *average* current is maintained while the tip is oscillated at a set frequency. The exponential relationship between the current and tip height allows the tip to penetrate further into the sample than in constant current mode, for the same setpoint current. Again, this allows more detailed images to be constructed.

2.2 The Physics of AFM

The basic mechanism of the AFM is very similar to that of the STM, where a sharp probe is scanned over a sample and an image formed from the resultant data. However, whereas the STM relies on the tunnelling current observed when a bias is applied between the tip and sample, AFM relies on the force interaction between them to construct an image. This means that the requirement for a bias

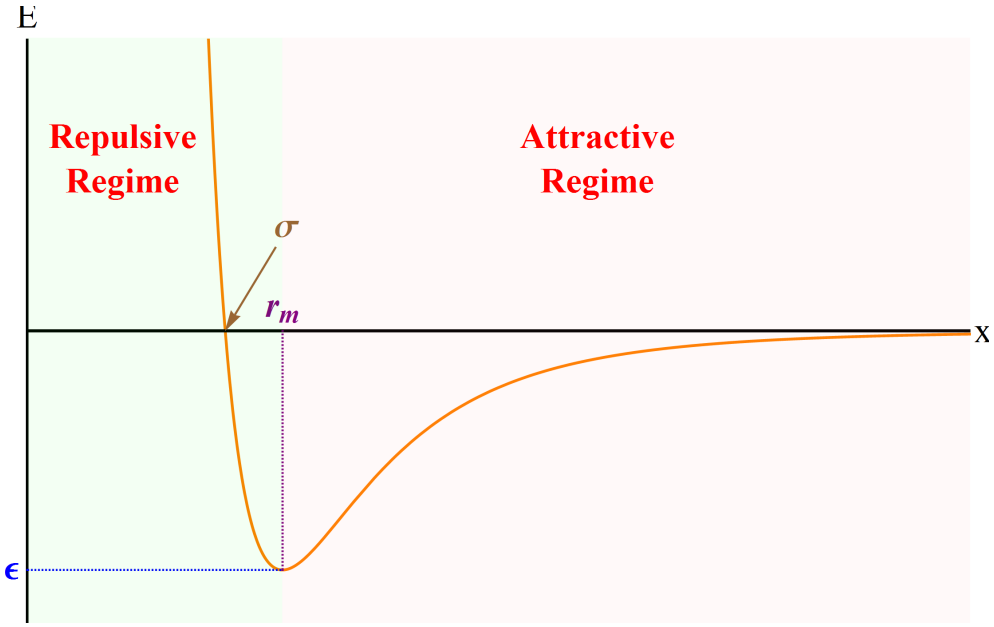

Figure 2.1: Lennard-Jones potential modelling the interaction of two arbitrary atoms. The pink and green shaded regions represent the attractive and repulsive regimes repectively, r_m is the interatomic separation at which the potential well reaches a minimum value of ϵ, and σ is the finite value at which the energy is zero.

to be applied is redundant, and as such AFM can be used on non-conducting surfaces.

The origin of the dominant force being measured in AFM can be either vdW or from the Pauli exclusion principle, depending on the distance between tip and sample. With the tip further away, the net force (for a neutral sample and tip) is vdW in nature, and hence attractive. As the tip becomes closer, Pauli exclusion becomes more and more significant, which is exhibited as a repulsive force. It is possible to image in both the attractive and repulsive regions in AFM, although the highest resolution images obtained to date are found by imaging where the repulsive interaction is dominant [28].

To understand the nature of the force further, it is worth considering a Lennard-Jones (LJ) type potential such as that one shown in figure 2.1, where the energy due to the interaction of two arbitrary atoms is plotted as a function of the interatomic distance. The LJ potential is an empirically derived function to model the energy of two interacting atoms, the details of which will be covered in more depth shortly. However, the important feature is the distinction between the attractive and repulsive regimes. It can be seen that the energy decreases within the

attractive regime as the two atoms approach, indicating an attractive force as the negative of the derivative of the curve is negative. At the position r_m, where the energy reaches a minimum, the vdW force exactly cancels the Pauli repulsion, and there is no net force acting between the atoms. When the atoms are pushed closer together, the energy, and hence the repulsive force, increases at a rapid rate. This increase results in a finite separation, denoted σ, at which the energy is zero.

The AFM may operate in either contact, or non-contact mode. Contact mode, where the tip is not oscillated, is generally undertaken within the repulsive regime with the tip 'dragging' along the surface. The probe is fixed to a cantilever, and a static deflection of this cantilever is maintained to keep a constant force, with the change in tip height then used to construct the image. Having a static cantilever causes the signal to be prone to noise, and as such stiff cantilevers with a high spring constant are used to help alleviate this problem. The close contact and strong forces involved, mean that contact mode is generally only utilised for flat, stable surfaces, and can not be used for imaging small molecules or rough surfaces.

In non-contact AFM (NC-AFM), the probe is oscillated, and imaging is generally undertaken in the attractive regime with the tip further away from the sample than in contact mode. There are two common schemes of operation in NC-AFM, frequency modulation and amplitude modulation. In frequency modulation, the cantilever is oscillated at its resonant frequency. The change in this frequency brought about from the tip-sample interaction is then used in forming the image. In amplitude modulation, the cantilever is driven at just above its resonant frequency, and it is then the change in amplitude that is used in constructing the final image. Stiff cantilevers are used in both cases to provide the optimum resolution.

There is a further mode of operation known as tapping mode, where the tip is oscillated at a large amplitude, at a large distance away from the sample. This mode is generally used for fragile samples, or where imaging is being undertaken in ambient conditions, as the large tip-sample separation and amplitude mean that the probe can penetrate close to the sample while spending less time in close

proximity to the sample where it may be damaged [29].

2.3 Tip Functionalisation

The tip used during SPM is usually made to be as atomically sharp as possible. That is, that in the ideal case there is a single atom at the apex of the tip. However, there is great difficulty in accurately determining what the exact tip state is from the STM or AFM data obtained. One way around this is to functionalise the tip through deliberate adsorption of a chemical species. In this way, the tip state can be assigned far more reliably, and the effect it has on the images obtained can be accounted for.

It is tip functionalisation that has allowed the imaging of organic molecules to be undertaken at unprecedented resolution [28]. Through adsorption of a CO molecule, Gross and co-workers have obtained molecular imaging through AFM revealing the individual bonds within molecules [7, 30, 13]. This concept has led to an array of new research, and has found use, among others, in the imaging of ferromagnetic domains [31], and the analysis of intermolecular forces [32].

One area in which tip functionalisation promises to be of significant importance is in the investigation of intermolecular properties. By picking up the molecule on the tip it is possible to directly observe properties such as conductance and the force interaction between two molecules as a function of the intermolecular separation, while also giving an insight into the nature of the bonding between molecule and substrate. In addition, it allows numerous orientationally dependent properties to be explored, something that is key in explaining the ordered structures observed on various forms of monolayer.

Early attempts to probe the tip structure during SPM were made by Giessibl *et al.* [33] and by Herz *et al.* [34], where inverse imaging from a Si(111)-(7x7) surface was used to observe the tip apex in AFM and STM respectively. Since these, much work has been undertaken to accurately interpret the tip structure directly from SPM images. This is exemplified by a series of works from Chaika

and co-workers [35, 36, 37, 38] looking at the accurate description of the tip termination through the interaction with a known surface structure. The importance of the tip termination in describing STM images is also shown in more general terms, in the work undertaken by Loos [39], Hagelaar *et al.* [40] and Gottlieb and Wesoloski [41], while the AFM images of PTCDA obtained with a CO terminated tip were examined from an experimental and theoretical perspective by Moll *et al.* [42]. Single atomic tips have also been investigated from a purely theoretical perspective in the work by Wright and Solares [43], while both experimental and theoretical work was undertaken investigating the effect of xenon, bromine and carbon monoxide tips during STM and AFM by Mohn *et al.* [44].

2.4 Modelling SPM

A variety of theoretical techniques exist for modelling the multi-electron systems that are imaged in SPM. One such technique is the Hartree-Fock method, which is a useful tool for the theoretical analysis of these systems, and aims to find an approximate solution to the Schrödinger equation. As no exact solution is obtainable for the overwhelming majority of multi-electron systems, the solutions are all found numerically, and an iterative process is used. Firstly, a set of electronic basis functions are estimated, which are then used to construct a portion of the full Hamiltonian, known as the Fock Matrix. Through diagonalisation of the Hamiltonian, the eigenfunctions suggest a new basis, which in turn is used to construct a new Fock Matrix and so on. This iterative process is repeated until the eigenfunctions match to the desired accuracy. While producing accurate results in some circumstances, the main drawback to this method is that the electron correlation interaction is not fully considered, which can produce significant deviations from the observed values. This can be corrected using post Hartree-Fock methods, although the computational time of these is considerably increased to make them only useful in certain circumstances.

The most common technique used that incorporates electron correlation is density functional theory (DFT). This technique is based on two theorems, known as

the Hohenberg-Kohn theorems. They state that firstly, the ground state of a many electron system is defined by the electron density that is a function of three spatial coordinates, and secondly, an energy functional exists such that the correct electron density minimises this functional.

In Kohn-Sham DFT, the most commonly utilised form of DFT, the interaction between electrons is modelled by considering a combination of non-interacting electrons moving within a fixed potential, and exchange and correlation interactions to model the electron-electron interaction. The main problem within DFT is accurately modelling this exchange-correlation interaction, with multiple functionals used depending on the accuracy required. Local density approximation (LDA) functionals are common, as are generalised gradient approximations (GGA), and hybrid functionals that incorporate part of the exchange interaction computed through the Hartree-Fock method.

Like the Hartree-Fock approach, DFT is an iterative process. The electron density is first approximated, and then used within a set of equations known as the Kohn-Sham equations to obtain a set of Kohn-Sham orbitals, which are then used to create a new estimate of the electron density. This continues until the required accuracy is obtained. One disadvantage of DFT is its computational expense, particularly when considering the complex systems that can occur in SPM. This is particularly true when modelling AFM, due to problems incorporating intermolecular interactions, especially when considering vdW forces [45].

Alternatives to these approaches that are less computationally expensive, although more limited in their applications, are the tight binding approach, and the related extended Hückel molecular orbital (EHMO) theory and standard Hückel molecular orbital (HMO) theory. Each of these methods are linear combination of atomic orbitals (LCAO) methods, with the simplest being HMO theory. In this method, the electronic basis is formed from π electrons only, and only interactions between nearest neighbour atoms are considered. In this way, all σ type bonding is considered negligible in determining the properties of a molecule. HMO theory is generally only accurate when considering conjugated molecules where there are alternating single and double bonds, although the errors associ-

ated with the different properties vary. Thus, while HMO theory may not predict all of the properties correctly, it can still be used for some molecules which are not conjugated.

One of the advantages of HMO theory is that no integrals need to be calculated to obtain the results. Instead, the matrix element associated with nearest neighbour atomic orbitals is given the unknown value β, and all energy values are produced as a function of this unknown. This greatly increases the computational speed, as the only calculation is the diagonalisation of a numerical matrix, although its limitations mean that it is not often used in molecular modelling.

EHMO theory modifies HMO theory by incorporating the interactions between all atoms, and also by introducing the σ bonding into the calculation. Unlike HMO theory, this technique requires the evaluation of the overlap integrals to calculate the matrix elements, and as such is slightly more computationally expensive than HMO theory. However, like HMO theory, an iterative procedure is not necessarily required (although can be used in what is called self-consistent EHMO theory), which, while reducing the accuracy of the method in some cases, has substantial computational benefit. Both HMO theory and EHMO theory will be discussed in greater detail in chapter 3.

Tight binding is closely related to EHMO theory but it is generally used for dealing with crystalline structures rather than individual molecules. The name 'tight binding' comes from the assumption used that the electrons associated with each atom within a crystal can be approximately described by the atomic orbitals of that atom, and thus are tightly bound to it. A Hamiltonian is constructed in the same way as for EHMO theory by using the atomic orbitals as the basis, and, on the assumption that the atomic overlaps are small, a perturbation is added to the Hamiltonian to form the tight binding Hamiltonian. Diagonalising this results in the electronic states for the appropriate Bloch energies of the crystal.

2.5 Si(111)-(7x7) Reconstruction

The Si(111)-(7x7) reconstruction was first observed using low-energy electron diffraction by Schlier and Farnsworth in 1959 [46], although its detailed structure did not become apparent until 1982, when the surface was first resolved in real space through the use of STM imaging, and an adatom model was suggested [8]. The work by Takayanagi [47] then followed that suggested a dimer adatom stacking-fault (DAS) model which has since been further verified by ab-initio calculations [48], and been accepted as the true structure.

The complete structure of the unit cell is shown in figure 2.2a as taken from ref. [48]. The crucial feature as far as SPM is concerned, is the location of the twelve adatoms, as the images obtained during both STM and AFM are primarily formed by the interaction between the tip and these adatoms, as shown in figure 2.2b. This interaction stems from the orbital structure of these adatoms, with each possessing a sp^3 dangling bond that points normal to the surface.

There are three layers to the reconstruction. The first layer contains the stacking fault, which distinguishes one side of the unit cell from the other. Above this is the dimer layer, while the third layer contains the twelve adatoms, where each of the adatoms are bound to three silicon atoms within the stacking fault layer. The other main feature of the reconstruction is the corner hole, which is found on the corners of each unit cell, and extends down to the Si(111) layer below

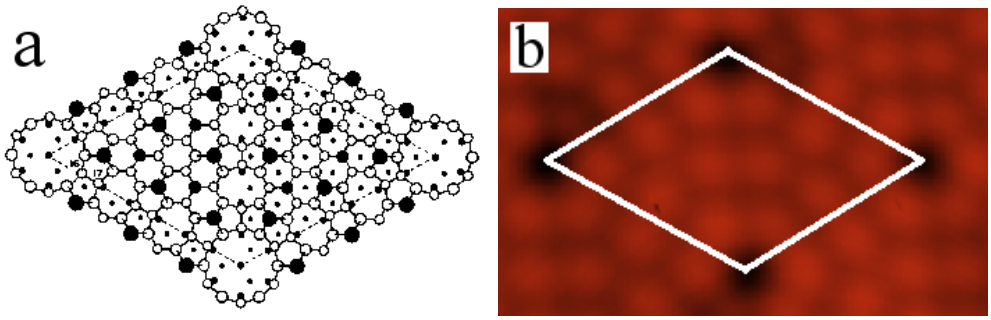

Figure 2.2: a, The unit cell (dashed) of the Si(111)-(7x7) reconstruction taken from ref. [48] constructed using ab-initio calculations. The large black dots represent the 9 adatoms, the smaller black dots are the underlying rest atoms, the white circles represent the dimers, and the smallest black dots show the first layer of the unreconstructed surface. The faulted side of the unit cell is on the left hand side. b, Experimental STM image of the Si(111)-(7x7) surface, showing the 12 adatoms within the unit cell (outlined in white)

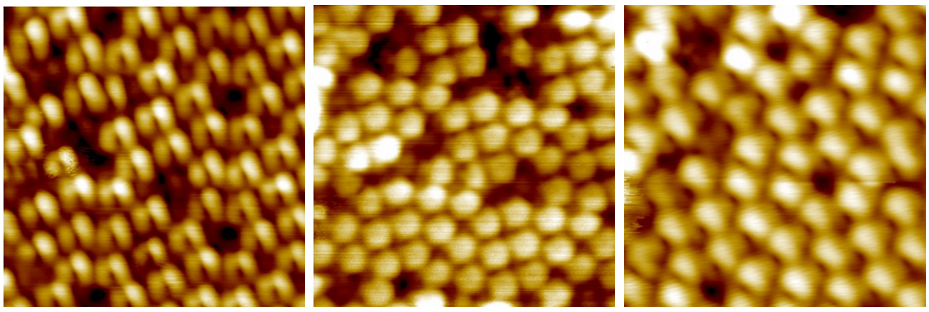

Figure 2.3: Selection of STM images of the Si(111)-(7x7) surface showing a variety of tip structure [50]

the stacking fault layer. This has uses during SPM by acting as a reference point to distinguish between background signal, and that obtained from the adatom interaction [49]

One of the benefits of using the Si(111)-(7x7) surface, is that the large inter-adatom distance makes it ideal for investigating the tip structure during AFM and STM. This is shown by numerous works, but particularly in the inverse imaging work from Herz *et al.* [34]. A selection of STM images revealing a variety of tip structures are shown in figure 2.3, with the interpretation of this form of image forming part of the work presented here.

2.6 C_{60} and SPM

C_{60} has been used extensively in SPM related research, an overview of which is given by Moriarty [51]. A lot of the experimental work has focussed upon the various properties and structure of C_{60} islands and monolayers. Franke and Pascual [52] investigated electron transport through C_{60} molecules on Cu(110), Pb(111) and Au(111) surfaces, while Gardener *et al.* [53] also investigated C_{60} on Au(111), but instead to examine the orientational structure of C_{60} monolayers. Various other surfaces have been examined, including the investigation of C_{60} self-assembly on graphene [54], and looking at rotating C_{60} molecules within a monolayer on W(110) and WO_2 surfaces [55] among others.

The majority of this work has used DFT where possible to interpret certain aspects of the experimental data, although, as the systems under consideration are

generally large, the computational expense can often exceed that viable for a realistic DFT calculation, and a full theoretical explanation can not be provided. This is not always the case, and joint STM and DFT studies have been undertaken, such as the work by Wang and Cheng [56] that examined the ordering of a C_{60} monolayer on Au(111) and Ag(111) surfaces by considering four molecules on the surface in DFT. However, in general, the computational expense is usually too great to have a thorough theoretical interpretation of C_{60} monolayers.

The computational demand is less problematic, although still relevant, when considering SPM of individual molecules. Again, a large body of experimental work has been undertaken looking at the various properties of individual molecules, much of it in relation to possible applications in molecular electronics. The conductance of a single C_{60} molecule was measured with gold electrodes in STM by Bohler *et al.* [57], while the spectral density of an Ag(110) adsorbed C_{60} was measured by Lu *et al.* [58]. The most commonly used theoretical technique to interpret the data is again DFT, as exemplified by the work by Cho *et al.* [59] who examined charge transfer associated with the C_{60}-Cu interface in a joint STM and DFT study. Further examples are the work by Casarin *et al.* [60] and Hou *et al.* [61] who both used DFT along with STM to look at the bonding between C_{60} and Pt(110) and Si(111)-(7x7) respectively.

While DFT is by far the most common theoretical approach to modelling SPM of C_{60}, alternatives have also been used. Specifically, Rurali *et al.* [62] used a tight binding mechanism to predict various bonding sites of C_{60} on Si(111)-(7x7), with the predicted orientations later experimentally observed in STM undertaken by Du *et al.* [63]. HMO theory has been used in the work by Hands *et al.* [64] and Heinrich [65] to determine the molecular orientation of C_{60} from STM. This was also used in further work by Hands *et al.* [66], Dunn *et al.* [67], and Lakin *et al.* [68] to attempt to explain the STM images of the Jahn-Teller distorted C_{60}^{-} anion. However, despite the fact that C_{60} is an excellent electron acceptor, very little experimental work has been undertaken on this, or any other of the anions of C_{60}. The exception to this is the work undertaken initially by Wachowiak *et al.* [69], which was follow by Wang and co-workers [70, 71] which imaged

K_2C_{60}, K_3C_{60}, and K_4C_{60} monolayers, which contain the C_{60}^{2-}, C_{60}^{3-} and C_{60}^{4-} ions respectively, in STM, identifying some novel molecular orienting within the monolayer.

In addition to the work by Rurali *et al.* [62] and Hou *et al.* [61], a selection of work has also been undertaken looking at C_{60} adsorbed on Si(111)-(7x7). The work by Hou was followed by research from Pascual *et al.* [72] who postulated an alternative explanation to the results of Hou, and noted the surprising lack of bias dependence in Pascual's experimental images. More recently Huang *et al.* [73] used STM to identify molecular orientations of both C_{60} and C_{84} on the surface.

All of the work mentioned thus far has utilised STM, for the simple reason that it is far more numerous within the literature. However, work has also been undertaken looking at AFM images of C_{60}. Loske *et al.* [74] observed contrast inversion within C_{60} islands as the tip-sample separation was altered, while Chiutu *et al.* [75] measured the Si-C_{60} chemical force characteristics through AFM. High resolution images of C_{60} have been obtained firstly by Pawlak *et al.* [76] using force modulated AFM, and later by Gross *et al.* [13] where, by using a CO terminated AFM tip, the Pauling bond order of C_{60} could be determined.

Chapter 3

Theoretical Techniques

Before beginning the investigative portion of the work, it is first necessary to introduce a number of mathematical techniques and theoretical constructs that will be used in the modelling process. In this chapter, an overview of previously utilised methods that will be required throughout this work will be introduced, followed by a comprehensive explanation, and where relevant, justification, of the new methods that have been developed during the course of this research. Where necessary, specific examples will be given to aid in the understanding of these methods.

This chapter will start by examining how the tunnelling current observed during STM can be derived for a particular tip state, with Chen's derivative rule utilised to model a variety of tip orbitals. The theory and mathematics behind the force interaction observed in AFM will then be considered, with particular focus given to the repulsive interaction induced by the Pauli exclusion principle. HMO and EHMO theory will then be explained in detail, and the choice of electronic basis set discussed with particular attention to the advantages and disadvantages of different bases. A selection of group theoretical techniques will then be outlined, before the way in which these can be used to model an external interaction will be discussed.

3.1 Modelling STM Images

Images obtained from STM are constructed by analysing the tunnelling current observed between the tip and sample. While ultimately, different methods may be used to model the STM, these will only represent different ways of obtaining the electronic distribution within the system. The important step in constructing STM images is relating this to the observed current, and it is this that shall be the initial focus.

3.1.1 Bardeen's Tunnelling Theory

To model the tunnelling current observed during STM, Bardeen's tunnelling theory may be used. The tunnelling current is expected to be proportional to the probability of a transition occurring between electronic states of the sample and the tip. If this tunnelling is treated through time-dependent perturbation theory, the probability, P, that this transition will occur from a state χ to a state ψ, is given by Fermi's golden rule:

$$P = \frac{2\pi}{\hbar} \sum_{\nu} |M|^2 \, \delta \left(E_{\chi_\nu} - E_{\psi} \right), \tag{3.1}$$

where ν sums over all states χ, that can tunnel into ψ, and M is defined as the tunnelling matrix element. The δ function ensures that tunnelling only occurs between sites of equivalent energy. Throughout this work, it will be assumed that the states available for tunnelling will be sufficiently far apart, such that only one (or more if degeneracies exist) state will form the predominant contribution to the current (i.e. the probability of any other state having the required energy has decayed sufficiently such that it can be neglected). In this case, the sum does not need to be considered, and the simple relationship whereby:

$$I \propto P \propto \sum_{i} M_i^2, \tag{3.2}$$

is produced, where the summation i, is over any states of equal energy. The tunnelling matrix element is produced through Bardeen's transfer Hamiltonian

theory, and takes the form [27]:

$$M = -\frac{\hbar}{2m}\int_{\Omega_T}\left(\chi^*\nabla^2\psi - \psi^*\nabla^2\chi\right)d\tau. \tag{3.3}$$

Here m is the mass of the electron, Ω_T represents the effective volume of the tip, and τ indicates the space over which to integrate.

One of the assumptions within Bardeen's transfer Hamiltonian theory, is that the system is separable into two known Hamiltonians associated with the electronic wavefunctions of the two states involved in tunnelling (the tip and sample states with respect to STM), and a third Hamiltonian known as the transfer Hamiltonian. With this assumption, and relating it to STM, under positive sample bias, tunnelling will occur from the occupied states of the tip to the unoccupied states of the sample, and as such χ can be defined as the single electron tip wavefunction of the occupied state, and ψ, can be defined as the sample electronic wavefunction of the unoccupied state of the sample. When a negative sample bias is applied, tunnelling occurs from the occupied states of the sample, to the unoccupied states of the tip, and therefore the situation is reversed, with χ representing the occupied sample electronic state, and ψ representing the unoccupied tip state.

3.1.2 Calculating the Matrix Element

With the exception of the most simple of cases, the integral within the matrix element produces very complicated analytical solutions, if indeed an analytical solution is obtainable, and as such, calculating the matrix element can be problematic. Fortunately, if the tip wavefunction is assumed to be of certain forms, the integral simplifies to give considerably less complicated results.

It has been shown, firstly by Tersoff and Hamann using Fourier transforms [77], and then later by Chen [5] using a Green's function, that if the tip is considered as a simple s-type atomic orbital associated with a single atom, the integral in equation (3.3) reduces such that the matrix element is proportional to the wave-

function of the sample orbital only, determined at the tip centre $\mathbf{r}_0$, i.e.:

$$M \propto \psi\left(\mathbf{r}_0\right). \tag{3.4}$$

To show that this is the case, the Green's function method as outlined by Chen [5] can be considered.

By using a spherical modified Bessel function, it can be shown that the s-type spherical harmonic representing the tip can be written as a Green's function [5]:

$$\chi_s \propto G(\mathbf{r} - \mathbf{r}_0), \tag{3.5}$$

where χ_s is the tip wavefunction, and $G(\mathbf{r} - \mathbf{r}_0)$ is the Green's function centred at the tip position $\mathbf{r}_0$.

This can be placed into the integral in equation (3.3) to give:

$$M \propto \int_{\Omega_T} \left(G(\mathbf{r} - \mathbf{r}_0)\nabla^2\psi(\mathbf{r}) - \psi(\mathbf{r})\nabla^2 G(\mathbf{r} - \mathbf{r}_0)\right) d\tau. \tag{3.6}$$

The Schrödinger equation for the Green's function is given by [5]:

$$\left(\nabla^2 - \kappa^2\right) G(\mathbf{r} - \mathbf{r}_0) = \delta\left(\mathbf{r} - \mathbf{r}_0\right), \tag{3.7}$$

where $\delta\left(\mathbf{r} - \mathbf{r}_0\right)$ is the Dirac-delta function.

Using this, equation (3.6) expands to:

$$\begin{aligned} M &\propto \int_{\Omega_T} \left(G(\mathbf{r} - \mathbf{r}_0)\kappa^2\psi(\mathbf{r}) - \psi(\mathbf{r})\left(G(\mathbf{r} - \mathbf{r}_0)\kappa^2 - \delta\left(\mathbf{r} - \mathbf{r}_0\right)\right)\right) d\tau \\ &\propto \int_{\Omega_T} \psi(\mathbf{r})\delta\left(\mathbf{r} - \mathbf{r}_0\right) d\tau. \end{aligned} \tag{3.8}$$

This can be simplified further using the relationship for the time shifted Dirac delta function:

$$\int f\left(\mathbf{r}\right)\delta\left(\mathbf{r} - \mathbf{r}_0\right) = f\left(\mathbf{r}_0\right), \tag{3.9}$$

to give the result in equation (3.4), where M is proportional to the sample wavefunction evaluated at the tip centre $\mathbf{r}_0$.

3.1.3 Chen's 'Derivative Rule'

Using the ideas outlined for the s-type tip, it is also possible to look at the situation where the tip is described by a p or d orbital of the various forms, leading to what is termed the 'derivative rule' [78]. Again, through the use of spherical modified Bessel functions, these different tip states can be related to a Green's function. To see how this can be used, the example of the p_z tip state shall be taken, which may be represented by the derivative with respect to z of a Green's function [78]. This same method can be applied with the appropriate Green's function to use with any atomic orbital, to produce a derivative relationship.

It can be seen from the calculations for the s-type tip state, that the following relationship exists:

$$\psi\left(\mathbf{r_0}\right) \propto \int_{\Omega_T} \left(G(\mathbf{r}-\mathbf{r}_0)\nabla^2\psi\left(\mathbf{r}\right) - \psi\left(\mathbf{r}\right)\nabla^2 G(\mathbf{r}-\mathbf{r}_0)\right) d\tau. \tag{3.10}$$

If the derivative of both sides is taken with respect to z_0, the following result is produced, noting that z_0 only occurs in the Green's function and is unaffected by the integration, and so can be introduced within the integral:

$$\frac{\partial}{\partial z_0}\psi\left(\mathbf{r_0}\right) \propto \int_{\Omega_T} \left(\frac{\partial}{\partial z_0}G(\mathbf{r}-\mathbf{r}_0)\nabla^2\psi\left(\mathbf{r}\right) - \psi\left(\mathbf{r}\right)\nabla^2\frac{\partial}{\partial z_0}G(\mathbf{r}-\mathbf{r}_0)\right) d\tau. \tag{3.11}$$

As the p_z tip state may be represented by the derivative of a Green's function with respect to z [5], equation (3.11), can be simplified to give:

$$\begin{aligned}\frac{\partial}{\partial z_0}\psi\left(\mathbf{r_0}\right) &\propto \int_{\Omega_T} \left(\chi_{p_z}\nabla^2\psi - \psi\nabla^2\chi_{p_z}\right) d\tau \\ &\propto M_{p_z},\end{aligned} \tag{3.12}$$

a surprisingly simple result, that again only relies upon knowledge of the sample wave function.

Using the same approach for other tip states gives the results that are summarised in table 3.1 [78].

Table 3.1: The reduction of the matrix element when the tip is assumed to be of the form of a particular atomic orbital [78]

Tip Orbital	Proportionality to M
s	$\psi(\mathbf{r_0})$
p_x	$\frac{\partial}{\partial x}\psi(\mathbf{r_0})$
p_y	$\frac{\partial}{\partial y}\psi(\mathbf{r_0})$
p_z	$\frac{\partial}{\partial z}\psi(\mathbf{r_0})$
d_{zy}	$\frac{\partial^2}{\partial z \partial y}\psi(\mathbf{r_0})$
d_{zx}	$\frac{\partial^2}{\partial z \partial x}\psi(\mathbf{r_0})$
d_{xy}	$\frac{\partial^2}{\partial x \partial y}\psi(\mathbf{r_0})$
$d_{3z^2-r^2}$	$2\frac{\partial^2}{\partial z^2}\psi(\mathbf{r_0}) - \frac{\partial^2}{\partial y^2}\psi(\mathbf{r_0}) - \frac{\partial^2}{\partial x^2}\psi(\mathbf{r_0})$
$d_{x^2-y^2}$	$\frac{\partial^2}{\partial x^2}\psi(\mathbf{r_0}) - \frac{\partial^2}{\partial y^2}\psi(\mathbf{r_0})$

3.2 Modelling the Force Interaction

The nature of the force interaction observed during AFM is dependent on the regime in which imaging is taking place. In the attractive regime, when the tip-sample separation is relatively large, the dominant force is vdW in nature, and when in the repulsive regime, it is the Pauli repulsion which has the most significant contribution. The mechanism behind these differ greatly, and so from a modelling perspective they need to be treated differently.

Problems exist in using first principle arguments to describe the vdW type interaction, and as such, most of the techniques involve empirically derived functions to fit experimental data. Numerous alternatives exist to model the interaction between two atoms, including the Born-Mayer and Morse potentials [79], but here the Lennard-Jones potential will be used where needed.

The LJ potential is defined either in terms of the finite distance, σ, at which the interatomic potential is zero, or in terms of the distance at which the potential reaches its minimum, r_m. This gives two possible, equivalent expressions:

$$\begin{aligned} V_{LJ} &= 4\epsilon\left[\left(\frac{\sigma}{r}\right)^{12} - \left(\frac{\sigma}{r}\right)^{6}\right] \\ V_{LJ} &= \epsilon\left[\left(\frac{r_m}{r}\right)^{12} - 2\left(\frac{r_m}{r}\right)^{6}\right], \end{aligned} \tag{3.13}$$

where ϵ is the depth of the potential well. A plot of this function was shown in figure 2.1 in chapter 2 with the key parameters highlighted. To use this function, values are given for ϵ and either σ or r_m, that have usually been found previously

from experiment, and are dependent on the atomic species under consideration, and the systems with which they are associated.

The two terms found within the potential, model the Pauli repulsion and the vdW force separately. The r^{-12} term is used to model the Pauli repulsion, and gives rise to the steep increase in the function observed when the interatomic separation is closer than the minimum energy point. It is the r^{-6} term that models the vdW force that is dominant at long range. The nature of these terms mean that the LJ potential is often referred to as the 6-12 potential.

As seen, the LJ potential also incorporates the short-range Pauli repulsion. However, when looking at molecular interactions this does not possess sufficient accuracy to be usefully utilised. To incorporate this interaction into the model, the process based upon that outlined by Moll *et al.* [42] for same spin electrons can be used.

As electrons are fermions, they must obey the Pauli exclusion principle in that two electrons must not have the same quantum state. Mathematically, this can be interpreted as imparting an orthogonality relationship on two electrons, such that the electronic states must be orthogonal to one another, i.e.:

$$\langle \Psi(1) | \Psi(2) \rangle = 0, \tag{3.14}$$

where $\Psi(1)$ and $\Psi(2)$ are the wavefunctions of the two electrons

If it is assumed the wavefunctions of the electrons can be described by the appropriate atomic orbitals, for any real system, where the electrons are not infinitely far apart, the overlap between them will be non-zero. As such, without modification to these orbitals, equation (3.14) would not hold. Theoretically, this is treated by assuming that the wavefunction of one of the electrons remains unaltered, and the second wavefunction is then orthogonalised with respect to this. In this work, and in the work undertaken by Moll [42], this is done using a Gram-Schmidt orthogonalisation such that:

$$|\Psi(2)'\rangle = \frac{|\Psi(2)\rangle - \langle \Psi(1) | \Psi(2) \rangle \, |\Psi(1)\rangle}{\sqrt{1 - |\, \langle \Psi(1) | \Psi(2) \rangle \,|^2}}, \tag{3.15}$$

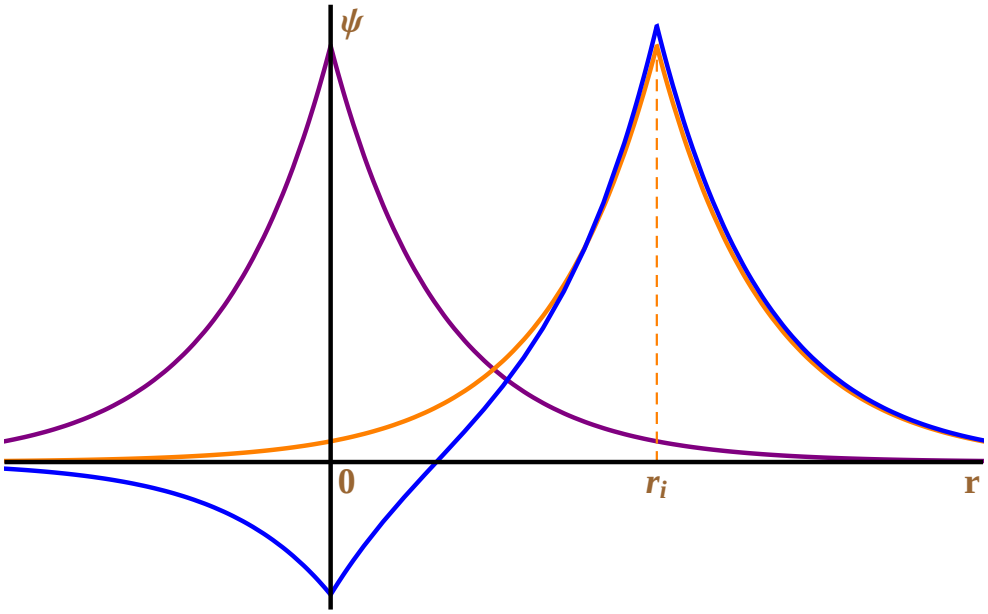

Figure 3.1: Orthogonalised and unorthogonalised states for two interacting s-type Slater orbitals separated by a distance r_i. The wavefunction of the first electron is in purple and remains unchanged, while the unorthogonalised state of the second electron is in orange, and the orthogonalised state is in blue.

which ensures that:

$$\langle \Psi(1) | \Psi(2)' \rangle = 0. \tag{3.16}$$

The effect this has on the wavefunction is shown in figure 3.1, where two s-type Slater orbitals, one centred on the origin, and one centred at r_i, are shown with and without the orthogonalisation requirement. The purple line represents the wavefunction of the first electron, and does not change during orthogonalisation. The orange and blue lines represent the unorthogonalised and orthogonalised states respectively. This change in shape of the wavefunction results in an increase in the kinetic energy of the system, and it is from this, that the Pauli repulsion results.

The change in kinetic energy can be expressed as a function of the interatomic distance by simply taking the difference between the kinetic energy of the orthogonalised and unorthogonalised systems. i.e.:

$$\Delta E_{\text{kin}} = \langle \Psi(2)' | \hat{T} | \Psi(2)' \rangle - \langle \Psi(2) | \hat{T} | \Psi(2) \rangle \,, \tag{3.17}$$

where $\hat{T}$ is the kinetic energy operator, which in atomic units, takes the form:

$$\hat{T} = -\frac{1}{2}\nabla^2. \tag{3.18}$$

The relationship between the kinetic and potential energy is in general not straightforward for quantum systems, as the Pauli repulsion is a non-conservative force, with a non-homogeneous potential [42]. However, for diatomic (or dimolecular as will be considered later) systems where there is only one degree of freedom, as is the case during AFM, when the tip is only allowed to deviate in the Z direction normal to the scan, the relationship is much simpler. For these cases, the interaction energy can be expressed via the improper integral:

$$\Delta E_{\text{int}}(Z) = \frac{1}{Z} \lim_{\gamma \to \infty} \int_{Z}^{\gamma} \Delta E_{\text{kin}}(Z') dZ'. \tag{3.19}$$

At this point, it should be noted that techniques are available, in particular the method detailed by Sader and Jarvis [80], for allowing the experimentally derived frequency shift to be related to both the force and interaction energy. As such, the expression in equation (3.19) is sufficient for comparison with experiment. However, it is sometimes beneficial to go beyond this, and derive the force, which is related to the negative of the first derivative of $\Delta E_{\text{int}}(Z)$, or the frequency shift, which is related to the second derivative. This will be considered in more detail in chapter 7

3.3 HMO and EHMO Theory

The methods outlined above for modelling both STM and AFM rely on the wavefunctions of the electrons involved being able to be found. Using Bardeen's tunnelling theory, the current observed during STM has been shown to be proportional to the square of the matrix element of the system (equation (3.2)), which, using Chen's derivative rule, is proportional to the square of a certain derivative of the sample wavefunction (table 3.1) when the tip is considered to be of the form of some atomic orbital. In AFM, the Pauli repulsion is modelled by considering the orthogonalised electronic states that make up the system. Thus, the final step in order to construct theoretical images, is to obtain an expression for the appropriate states. In this work HMO theory will be used predominantly, although EHMO theory will also be considered.

Both HMO and EHMO express the electronic wavefunctions as molecular orbitals (MOs). A MO is simply a mathematical function which is used as an approximation to the single electron wavefunction of each electron within a molecule. Thus each molecule contains numerous MOs. In the same way that electrons associated with an atom are restricted to atomic orbitals of different energy, the electrons around a molecule are restricted to different energy MOs. Thus, electrons added to a molecule occupy the MOs in order of increasing energy. The highest energy MO that is filled is referred to as the highest occupied molecular orbital (HOMO), with the next highest energy MO referred to as the lowest unoccupied molecular orbital (LUMO). Together, the HOMO and the LUMO form the frontier orbitals. It is also common for the unoccupied orbitals to be termed virtual orbitals.

3.3.1 HMO Theory

Although limited in its applications, HMO theory is a quick and powerful tool in the construction of MOs for the systems where it is valid. There are a number of assumptions that need to be made in order to use HMO theory. Firstly, it is necessary that the bonding within the molecule is dominated by π bonding, and any σ bonding that is present is assumed to have a negligible contribution when determining the molecular properties. This leads to the general rule that for HMO theory to be applicable, the system must be planar, and have conjugated bonding, i.e. it has alternating single and double bonds. However, there are exceptions to this, (as will be considered with C_{60}), where HMO theory correctly predicts some, but not all of the molecular properties.

HMO theory constructs the expressions for the MOs by considering a LCAO associated with each atom. Each of the atoms contributes a single electron to the π bonding network within the molecule, and as such the basis of atomic orbitals used to construct the linear combination is the set of p orbitals associated with each atom, pointing outwards from the molecule (for planar molecules aligned in the xy plane, these would be p_z orbitals). A Hückel Hamiltonian can then be

constructed that acts on this basis, which incorporates the kinetic and potential energy of the electron on the diagonal elements, and the interaction between adjacent orbitals only, on the off diagonal terms. Any interaction between next nearest neighbours and greater is deemed negligible.

In its most basic form, the elements of the matrix are defined as follows:

$$\begin{aligned}\mathcal{H}_{ii} &= \langle\psi_i|\mathcal{H}|\psi_i\rangle = \alpha \\ \mathcal{H}_{ij} &= \langle\psi_i|\mathcal{H}|\psi_j\rangle = \beta \text{ if the atoms are adjacent, or } 0 \text{ otherwise.}\end{aligned} \tag{3.20}$$

The term α is referred to as the Coulomb integral, and is what represents the total potential and kinetic energy associated with the electron present in the p orbital of atom i. The β term is the resonance integral and represents the energy of an electron in the region between atoms where the atomic orbitals overlap. This definition incorporates the assumption that only nearest neighbour atomic overlaps are considered, by assigning all other terms in the Hamiltonian to zero.

For a Hamiltonian of any form, the secular equation is defined as:

$$\mathcal{H}\vec{\Psi} = \epsilon\vec{\Psi}. \tag{3.21}$$

Here, ϵ is the energy, and is found from the eigenvalues of the Hamiltonian, $\mathcal{H}$, while the wavefunction is given by $\vec{\Psi}$, which is found from the eigenvectors of $\mathcal{H}$. As the basis to the Hamiltonian is the 60 radial p orbitals associated with each atom, the wavefunction of the π orbital system defined by the eigenvector of this Hamiltonian is a linear combination of these orbitals, such that:

$$\vec{\Psi} = \sum_i c_i\psi_i, \tag{3.22}$$

where i sums over all atoms, and c_i is the coefficient indicating the relative proportion of the p orbital ψ_i in $\vec{\Psi}$, as dictated by the specific eigenvector. Thus, to obtain the mathematical expressions that represent the MOs, and their relative energies, it is necessary to diagonalise the Hamiltonian to give the eigenvectors as a function of the p orbitals.

In HMO theory, the Hückel Hamiltonian becomes a sparse matrix containing elements equal to either α on the diagonal elements or β on the non-zero off-diagonal elements. However, to obtain the eigenvalues and eigenvectors it is not

necessary to know the values for either α or β. Instead, the secular equation is divided through by β, resulting in a Hamiltonian that has the same unknown on each diagonal element. The full calculation and implications of this will be covered in more detail in chapter 4, although this results in the eigenvectors being correctly obtained, but with the eigenvalues (energy levels) given as a function of α and β. However, the advantage of this method is that no empirical data is needed, and no integrals need to be calculated, making HMO theory an incredibly quick method.

3.3.2 EHMO Theory

While of considerable use for the systems in which it is valid, HMO theory is still limited in its use, and can not predict energy values, due to the unknowns α and β. One way around this that is incorporated into EHMO theory, is to firstly consider all of the valence electrons in the calculation, and include the overlaps between all the atomic orbitals considered. This allows the method to be used in far more instances than regular HMO theory, and also removes the unknown variables α and β from the technique. However, the values chosen for α are based on empirically obtained data, and calculating the values for β involve a series of overlap integrals which add to the computational expense.

The value for α is generally taken to be the negative of the ionisation potential from each electron within the molecule. As this is determined experimentally, the method is considered to be semi-empirical in nature, although extensions such as the Fenske-Hall method [81] exist that aim to resolve these values from first principles. Using this value for α, and the overlap integrals between the atomic orbitals, it is possible to define all the elements of the Hamiltonian numerically, such that:

$$\begin{aligned} \mathcal{H}_{ii} &= -E_{\text{ion}} \\ \mathcal{H}_{ij} &= KS_{ij}\frac{\mathcal{H}_{ii}+\mathcal{H}_{jj}}{2}, \end{aligned} \tag{3.23}$$

where, E_{ion} is the appropriate ionisation potential, S_{ij} is the overlap between the ith and the jth atomic orbitals, and K is the Wolfsberg-Helmholtz constant.

For hydrocarbons, accurate predictions are found when K is taken to be 1.75, as discussed in the work by Hoffmann [82]. As such, the same value shall be used here.

Using the definitions in equation (3.23), it is then straightforward to construct and diagonalise the Hamiltonian, to obtain numerical expressions for the energy levels and eigenvectors of the system. The removal of the unknowns from the theoretical method means that the absolute energy values can be predicted. However, to calculate the overlaps present on the off-diagonal elements of the Hamiltonian, it is necessary to undertake a large number of overlap integrals for each electron, which increases the computational expense.

3.3.3 Choices for the Orbital Basis

Thus far, the electronic basis has been defined in terms of the relevant atomic orbitals. However, there are a variety of expressions that can be used to describe these orbitals. The nature of the calculation to be undertaken will largely dictate what function is used, as the choice will have a significant impact on the complexity of the calculation. When defined in spherical harmonics, a general atomic orbital can be defined as the product of two terms; the radial component $R(r)$, and the spherical harmonic $Y_{lm}(\theta, \phi)$. For the different choices of atomic orbital the spherical harmonic remains the same, and it is only the radial part that alters.

Three choices of orbital will be considered here, the hydrogen-like orbital, Slater-type orbital (STO) and the Gaussian-type orbital (GTO). The hydrogen-like functions contain a radial component defined as:

$$R_{nl}(r) = \sqrt{Z'^3 \frac{(n-l-1)!}{2n\left[(n+l)!\right]^3}} e^{-\frac{Z'r}{2}} (Z'r)^l L_{n-l-1}^{2l+1}(Z'r)\,. \tag{3.24}$$

In this equation, $L(r)$ is a Laguerre polynomial, and Z' is defined as:

$$Z' = \frac{2Z\mu}{nm_e a_0} \tag{3.25}$$

where Z is the atomic number, a_0 is the Bohr radius, and μ is the reduced mass

of the system and is defined as $\mu = \frac{m_N m_e}{m_N + m_e}$, where m_N is the nuclear mass and m_e is the mass of the electron.

The hydrogen-like orbital is found as the exact solution to the Schrödinger equation for a single electron system, and is considered a relatively accurate function in describing the electronic wavefunction in other elements. However, using the radial part of hydrogen-like functions for complex calculations is problematic, as they contain nodes, and so are not simple to integrate. As such, alternatives are often used.

STOs are one common alternative to hydrogen-like functions that are easier to work with, while maintaining many of the properties of the hydrogen-like functions. The radial component is written in the form

$$R(r) = N(n, \zeta) r^{n-1} e^{-\zeta r}, \tag{3.26}$$

where ζ is the Slater exponent, often taken to be Z_{eff}/na_0 (where Z_{eff} is the effective nuclear charge, and a_0 is the Bohr radius). $N(n, \zeta)$ is a normalisation constant defined as:

$$N(n, \zeta) = (2\zeta)^n \sqrt{\frac{2\zeta}{(2n)!}}. \tag{3.27}$$

STOs accurately describe the long range properties of the orbitals, as they decay in much the same way as the hydrogen-like functions. However, the main difference between the two is the lack of radial nodes in the STOs when compared to hydrogen-like functions. This can have implications for close range interactions, although generally STOs form an accurate orbital basis. While problems exist in analytically integrating the higher orbital levels, solutions are known for the lower orbitals as shown by Mulliken *et al.* [83] and Roothaan [84], which is sufficient to cover the majority of the work shown here. The expressions for the integrals of the s and p-type STOs need slight modification for the work here, with the modified expressions shown explicitly in appendix A.

GTOs differ from hydrogen-like orbitals and STOs in that the exponent within the radial wavefunction is a function of r^2 as opposed to simply r. This simplifies a large number of calculations as analytical expressions exist for integrating

Gaussians and their related functions, and can vastly decrease computational time. The general form for a GTO is

$$\text{GTO} = \sum_i d_i \frac{2\chi}{\pi^{3/4}} e^{-\chi r^2}, \tag{3.28}$$

where d and χ are defined according to the specific orbital of a given element, and i sums over the appropriate number of Gaussians.

The main hindrance when using GTOs is that, due to the r^2 term in the exponent, the long range behaviour is not accurately modelled. This is countered by summing over multiple Gaussian orbitals, which increase the accuracy of the basis. However, increasing the number of Gaussians increases computational time, and hence it is a trade off between accuracy and speed when choosing an appropriate basis set.

There are numerous forms of GTOs that can be constructed. The most basic form are the minimal basis sets, which are comprised of the same number of Gaussian functions for the core and valence orbitals. Common examples are the STO-3G, or STO-6G basis sets, which aim to directly model the STOs using 3 and 6 Gaussian functions respectively. The second form is split-valence sets, which treat the core and valence electrons separately. The usual notation used is of the form X-YZG, where X represents the number of Gaussian primitives used to describe the core, while Y and Z represent two basis functions (known as a double-ζ basis set) for describing the valence shell. Common examples are the 3-21G and 6-31G basis sets. Triple-ζ functions can also be constructed such as the 6-311G basis set, where the valence shell is split into three Gaussian functions. Polarised functions (represented as a *, e.g. 6-31G*), where higher lying orbitals are added to the basis set than what would be filled in the ground state, may also be formed, as can diffuse GTOs (represented by a $+$, e.g.6-31+G), which more accurately represent the tail of the wavefunction at the expense of close range accuracy.

3.4 Group Theoretical Considerations

For symmetrical molecules such as C_{60}, that forms the basis of a large portion of this work, group theoretical techniques are often used to model various aspects of the systems associated with them. However, in order to use them it is first necessary to understand some of the basic concepts of symmetry groups, and to understand the nomenclature used in describing the symmetry of a molecule. A comprehensive guide to the group theoretical techniques involved is given in many places within the literature (e.g. ref. [14]), and so only a brief overview of the key points will be given here.

3.4.1 Point Groups and Irreducible Representations

In describing the geometry of a molecule, a selection of symmetry operations may be collected which share the property that when applied to the molecule, it is left geometrically unaltered in space. It is this complete set of all of these symmetry operations that is defined as the point group which describes the molecule.

There are five different forms of symmetry operation: rotations, reflections, improper rotations, and the inversion and identity operations. Predictably, the identity leaves the system unchanged, while an inversion has the effect of moving every point in a straight line through a particular point known as the inversion centre, (usually the origin), to a new point, the same distance away as was originally found. In three dimensions, with the inversion centre at the origin, this relates to the transformation $(x, y, z) \mapsto (-x, -y, -z)$. A reflection is represented by the symbol σ, with the plane where the reflection takes place given as a subscript, while a rotation is denoted C, with the number of rotations made around the rotational axis before returning to the original position also given as a subscript, i.e. a C_5 rotation is a rotation of $\frac{2\pi}{5}$ radians. An improper rotation, S, is defined as a rotation followed by an inversion, and follows the same subscript notation. All of these symmetry operations can be written in terms of matrix representations. So, for example, in three dimensional Cartesian coordinates, a

rotation around the z axis through an angle θ is represented by the matrix:

$$\begin{pmatrix} \cos[\theta] & \sin[\theta] & 0 \\ -\sin[\theta] & \cos[\theta] & 0 \\ 0 & 0 & 1 \end{pmatrix}. \tag{3.29}$$

Likewise, all other symmetry operations have an associated matrix that represents the transformation.

Throughout this investigation, the primary concern will be with the I_h point group which describes the undistorted C_{60} molecule. This point group contains 120 of these different symmetry operations incorporating the identity and the inversion, C_2, C_3, C_5 and $(C_5)^2$ rotations, S_6, S_{10} and $(S_{10})^3$ improper rotations, and a selection of reflectional planes. When the molecule distorts from its truncated icosahedral shape, for example, through the interaction with the surface as will be considered here, some of these operations will no longer leave the molecule geometrically unaltered, and will be lost. Thus, the distorted molecule will be described by some lower point group formed from the conserved symmetry operations that is a subgroup of I_h, i.e. a group that contains some, but not all of the symmetry operations of I_h.

As the point group contains the complete set of symmetry operations it is closed under multiplication, meaning that when two operations are combined, it must have the same effect on the molecule as one of the other operations in the group. This leads to the construction of a multiplication table which shows the resultant transformation that arises from applying any two of the operations. As a simple example, if the I_h group is considered, and two C_2 rotations are considered, one rotating in the xy plane, and the other in the xz plane, the resultant transformation is the same as the C_2 rotation in the yz plane, as can be seen from the three-dimensional symmetry operations below:

$$\begin{pmatrix} -1 & 0 & 0 \\ 0 & -1 & 0 \\ 0 & 0 & 1 \end{pmatrix} \begin{pmatrix} -1 & 0 & 0 \\ 0 & 1 & 0 \\ 0 & 0 & -1 \end{pmatrix} = \begin{pmatrix} 1 & 0 & 0 \\ 0 & -1 & 0 \\ 0 & 0 & -1 \end{pmatrix}. \tag{3.30}$$

It can be shown that if the multiplication table of any group of matrices is the same as that of a particular point group, then the two groups are isomorphic, and

have the same properties [14]. The group of matrices which are isomorphic to a point group are known as matrix representations of that point group, and may be either reducible or irreducible.

For the representation to be reducible, a similarity transformation (i.e. a change in basis) may be applied to the original matrix such that the resultant matrix is found in block diagonal form. This indicates that the matrix may then be divided up into two separate forms of lower dimension. For a representation to be *irreducible*, this must not happen, with the representation having the lowest dimension possible. Thus the dimensions of a particular irreducible representation (irrep) give information relating to how many functions are needed to describe the complete space. For the I_h group there are ten irreps of various dimensions which may be used to model the point group. These irreps have particular importance when describing the MOs of a molecule, as the functions which describe the orbitals of various energy will transform according to a certain irrep [85].

Throughout this work, Mulliken's notation will be used to describe the irreps, although alternative schemes are also used within the literature. In Mulliken's notation, the irreps are denoted A or B for singlets (representations of one dimension), E for doublets, T for triplets, G for a four-fold degenerate state, and H for a five fold irrep. For the two singlet notations, A is used when the irrep is symmetric (does not change sign) under the highest n, C_n rotation, (or there are no rotations), and B is used when the irrep is antisymmetric (changes sign). A subscript may also be added to describe the transformation under inversion, where g is used if the sign stays the same, and a u represents a change in sign. Double primes are used to denote a change in sign under a σ_h reflection when no inversion exists, and single primes used when the irrep is unchanged. Finally, a subscript 1 or 2 can be added to describe the sign change under a C_2 rotation around an axis perpendicular to the main symmetry axis. 1 represents the sign staying the same, and 2 represents a change in sign. For the I_h point group, there are 10 irreps; A_g, T_{1g}, T_{2g}, G_g, H_g, and the equivalent irreps with the u subscript.

For each type of symmetry operation, the trace of the matrices of a particular irrep will all be the same, and is known as the character [85]. A character table

may be constructed for each point group containing all the characters for each of the symmetry operations and irreps. So, the character associated with a particular irrep for a particular symmetry operation may differ from that for the same irrep and different operation, and from a different irrep and the same operation. These character tables have uses when looking at the decomposition of the symmetry of a molecule to a lower point group, as will be discussed shortly. The relevant character tables needed for the work presented here are given in appendix B.

3.4.2 Projection Operators

A technique that will be utilised in the construction of the MOs is that of projection operators. This technique is based on the Great Orthogonality Theorem [86], where it is found that for any point group of symmetry G with irreducible representations Γ^i, the projection operator for each of the irreps is [87]:

$$\rho^i_{ts} = \frac{d_i}{g} \sum_{R \in G} D^i_{ts}(R)^* \hat{R} \tag{3.31}$$

where g is the order (the number of symmetry operation) of the group G, (120 for the I_h group), d_i is the dimension of the irrep Γ^i, $\hat{R}$ is a symmetry operation of the group, and $D^i_{ts}(R)^*$ is the complex conjugate of the ts^{th} element of the matrix representation of the symmetry operation $\hat{R}$.

This technique finds use when constructing MOs that are described by a particular irrep. When considering a molecule of a given symmetry, the atomic positions will transform according to the symmetry operations of this point group. As such the orbitals associated with each of these positions, will also transform in the same way. When the projection operator is applied to a single orbital, it projects out either a new, symmetry-adapted state, that is a linear combination of the orbital basis, and has the same transformation properties as the projection operator, or zero. It will be seen that this can be used when simplifying the Hückel Hamiltonian to reduce it to block diagonal form by changing the basis, allowing for easier diagonalisation of the matrix.

Chapter 4

A Simple Application: The Molecular Orbitals of Benzene

To understand some of the techniques outlined in chapter 3 it is worthwhile to use them on a simple molecular system to see the details of the calculation. With this in mind, this section will focus on using both HMO and EHMO to model the simple benzene molecule, C_6H_6. A comparison between the two methods will be given, the structure of the MOs will be considered, and theoretical STM plots will be constructed. A brief discussion will also be given relating the constant current and constant average current images that can be obtain using the dSTM technique.

4.1 Constructing the Hamiltonian Using HMO Theory

Benzene is a conjugated, planar molecule, and is therefore an ideal candidate for treatment using HMO theory. The molecular structure is shown in figure 4.1, where it can be seen that each carbon atom is bonded to two other carbons and a single hydrogen atom. The bonding between the carbons is neither consistent with a single or double C-C bond length (1.47Å and 1.35Å respectively), and is

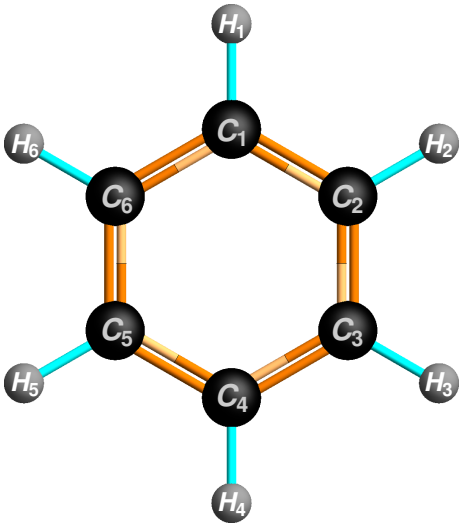

Figure 4.1: Ball & stick model of the benzene molecule showing the atomic labelling used to construct the Hamiltonian

instead found to be 1.40Å [88]. This is due to electron delocalisation, whereby the electrons involved in C-C bonding are distributed evenly amongst the six carbon atoms.

The first step to using HMO theory is to label the individual atoms with the aim of constructing the Hückel Hamiltonian. The designation of the atoms is shown in figure 4.1, although as HMO theory only relies on the π-bonding network, only the six carbon atoms need to be considered (the electrons associated with the hydrogen atoms are in the $1s$ orbital, and therefore only contributes to the σ-bonding). A p_z orbital (i.e. a p orbital pointing perpendicular to the plane of the molecule) associated with each atom forms the electronic basis, then, using the relationships given in equation (3.20) and the adjacencies shown by figure 4.1, the Hamiltonian can be constructed to give:

$$\mathcal{H} = \begin{bmatrix} \alpha & \beta & 0 & 0 & 0 & \beta \\ \beta & \alpha & \beta & 0 & 0 & 0 \\ 0 & \beta & \alpha & \beta & 0 & 0 \\ 0 & 0 & \beta & \alpha & \beta & 0 \\ 0 & 0 & 0 & \beta & \alpha & \beta \\ \beta & 0 & 0 & 0 & \beta & \alpha \end{bmatrix}. \tag{4.1}$$

This matrix may be inserted into the secular equation (equation (3.21)) with the

aim of solving for ϵ and $\vec{\Psi}$, to give:

$$\begin{bmatrix} \alpha-\epsilon & \beta & 0 & 0 & 0 & \beta \\ \beta & \alpha-\epsilon & \beta & 0 & 0 & 0 \\ 0 & \beta & \alpha-\epsilon & \beta & 0 & 0 \\ 0 & 0 & \beta & \alpha-\epsilon & \beta & 0 \\ 0 & 0 & 0 & \beta & \alpha-\epsilon & \beta \\ \beta & 0 & 0 & 0 & \beta & \alpha-\epsilon \end{bmatrix} \vec{\Psi} = 0, \tag{4.2}$$

noting that the right hand side of equation (3.21) has been written in the form $\epsilon\vec{I}\vec{\Psi}$ (with $\vec{I}$ representing the identity matrix) to allow the energy to be incorporated into the matrix. At this point, there are three unknowns in the matrix in the form of α,β and ϵ. However, if equation (4.2), is divided through by β and we define an unknown E', such that $E' = -\frac{\alpha-\epsilon}{\beta}$, the matrix simplifies greatly to the form:

$$\begin{bmatrix} -E' & 1 & 0 & 0 & 0 & 1 \\ 1 & -E' & 1 & 0 & 0 & 0 \\ 0 & 1 & -E' & 1 & 0 & 0 \\ 0 & 0 & 1 & -E' & 1 & 0 \\ 0 & 0 & 0 & 1 & -E' & 1 \\ 1 & 0 & 0 & 0 & 1 & -E' \end{bmatrix} \vec{\Psi} = 0. \tag{4.3}$$

This matrix can then be rearranged back to the standard form of the secular equation, to give the far simpler expression:

$$\begin{bmatrix} 0 & 1 & 0 & 0 & 0 & 1 \\ 1 & 0 & 1 & 0 & 0 & 0 \\ 0 & 1 & 0 & 1 & 0 & 0 \\ 0 & 0 & 1 & 0 & 1 & 0 \\ 0 & 0 & 0 & 1 & 0 & 1 \\ 1 & 0 & 0 & 0 & 1 & 0 \end{bmatrix} \vec{\Psi} = E'\vec{\Psi}, \tag{4.4}$$

This gives a purely numerical matrix (which is equal to the adjacency matrix in simple cases such as this) which is straightforward to diagonalise. The basis has remained the same throughout the manipulation, and as such the eigenvectors (MOs) may still be constructed in the same way. However, as the energy is

Table 4.1: The Hückel eigensystem of the benzene molecule with the relative energy between orbitals

E'	Eigenvector	Molecular Orbital
-2	$\left(-\frac{1}{\sqrt{6}}, \frac{1}{\sqrt{6}}, -\frac{1}{\sqrt{6}}, \frac{1}{\sqrt{6}}, -\frac{1}{\sqrt{6}}, \frac{1}{\sqrt{6}}\right)$	LUMO+1
-1	$\left(-\frac{1}{2\sqrt{3}}, -\frac{1}{2\sqrt{3}}, \frac{1}{\sqrt{3}}, -\frac{1}{2\sqrt{3}}, -\frac{1}{2\sqrt{3}}, \frac{1}{\sqrt{3}}\right)$	LUMO
-1	$\left(\frac{1}{2}, -\frac{1}{2}, 0, \frac{1}{2}, -\frac{1}{2}, 0\right)$	LUMO
1	$\left(-\frac{1}{2\sqrt{3}}, \frac{1}{2\sqrt{3}}, \frac{1}{\sqrt{3}}, \frac{1}{2\sqrt{3}}, -\frac{1}{2\sqrt{3}}, -\frac{1}{\sqrt{3}}\right)$	HOMO
1	$\left(\frac{1}{2}, \frac{1}{2}, 0, -\frac{1}{2}, -\frac{1}{2}, 0\right)$	HOMO
2	$\left(\frac{1}{\sqrt{6}}, \frac{1}{\sqrt{6}}, \frac{1}{\sqrt{6}}, \frac{1}{\sqrt{6}}, \frac{1}{\sqrt{6}}, \frac{1}{\sqrt{6}}\right)$	HOMO-1

given in terms of unknown variables, nothing absolute can be deduced about the energies of each MO. Even so, as α and β are constants, the eigenvalues E', are linearly related to the eigenvalues ϵ, and as such the method does provide the correct ordering of the MOs.

4.1.1 Finding the Molecular Orbitals

The eigenvectors, Ψ, and eigenvalues, E', can easily be obtained computationally by diagonalising the Hamiltonian giving the results shown in table 4.1. To determine which of the orbital expressions contain electrons when the molecule is in the ground state, it is necessary to order the MOs in terms of their energies, and hence the expression relating E' to the energy of the MO, ϵ, is needed:

$$\begin{aligned} E' &= -\frac{\alpha - \epsilon}{\beta} \\ &= -\frac{\alpha}{\beta} + \frac{\epsilon}{\beta}. \end{aligned} \tag{4.5}$$

As both α and β are constants, the first term will merely represent a shift of each value of E' with respect to ϵ, and will therefore not affect the overall ordering of the orbitals. However, the second term shows that E' is related to ϵ via the multiplicative constant β. β is related to the overlap of adjacent p orbitals, and importantly, will always be negative [10]. Thus, ϵ, is directly related to the *negative* of the E' values found, giving the ordering shown in table 4.1.

Electrons will fill the MOs in order of lowest energy, and so, as carbon contributes one electron to the π orbital system, in its ground state there will be two

electrons in the $E' = 2$ orbital in table 4.1, and two further electrons in each of the degenerate $E' = 1$ orbitals. This shows that for benzene, both the HOMO and LUMO are two-fold degenerate, (i.e. there are two MOs of the same energy in both cases).

Each MO can then be found from the LCAO specified by the eigenvectors in table. 4.1 which provides the coefficients for the p_z orbital associated with each atom. The p_z function itself is taken to be the STO for a carbon $2p$ orbital, which has a radial component as given in equation (3.26) for $n = 2$, and the spherical harmonic of $l = 1$ and $m = 0$, giving:

$$\left(\frac{\zeta^5}{\pi}\right)^{\frac{1}{2}} r\cos(\theta)\, e^{-r\zeta}. \tag{4.6}$$

It is useful to convert this to Cartesian coordinates to give:

$$\left(\frac{\zeta^5}{\pi}\right)^{\frac{1}{2}} z e^{-\zeta\sqrt{x^2+y^2+z^2}}. \tag{4.7}$$

For the p_z orbital of carbon, the Slater exponent is taken to be $\zeta = 1.568$, as derived by Clementi and Raimondi [89]. If the origin is defined as the centre of the benzene molecule, a simple translation is then necessary to align a p_z orbital with each atomic position. The atomic positions are assigned to the vertices of a hexagon, with an atomic separation corresponding to the accepted bond length of 1.4Å, as specified in ref. [88]. However, as the Slater exponent specifies the length in terms of the Bohr radius, a_0 the bond length is converted to atomic units to give $2.65\mathrm{a}_0$.

The MOs can be plotted by considering an isosurface in three dimensional space, as shown in figure 4.2. As an orthogonal basis is not used, the MOs are not normalised (although degenerate levels have the same normalisation constant), and so the magnitude of the contour has been chosen separately in each case to best show the features of the MO. As is convention, the blue regions represent areas of negative polarity (negative contour), and the red regions represent areas of positive polarity (positive contour).

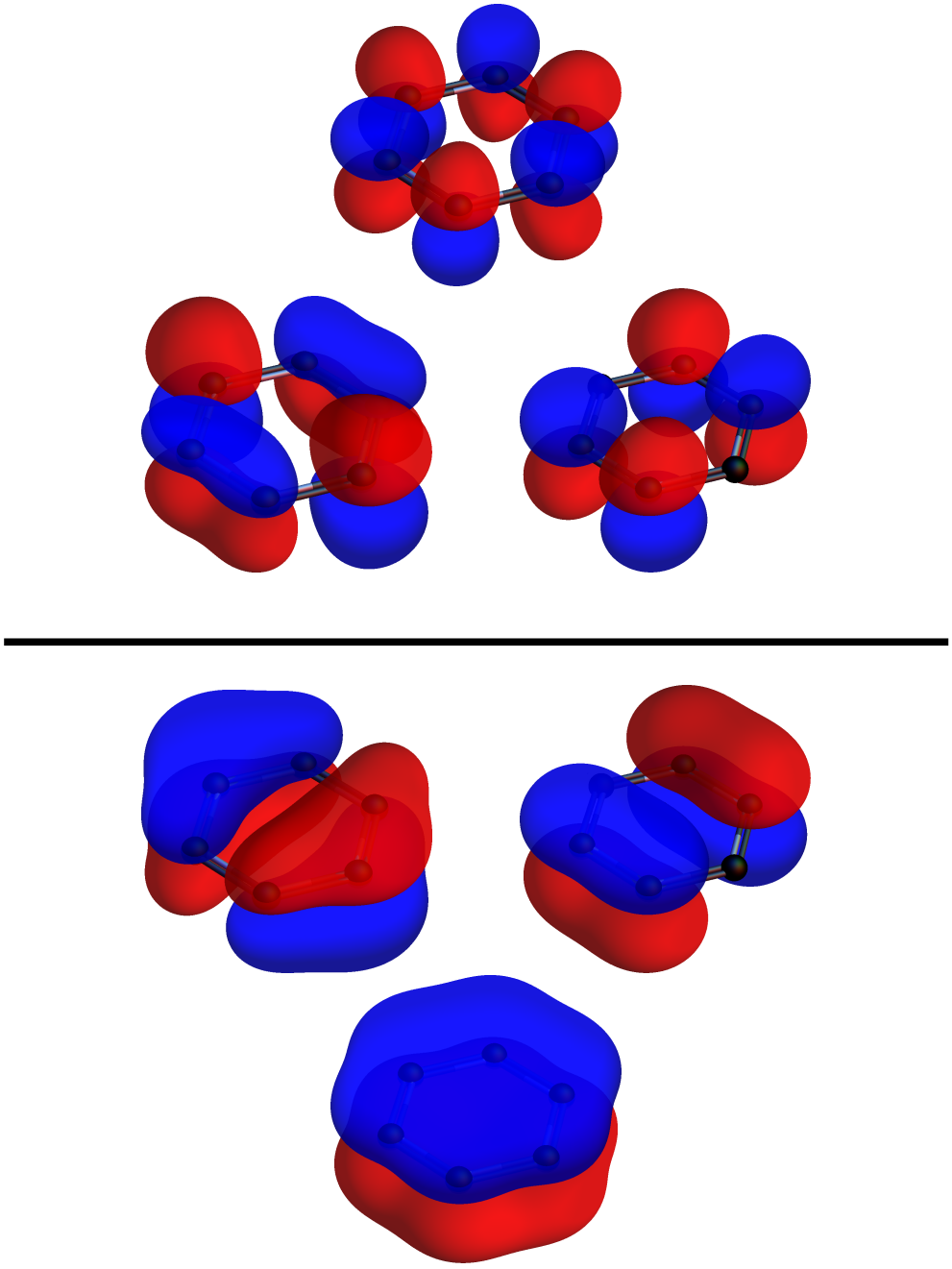

Figure 4.2: The molecular orbitals of benzene, showing, from top to bottom, the LUMO+1, the two degenerate components of the LUMO, the two degenerate components of the HOMO, and the HOMO+1.

4.2 Constructing the Hamiltonian Using EHMO Theory

Whereas HMO theory only required the p_z orbitals of the carbon atoms to construct the MOs, if EHMO theory is to be used, the basis needs to be formed of all the valence orbitals. Thus, the full MO basis consists of the $1s$ orbitals of the hydrogen atoms, and the $2s, 2p_x$ and $2p_y$, as well as the $2p_z$ orbitals of carbon. In addition to this, the overlaps between all of these need to be calculated.

The first step in constructing the Hamiltonian is to define the diagonal elements. These often take the values of the negative of the ionisation potential for the particular orbital, although they are often varied slightly from this depending on the system. Generally, this is done to 'fine tune' the specific energies to match experimental data, and so in this work, where the main concern is with the MOs and not the accurate energy, the ionisation potentials will be used.

The values used for the diagonal elements are those given by Skinner and Pritchard [90]. Each p orbital of carbon will have the same ionisation potential, and so only three different values are needed, taken in atomic units as:

$$\begin{aligned} H_{ii}^{H_{1s}} &= -0.500\mathrm{E}_H \\ H_{ii}^{C_{2s}} &= -0.786\mathrm{E}_H \\ H_{ii}^{C_{2p}} &= -0.419\mathrm{E}_H. \end{aligned} \tag{4.8}$$

This defines all of the diagonal elements needed for benzene, and then from this, equation (3.23) can be used to construct all the off-diagonal elements. However, to do this requires calculation of the electronic overlaps, S_{ij} through the integral:

$$S_{ij} = \int \psi_i \psi_j d\tau, \tag{4.9}$$

where ψ_i and ψ_j are the two orbitals, and τ indicates an integral over all space. To calculate these integrals, the atomic orbitals are taken as STOs and the expressions given in appendix A (adapted from ref. [84]) are used. The values for ζ are again those derived by Clementi and Raimondi [89], where for each of the p orbitals of carbon, $\zeta = 1.568$, and for the $2s$ state $\zeta = 1.608$. For the $1s$ hydrogen

orbitals $\zeta = 1$, as there is only a single electron and hence no shielding, which reduces the STO to the exact solution of the hydrogen Schrödinger equation.

With the atomic coordinates assigned as previously, the atomic overlaps can be calculated, and the off-diagonal elements of the Hamiltonian calculated using the Wolfsberg-Helmholtz constant of $K = 1.75$. This produces a fully numerical Hamiltonian that can be diagonalised to give the MOs and their respective energies. For planar molecules such as benzene, the p_z orbitals will have zero overlap with all other orbitals, and as such the Hamiltonian splits into block diagonal form; one block associated with the $1s$, $2s$, $2p_x$ and $2p_y$ network, and one block with the p_z network. It is for this reason that the assumption within HMO theory that only the p_z orbitals contribute, is valid for planar molecules. With the Hamiltonian split into these two blocks, it is unsurprising that upon diagonalisation, the MOs that arise from the p_z orbital network are the same in both EHMO theory and HMO theory. In addition to this, when considering the electron occupancy of all of the MOs, both HMO theory and EHMO theory predict the same frontier orbitals.

Using EHMO theory has the additional benefit that as the overlap integrals have all been undertaken, it is straightforward to normalise the MOs. For a particular MO, Ψ, that is a LCAO such that $\Psi = \sum_i c_i \psi_i$, normalisation requires that:

$$\int \left(N \sum_i c_i \psi_i \right)^2 d\tau = 1, \tag{4.10}$$

where i sums over all atomic orbitals, c is the coefficient defined by the LCAO, and N is a normalisation constant. Solving this for N and noting the relationship

for the overlap given in equation (4.9), gives:

$$\begin{aligned}
\int \left(N \sum_i c_i \psi_i \right)^2 d\tau &= 1 \\
N^2 \int \sum_i \sum_j c_i c_j \psi_i \psi_j d\tau &= 1 \\
N^2 \sum_i \sum_j c_i c_j \int \psi_i \psi_j d\tau &= 1 \\
N^2 \sum_i \sum_j c_i c_j S_{ij} &= 1 \\
N &= \left(\sum_i \sum_j c_i c_j S_{ij} \right)^{-\frac{1}{2}}
\end{aligned} \tag{4.11}$$

4.3 Simulating a Constant Current STM Image

To conclude the brief investigation of benzene, a constant current image of the LUMO will be constructed for the case of a simple s-type tip state to show the details of the method used. Constant height STM images are not considered at all in this investigation as, even though they are very simple to construct, the majority of experimentally obtained images in the literature are either constant current or constant average current dSTM images. Indeed, the comparisons made between theory and experiment in this work are almost exclusively with these two techniques.

It has been shown by Tersoff and Hamann [77] that, for an s-type tip, the current observed during STM is proportional to the sum of the squares of the MOs under consideration, evaluated at tip position (x, y, z). In the theoretical model, a value is chosen to represent the current, I', that is related to the true current by some proportionality constant. The derivation of this constant is complicated as it requires knowledge of the tunnelling transition probability, and hence, accurately determining the tunnelling matrix element. However, its derivation is not necessary when constructing qualitative images, where a value for I' can be chosen to form a 'best match' with experiment.

As I' is related to the MO functions, the value that would be observed at any

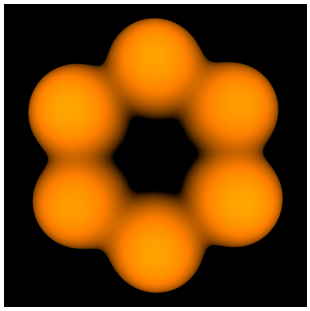

Figure 4.3: A simulated constant current STM image of the two fold degenerate LUMO of benzene where $I' = 0.001$

point in space is a function of x, y and z only, and is of the form:

$$\sum_{i}^{j} \Psi_i \left(x, y, z\right)^2 = I', \tag{4.12}$$

where Ψ_i is the ith MO for an j-fold degenerate state. To form a theoretical image, the height adjustment of the tip is taken to always be along the z axis, with the raster scan taking place over x and y. To obtain the correct tip height, the particular values of x and y are fixed, and equation (4.12) is solved for the remaining unknown z for a fixed I'. In fact, there are multiple solutions to this equation, and so the highest solution of z is taken for the tip height, corresponding to the point at which the tunnelling current would first be observed by an s orbital approaching the sample from above. The equation is then repeatedly solved with different values of x and y as the tip scans across the sample, producing an array of values for the tip height. It is this three dimensional data that is then plotted to produce a simulated image. The image in figure 4.3 shows the two fold degenerate LUMO of benzene, where the effective current has been produced by summing over the contributions of both orbitals, as specified in equation (4.12).

4.3.1 Dynamic STM

As an experimental alternative to the constant current technique, dSTM may be used where the probe is oscillated at a given frequency and the average current used to produce the image. However, from a theoretical perspective the two methods can be approximated in the same way, as, due to the exponential decay of the p orbitals that make up the MOs, the main contribution to the average

tunnelling current will be when the tip is at its peak amplitude. Any contribution below this is expected to be negligible due to the rapid decay of the sample wavefunction.

To verify these assumptions, it is also possible to directly model the dSTM technique and compare it with the results for the constant current simulation. This is undertaken by assuming that the tip oscillates in the z direction as a simple harmonic oscillator, meaning that the following transformation can be applied to the square of the MO to obtain the effective current as a function of time:

$$z \mapsto z' + A\cos\left[2\pi\omega t\right], \tag{4.13}$$

where z' is the point around which the tip oscillates, A is the amplitude, ω is the frequency of oscillation, and t is the time. Approximate values for the amplitude and frequency may be taken by comparison with experimental parameters, which vary significantly depending on the experimental settings chosen.

With this transformation applied, the MO now contains two unknowns, z' and t, for each position in x and y. If it is assumed that ω is much shorter than the time spent at each position of the raster scan, I' can be accurately modelled as an integer multiple of the contribution from a single period of oscillation. Thus, by integrating with respect to t over a single period, a value proportional to the effective current will be obtained, and a function of the tip height, z', only, is produced. This can then be solved in the same way as for the constant current simulation to produce a plot, although the added complexity of the calculation due to the evaluation of the integral, significantly increases the time taken to produce the images.

Figure 4.4 again shows the LUMO of benzene, but this time modelled as if obtained via a dSTM method. The value of the effective current in this image has been chosen to most closely resemble the image in figure 4.3, where by comparison it can be seen that no noticeable difference can be observed from the two methods.

As stated, the exponential nature of the current-tip height relationship ensures that only the current at the peak amplitude significantly contributes. It should be

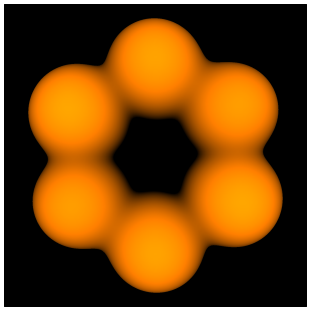

Figure 4.4: A simulated dynamic STM image of the two fold degenerate LUMO of benzene. I' was chosen to best match the image in figure 4.3, resulting in an indistinguishable image being produced.

noted that this assumption would not be valid if the tip was pushed deeper into the sample where the electron density reaches a peak, and the exponential relationship is no longer an accurate representation of the observed current. However, this corresponds to a tip-sample separation that appears to be much smaller than that used experimentally, and as such it is safe to use the assumption throughout.

Chapter 5

The Neutral C_{60} Molecule

The main body of this work is concerned with C_{60}, and it is this that shall now become the main focus in this section. Firstly, EHMO and HMO theory will be utilised to construct the MOs of the isolated molecule, and the two techniques are compared to show the validity of HMO theory for this system. Theoretical STM images will be constructed for the idealised case where no external interaction is present, after which two different methods for introducing this will be presented, and the effects on the theoretical images shown. The effect of the tip structure will be considered through the use of the derivative rule, before using this to look at the images that are obtained when a tip-adsorbed C_{60} interacts with the Si(111)-(7x7) surface, in work we have published in *Physical Review Letters* [91].

5.1 Constructing the Molecular Orbitals

As with the example considered previously, where theoretical STM images of benzene were constructed, the first step is to obtain expressions for the MOs of the molecule. The simplest way to do this is to use HMO theory, and only consider the π bonding network. Usually, HMO theory is used with planar molecules, and it is simply a case of taking a p orbital normal to the plane of the molecule associated with each atomic position as the basis set. However, as

C_{60} is three dimensional it is instead necessary to define the basis as the set of 60 p orbitals pointing radially outwards from each atomic position, as it will be these that contribute to the π bonding.

The p-type STO is used with the Slater exponent taken as 1.568 [89], as used in benzene in chapter 4. To construct a radial p_r orbital a linear combination of p_x,p_y and p_z orbitals is taken. For the orbital to point radially outwards, the molecule is centred at the origin, and the dot product is taken between the normalised atomic position, and three p orbitals i.e.:

$$\frac{1}{\sqrt{a_x^2+a_y^2+a_z^2}}\left(a_x,a_y,a_z\right)\cdot\left(p_x,p_y,p_z\right), \tag{5.1}$$

where (a_x, a_y, a_z) is the atomic coordinate of the atom with which the p orbital is associated.

Substituting the Cartesian expression for the p-type STO into equation (5.1), and translating the function so it is centred on the atomic coordinate gives the expression for a generic p_r orbital of C_{60} as:

$$p_r = \frac{1}{\sqrt{a_x^2+a_y^2+a_z^2}}\left(a_x(x-a_x)+a_y(y-a_y)+a_z(z-a_z)\right)\times \left(\frac{1.568^5}{\pi}\right)^{\frac{1}{2}} e^{-1.568\sqrt{(x-a_x)^2+(y-a_y)^2+(z-a_z)^2}}. \tag{5.2}$$

This general expression can then be used to construct the 60-fold electronic basis.

In the same way as described for the benzene molecule, the Hückel Hamiltonian can be constructed by looking at the adjacency of the atoms and assigning the elements of the Hamiltonian matrix accordingly. However, unlike the benzene molecule, the neighbouring interatomic distances vary, with the 6-6 bonds experimentally observed to be shorter than the 5-6 bonds. To incorporate this into the Hückel Hamiltonian, the resonance integral corresponding to a 6-6 bond is given the value β_d, while that associated with a 5-6 bond is given the value β_s. The two may then be related together as given by Hands *et al.* [64], where the ratio between them is taken as 1.433, i.e.:

$$\beta_s = \frac{\beta_d}{1.433}. \tag{5.3}$$

Table 5.1: Relative energies (as a function of the Hückel parameters α and β), degeneracies and the irreducible representation that describes the different MOs of undistorted C_{60}, obtained through HMO theory

E' (3 d.p.)	Degeneracy	Irrep	Level
-2.396	1	A_g	HOMO-7
-2.203	3	T_{1u}	HOMO-6
-1.843	5	H_g	HOMO-5
-1.384	4	G_u	HOMO-4
-1.343	3	T_{2u}	HOMO-3
-0.919	4	G_g	HOMO-2
-0.823	5	H_g	HOMO-1
-0.605	5	H_u	HOMO
0.376	3	T_{1u}	LUMO
0.569	3	T_{1g}	LUMO+1
0.968	5	H_g	LUMO+2
1.077	3	T_{2u}	LUMO+3
1.303	5	H_u	LUMO+4
1.617	4	G_g	LUMO+5
2.082	4	G_u	LUMO+6
2.129	3	T_{2g}	LUMO+7

The relationship between the two is then utilised so that only one of β_s or β_d remains. The choice is arbitrary, and will only change the units in which the relative energy is expressed (either as a function of β_d or β_s). Here, all overlaps between the 5-6 bonds are given as a function of β_d, such that only β_d remains. For clarity, in the remainder of the work this will simply be denoted β.

Using this relationship, a 60x60 Hückel Hamiltonian can be constructed, with the eigenvalues and eigenvectors found computationally by diagonalising the Hamiltonian, producing the mathematical functions that represent the MOs as well as their relative energies. Again, it should be noted that as β is a negative value, the energy relates to the negative of the eigenvalues. For the neutral, undistorted molecule, the relative energies and degeneracies are shown in table 5.1.

The irreps which represent each MO are obtained through the use of the projection operator technique described in section 3.4.2. The matrix representations of the different irreps that make up the icosahedral group have been taken from ref. [92], and utilised to obtain the different forms of projection operator. Applying each of the projection operators to an individual atom (it is not important which one), a new 60 fold basis is projected out comprising of a linear com-

Table 5.2: Functions that transform as the components of the LUMO and the HOMO of C_{60}

Component	Function
T_{1u_x}	x
T_{1u_y}	y
T_{1u_z}	z
H_{u1}	$8\sqrt{3}xyz\left(1-3z^2-\sqrt{5}\left(x^2-y^2\right)\right)$
H_{u2}	$-8xyz\left(3\left(x^2-y^2\right)+\sqrt{5}\left(1-3z^2\right)\right)$
H_{u3}	$x\Big((1-3x^2)(9-11x^2)-3(y^2-z^2)^2-2\sqrt{5}(1-3x^2)(y^2-z^2)\Big)$
H_{u4}	$y\Big((1-3y^2)(9-11y^2)-3(z^2-x^2)^2-2\sqrt{5}(1-3y^2)(z^2-x^2)\Big)$
H_{u5}	$z\Big((1-3z^2)(9-11z^2)-3(x^2-y^2)^2-2\sqrt{5}(1-3z^2)(x^2-y^2)\Big)$

bination of the individual p orbitals (known as symmetry adapted states). The transformation matrix associated with this may then be applied to the Hamiltonian to convert it to this new basis, resulting in a block-diagonal matrix that can be diagonalised to produce the MOs, revealing the degeneracies of each level and their symmetry transformation properties, giving the results in table 5.1.

These irreps can be compared to the results given by Chancey and O'Brien [93], which largely match those found here. The exception being that in the previous work, the HOMO-1 and HOMO-2 were found to be the same energy, leading to a nine fold, accidentally degenerate state represented by the $G_u \oplus H_g$ irreps. This would also be the case here if the 5-6 and 6-6 bonds were assumed to be the same length, but by including the more physical representation where the 6-6 bond is taken to be slightly shorter than the 5-6 bond, this level splits into the four fold and five fold degenerate levels shown in table 5.1.

Through the symmetry adapted states, the linear combination of the p orbitals is obtained from the eigenvectors of the transformed Hamiltonian. Each set of degenerate MOs form a basis set which transform according to the associated irrep, allowing them to be modelled using functions that have the same transformation properties. Throughout this work the energy levels that undergo the most consideration will be the HOMO and the LUMO. The components, i.e. the individual MOs, for the LUMO will be labelled T_{1u_x}, T_{1u_y} and T_{1u_z}, while for the HOMO, the components will be denoted $H_{u1}, H_{u2}, H_{u3}, H_{u4}$ and H_{u5}.

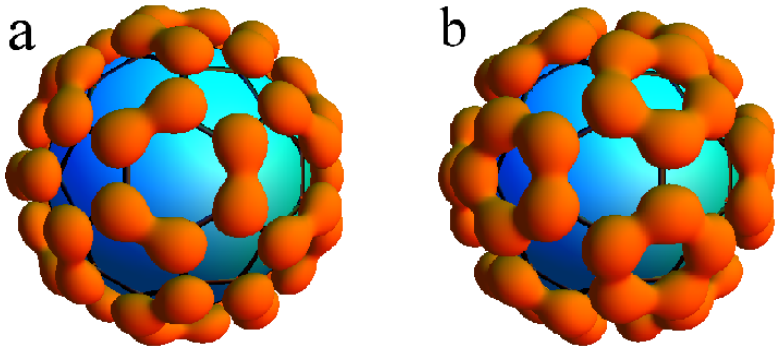

Figure 5.1: The electron distribution of the a, HOMO, and b, LUMO of C_{60}, constructed via HMO theory. The contour values for the simulations are chosen to best show the electronic distribution

The transformation properties of these MOs are listed in table 5.2, where the x,y, and z axes are all defined to have a C_2 symmetry axes. For cases where the basis functions need defining with a different definition of the x, y and z axes, it is simply a case of rotating the basis functions accordingly. To ascertain which MO corresponds to which component, it is necessary to compare the transformation properties of both the MO and the associated function when the symmetry operations of the I_h point group are applied. By associating the functions and the MOs that have equivalent transformation properties, the correct MO can be assigned.

Figure 5.1 shows the electron distribution for the degenerate HOMO and LUMO of C_{60} obtained via HMO theory. The plots are formed from the sum of the squares of the degenerate states, with the contour value chosen to best show the difference between the HOMO and LUMO of C_{60}. It can be seen the electrons are predominantly associated with the 6-6 bonds for the HOMO, and with the 5-6 bonds for the LUMO.

5.1.1 Verifying the Results Through EHMO Theory

As mentioned, HMO theory is primarily used for planar molecules, and as such it is not immediately obvious that it should still be valid when looking at three dimensional molecules such as C_{60}. Indeed, there are numerous molecules which can not be accurately modelled using HMO theory. However, we can gain evidence that the technique accurately predicts the MOs in C_{60} through the use of

EHMO theory.

The full electronic basis consists of the $2s, 2p_x, 2p_y$ and $2p_z$ carbon orbitals centred at each atomic position, resulting in MOs that are linear combinations of 240 atomic orbitals. As with benzene, STOs are used, and as such the expressions found in appendix A are used to evaluate the overlaps, and again the diagonal elements of the Hamiltonian are taken to be -0.786E_h for the $2s$ orbitals and -0.419E_h for the $2p$ orbitals.

In benzene, the Hamiltonian produced could be divided into block diagonal form, with the p_z orbitals forming a separate block to the remainder of the Hamiltonian, and hence the MOs associated with these orbitals were identical in both EHMO and HMO theory. For C_{60}, as the basis is comprised of radial p_r orbitals in HMO theory, and p_x, p_y, p_z orbitals in EHMO theory, the Hamiltonian does not break down into such a simple form, and the same comparison can not be made between the methods.

To solve this, the electronic basis could be altered for the EHMO Hamiltonian such that radial p orbitals are used, and two orbitals orthogonal to this chosen to complete the p basis. However, as we will only really be concerned (at least initially) with the HOMO and LUMO of C_{60}, it is simpler to plot the predicted MOs and compare the results visually. When this is done, it is found that both the HOMO and LUMO are visually the same for the two methods. Although mathematically a contribution is predicted from the $2s$ orbitals using EHMO theory, this contribution is small, and the higher rate of decay of the $2s$ orbital, means that it's contribution to the MO at the distances observed during STM is negligible.

Figure 5.2 shows a comparison between the five-fold degenerate HOMO of C_{60} as obtained through (a) HMO theory, (b) EHMO theory and (c) DFT, as found in ref. [60]. As expected, there is little difference between the images obtained from the three methods, verifying the use of HMO theory for simulating STM of C_{60}. It should also be noted that although not shown here, the LUMO of C_{60} is also predicted to be the same in all three techniques. From this point, all MOs

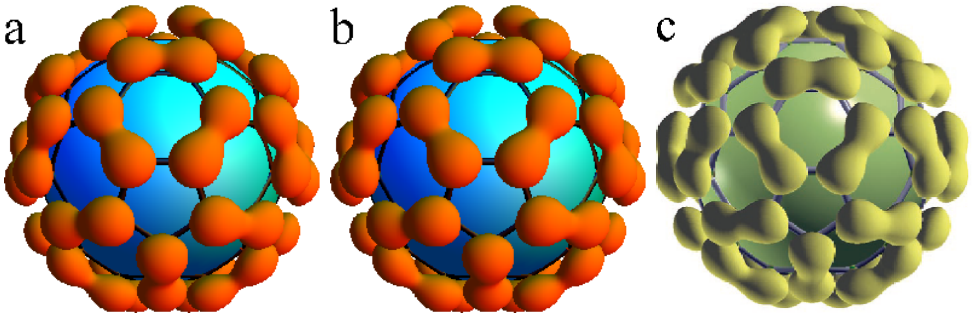

Figure 5.2: The electron distribution of the HOMO of C_{60} found using (a) HMO theory, (b) EHMO theory, and (c) DFT (from ref. [60]). For (a) and (b), the contour value is chosen to best match the DFT simulation in (c)

shown will be derived through HMO theory unless otherwise stated.

5.2 Incorporating a Surface Interaction

When imaging molecules during SPM, they are necessarily adsorbed on to a surface. This bonding interaction is expected to cause a splitting in the energies of the MOs that make up the molecule, the effects of which may be observable, particularly in STM, where only the frontier orbitals are imaged. The exact nature of this bonding will be dependent on both the surface and molecule under consideration, and so it is not necessarily straightforward to see how the images would be affected.

In order to obtain a universal model that incorporates the surface interaction, certain assumptions need to be made. In the following sections, two distinctly different approaches are given to produce theoretical STM images of C_{60}, which may both be used in different circumstances. Firstly, a group theoretical approach will be utilised that models the molecular distortion the surface interaction introduces via a change in symmetry. The second method will involve constructing a simple diagonal Hamiltonian that alters the potential and kinetic energy of the electrons associated with each orbital as a function of the distance from the surface.

5.2.1 The Group Theoretical Approach

When C_{60} is adsorbed on to a surface, the interaction between the molecule and surface is likely to induce a molecular distortion, and hence a reduction in symmetry. To model this, the surface is treated as a homogeneous plane in x and y, with the only interaction between the molecule and the surface being in the z direction, i.e. perpendicular to the surface. A similar idea has been used previously in conjunction with DFT calculations in ref. [72] where a uniaxial compression perpendicular to the surface was used to construct the MOs of a surface-adsorbed C_{60}. The bonding mechanism is assumed to have the effect of displacing the atomic positions, with the atoms closest to the surface affected to a greater extent than for those further away. As such, some of the symmetry operations which describe the undistorted molecule are not preserved, leading to the geometry being described by a subgroup of the initial I_h point group.

Introducing the surface interaction in this way makes it relatively straightforward to determine what symmetry operations would remain. Clearly, any rotations that are not in the z plane will not be permitted, the inversion operation will be lost, so no improper rotations will be allowed, and only reflections that act in a plane containing z will survive. For example, if a C_{60} molecule was situated on the surface with a 6-6 bond (C_2 symmetry axis) prone, the only surviving symmetry operations would be a C_2 rotation, and two reflections, one in a plane along the line of the 6-6 bond prone to the surface, and one perpendicular to it. These symmetry operations can then be matched against the tables of the different point groups (see appendix B), where it can be seen this particular case corresponds to the C_{2v} point group.

In order to then obtain information about whether particular levels are degenerate, it is necessary to examine the character tables for the point group describing the distorted molecule. As an example, we can consider the case of the three fold degenerate LUMO for undistorted C_{60} that is described by the T_{1u} irrep. As it is degenerate, there are three MOs that describe the electron distribution which are equivalent in energy. By finding the point group associated with the

distorted molecule, it is possible to apply each of the surviving symmetry operation to each component of the T_{1u} irrep to find the appropriate characters. By comparing these with the characters of the reduced point group, it can be seen which levels are non degenerate (those levels that match the characters for either A or B irreps), and what linear combination of the orbitals is needed to match the characters for a two fold degenerate (E irrep) level. However, as this method purely considers the splitting of degenerate orbitals from a group theoretical perspective, it does not provide information pertaining to the relative energies of the orbitals. This means that it is not possible to incorporate a strength for the surface interaction, merely to say that an interaction occurs of sufficient strength to change the energy of the MOs, and remove the degeneracies.

To find the characters for each symmetry operation of the lower point group to which the molecule distorts, it is necessary to work out how the MOs transform for each. These are made up of linear combinations of p orbitals, which in turn are dependent on the atomic positions, and as such, by finding out how the atoms transform, the transformation of the MOs can also be derived. To do this, a three dimensional matrix representation of a form of each symmetry operation is constructed, (noting that only one form of each operation needs to be calculated as the character is the same), and applied to each atomic position. As each component of the degenerate levels forms a basis, the transformed MOs must by necessity be formed via a linear combination of the original MOs. There therefore exists a matrix that acts on the original basis to produce the transformed functions, i.e. for the LUMO, there exists a function:

$$\begin{bmatrix} & & \\ & M & \\ & & \end{bmatrix} \begin{bmatrix} T_{1u_x} \\ T_{1u_y} \\ T_{1u_z} \end{bmatrix} = \begin{bmatrix} T'_{1u_x} \\ T'_{1u_y} \\ T'_{1u_z} \end{bmatrix}, \tag{5.4}$$

where M is the desired 3x3 matrix, and T'_{1u_i} is the transformed ith component of the T_{1u} orbital. For other levels described by different irreps, the dimensions of M will change accordingly.

As both the untransformed and transformed components of the MOs are known, it is simply a case of expanding out the matrices and solving the resultant si-

Table 5.3: Characters produced for the components of the LUMO when reduced to C_{3v} symmetry. $T^H_{1u_i}$ indicates the ith component of the LUMO as defined with the z component along an axis in line with a hexagon

Orbital	Component	I	C_3	σ_v
LUMO	$T^H_{1u_x}$	1	$-\frac{1}{2}$	1
	$T^H_{1u_y}$	1	$-\frac{1}{2}$	-1
	$T^H_{1u_z}$	1	1	1

multaneous equations for the matrix elements. Whilst it appears at first glance that there are not sufficient known variables to solve for all the elements in the matrix, it should be noted that each function is a combination of p orbitals and so the coefficient for each orbital is an independent variable, and as such there are in fact many more equations than variables to be solved for.

The character associated with each component of the irrep is the appropriate diagonal element of this matrix M. It is then simply a case of comparing this character with the characters for the appropriate subgroup, to determine how each component transforms. For example, for the hexagon prone molecule, the symmetry will be reduced to the C_{3v} point group, resulting in the characters for each component of the LUMO shown in table 5.3. By comparison with the character table for the C_{3v} point group (appendix B), it can be seen that the $T^H_{1u_z}$ component (where the superscript H represents a hexagonal face aligned with the z axis, and hence a reduction to C_{3v} symmetry) transforms as the A_1 irrep, and that $T^H_{1u_x}+T^H_{1u_y}$ (i.e. the sum of the characters) transforms as the two dimensional E irrep, indicating that these two components are degenerate. As the surface has been treated in the z direction only, this result is expected, as nothing has been introduced that could change the energy in the x and y directions, and it is these components that remain degenerate.

The complete set of results for both the LUMO and HOMO for all the point groups which may describe the distorted molecule are shown in tables 5.4 - 5.7, with the exception of the lowest C_1 point group (which contains only the identity operation) where only one irrep may describe the point group, and hence all components transform as this. This lack of symmetry would occur when the molecule is situated with no reflectional plane along the z axis. For the other orientations,

the symmetry will be reduced to C_s symmetry (with a single reflectional plane), except for when a 6-6 bond (C_{2v}), pentagonal face (C_{5v}), or the aforementioned hexagonal face (C_{3v}) are prone to the surface. The superscripts used in labelling the various components are given to describe the molecular orientation with ^{H} representing a hexagonal face in the z direction and a reduction to C_{3v}, ^{P} a pentagonal face (C_{5v}), ^{D} a 6-6 bond (C_{2v}), and ^{S} the various orientations where the reduction is to C_s symmetry

Table 5.4: Characters produced for the components of the LUMO when reduced to C_{3v} symmetry

Orbital	Component	I	C_3	σ_v	Irrep
LUMO	$T^H_{1u_x} + T^H_{1u_y}$	2	-1	0	E
	$T^H_{1u_z}$	1	1	1	A_1

Table 5.5: Characters produced for the components of the HOMO and LUMO when reduced to C_{5v} symmetry

Orbital	Component	I	C_5	C_5^2	σ_v	Irrep
HOMO	H^P_1	1	1	1	-1	A_2
	$H^P_2 + H^P_5$	1	$-\phi$	ϕ^{-1}	-1	E_2
	$H^P_3 + H^P_4$	1	ϕ^{-1}	$-\phi$	1	E_1
LUMO	$T^P_{1u_x} + T^P_{1u_y}$	1	ϕ^{-1}	$-\phi$	1	E_1
	T^P_{1uz}	1	1	1	1	A_1

Table 5.6: Characters produced for the components of the HOMO and LUMO when reduced to C_{2v} symmetry

Orbital	Component	I	C_2	σ_{xz}	σ_{yz}	Irrep
HOMO	H^D_1	1	1	-1	-1	A_2
	H^D_2	1	1	-1	-1	A_2
	H^D_3	1	-1	1	-1	B_1
	H^D_4	1	-1	-1	1	B_2
	H^D_5	1	1	1	1	A_1
LUMO	$T^D_{1u_x}$	1	-1	1	-1	B_1
	$T^D_{1u_y}$	1	-1	-1	1	B_2
	$T^D_{1u_z}$	1	1	1	1	A_1

In these tables there are a few important points that need to be highlighted. In table 5.4 only the irreps associated with the LUMO are shown. This is because, when calculating the characters for the five components of the HOMO a problem

Table 5.7: Splitting of the HOMO and LUMO, for a C_{60} molecule distorted to C_s symmetry

Orbital	Component	Irrep
HOMO	H_1^S	A''
	H_2^S	A''
	H_3^S	A'
	H_4^S	A''
	H_5^S	A'
LUMO	$T_{1u_x}^S$	A'
	$T_{1u_y}^S$	A''
	$T_{1u_z}^S$	A'

arises from the characters formed for all but the H_1^H component. From the characters for the other four components, two doublets are formed. However, as they both transform as E, there is no way to determine what the correct combinations are from the group theory alone. Thus, for this orientation, this method can only provide us with information on the H_1^H component which transforms as A_2.

A similar problem occurs when the symmetry of the molecule is reduced to C_s shown in table 5.7. Here, the only information that can be obtained regarding the form of the singlets is that of the $T_{1u_y}^S$ component which transforms as A''. The remaining components all have at least one other which transforms in the same way, and hence the exact form of all the other singlets can not be deduced.

From this information it is possible to construct theoretical STM images of the split MO levels. As discussed in section. 3.1.2, when an s-type tip state is considered, the observed current is proportional to the square of the MO being imaged. This makes constructing an image straightforward for the known singlets, as it is simply a case of plotting the square of that function. Constructing theoretical images for the doublets requires a little more consideration. The group theory shows that some arbitrary doublet, χ, is formed from two orthogonal components, ψ_1 and ψ_2 that form the components transforming as the E irrep. However, the group theory does not tell us what linear combination of these two components form the correct basis states, remembering that the current is the sum of the square of all degenerate levels. Luckily, when deriving the current, this problem is resolved.

If the two orthogonal basis states, (ψ_1' & ψ_2') are taken such that:

$$\begin{aligned}\psi_1' &= \xi_1\psi_1 + \xi_2\psi_2 \\ \psi_2' &= -\xi_2\psi_1 + \xi_1\psi_2,\end{aligned} \tag{5.5}$$

the observed current for the doublet would obey the proportionality relationship:

$$I \propto \psi_1'^2 + \psi_2'^2. \tag{5.6}$$

Expanding this out in terms of the initial components gives:

$$\begin{aligned}I &\propto (\xi_1\psi_1 + \xi_2\psi_2)^2 + (-\xi_2\psi_1 + \xi_1\psi_2)^2 \\ &\propto \xi_1^2\psi_1^2 + \xi_2^2\psi_2^2 + \xi_1\xi_2\psi_1\psi_2 + \xi_2^2\psi_1^2 + \xi_1^2\psi_2^2 - \xi_1\xi_2\psi_1\psi_2 \\ &\propto \left(\xi_1^2 + \xi_2^2\right)\left(\psi_1^2 + \psi_2^2\right).\end{aligned} \tag{5.7}$$

Assuming ψ_1' and ψ_2' are correctly normalised, (i. e. $\xi_1^2 + \xi_2^2 = 1$) this reduces to:

$$I \propto \left(\psi_1^2 + \psi_2^2\right), \tag{5.8}$$

which is simply the sum of the squares of the components of the initial icosahedral irreps that make up the doublet. Thus, when constructing a theoretical STM image it is not necessary to know the linear combination that forms the true basis of the orbital, knowledge of the icosahedral basis set is sufficient. Here, the normalisation of the two MOs is important in this relationship holding. As mentioned, as the p_r orbitals that form the electronic basis are not orthogonal to each other, this normalisation is not guaranteed. However, it *is* found that the degenerate components all have the same normalisation constant, and so the proportionality relationship in equation (5.8) still holds, as $\xi_1^2 + \xi_2^2$ is still equal to a constant, even if it is not unity.

An example of a theoretical scan produced by this method, the E_2 doublet of the HOMO for the pentagon prone C_{60} is visualised in figure 5.3, with the tip treated as an idealised s-type orbital. Alongside this image is a second theoretical image produced through DFT, and an experimental image, both taken from ref. [72]. It can be seen that the difference between the two theoretical approaches is almost indistinguishable, while an excellent match is also obtained

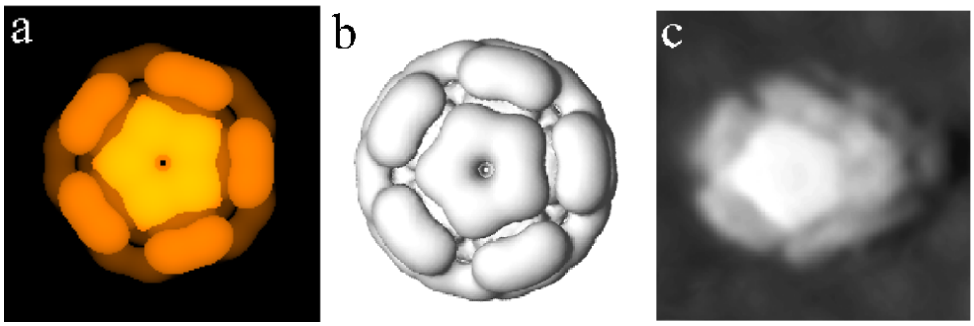

Figure 5.3: Comparison between (a) the theoretical STM image constructed using HMO theory alongside a symmetry lowering distortion, (b) the predicted orbitals obtained via DFT [72], and (c) an experimental STM image [72], for the E_2 doublet of the HOMO of a pentagon prone C_{60}.

with the experimental image. It should be noted that the image obtained through DFT is a three dimensional plot of the square of the MOs and not a theoretical STM scan, which accounts for the differences in the colour scaling of the two images.

5.2.2 Constructing a Simple Surface Hamiltonian

An external interaction may also be incorporated by directly modifying the diagonal elements of the Hückel Hamiltonian to model the effect of the interaction on the kinetic and potential energy of the electrons associated with the p orbitals of each atom. A function is constructed that perturbs the energy of the orbitals closer to the surface by a greater extent to those further away, essentially treating the interaction uni-axially and perpendicular to the surface as was considered in the group theoretical approach.

A Hamiltonian can be constructed that represents this energy change, giving the Hamiltonian for the system as:

$$\mathcal{H} = \mathcal{H}_H + \mathcal{H}_S, \tag{5.9}$$

where $\mathcal{H}_H$ is the Hamiltonian constructed from either HMO or EHMO theory, and $\mathcal{H}_S$ is the Hamiltonian representing the surface interaction. $\mathcal{H}_S$ takes the

simple diagonal form:

$$\mathcal{H}_{S_{ii}} = E_{S_i}(z) \tag{5.10}$$

$$\mathcal{H}_{S_{ij}} = 0, \tag{5.11}$$

where $E_{S_i}(z)$ is the energy function acting on the ith atomic orbital.

In this work, $E_{S_i}(z)$ is taken to be a LJ type potential to give an approximation to the true interaction between surface and molecule. When using HMO theory, the energy function must take units of the unknown β to match the units of the eigenvalues. In this case, a multiplicative constant is introduced, and it is only necessary to define the distance, r_m, at which the potential reaches a minimum. This is taken to be 10.34a_0 corresponding to a typical C-Si bond length (as the majority of the work will be with C_{60} adsorbed on Si(111)-(7x7)), with the molecule then situated with the lowest atom 10.34a_0 from the plane defined by the LJ potential. In fact, it is found that this value does not have a significant effect on the results as long as it is within sensible bounds. The energy function is therefore taken to be:

$$E_{S_i}(z) = \upsilon\left(\left(\frac{10.34}{r_i}\right)^{12} - 2\left(\frac{10.34}{r_i}\right)^{6}\right), \tag{5.12}$$

where r_i is the distance perpendicular to the implied surface of the function, and υ is a constant that is used to alter the strength of the interaction. Again, it is found that the value chosen for υ does not have a significant effect on the MOs predicted unless exceptionally large. The value chosen here is $\upsilon = -0.001\beta$, to allow for the fact that β is negative.

Using E_{S_i}, the surface Hamiltonian H_s can be constructed to produce a 60x60 diagonal matrix which can then be added to the Hückel Hamiltonian to produce the full matrix for the system. Diagonalising this Hamiltonian then provides the MOs, and reveals any degeneracies for a specific molecular orientation. It is found that the images produced are identical to those produced using the group theoretical method, an example of which is shown in figure 5.4, where the H_5^D component is plotted using both techniques, alongside a theoretical image produced through DFT by Pascual [72]. It can be seen that there is no observable

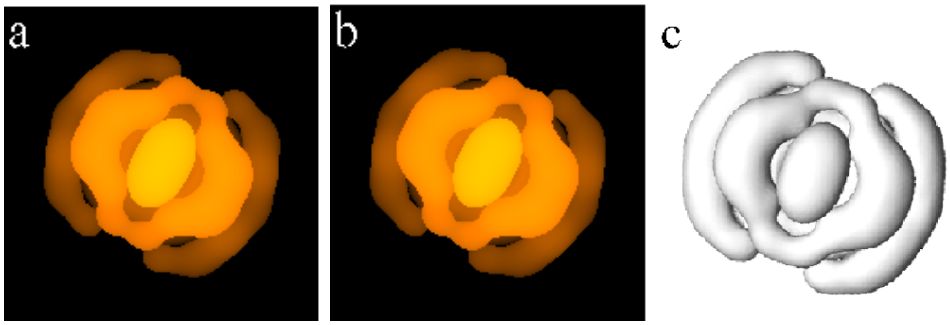

Figure 5.4: Comparison between (a) the theoretical STM image constructed through a surface Hamiltonian for the H_5^D component of the HOMO (b) the theoretical STM image constructed using HMO theory alongside a symmetry lowering distortion, (c) the predicted orbitals obtained via DFT [72]

difference between each of the methods. The benefit to this method over the group theoretical approach is that it allows images to be formed for the cases where more than one component is described by the same irrep. Figure 5.5 shows one of the doublets of the HOMO described by the E irrep when the symmetry is reduced to C_{3v} (i. e. hexagon prone). The comparison given is again with the DFT and experimental images provided in ref. [72].

A complete set of all the images for the LUMO and HOMO of the hexagon prone, pentagon prone, 6-6 bond prone, 5-6 bond prone and atom prone molecule are shown in figures 5.6-5.10, with the images produced using the surface Hamiltonian approach. It is worth noting however, that where images could be constructed using group theoretical techniques, these were produced to verify the accuracy of the method. For each component shown, the current values are chosen to give a realistic comparison with what would be seen during experiment. Images are shown with the components of the HOMO on the top row, and the

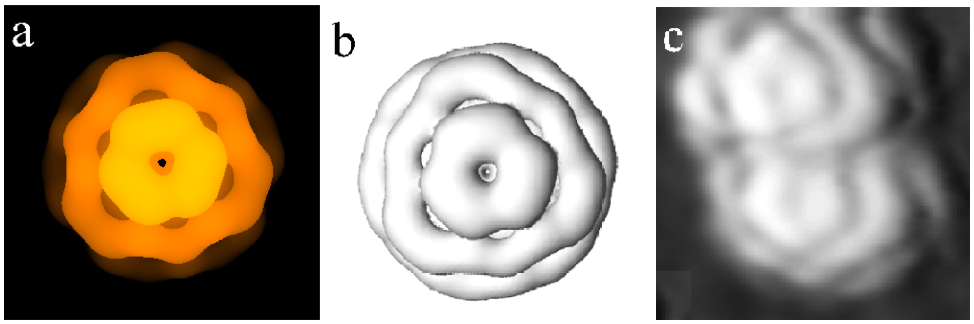

Figure 5.5: Comparison between (a) the theoretical STM image constructed by introducing a surface Hamiltonian (b) the theoretical STM image constructed through DFT [72], and (c) experimentally obtained image of C_{60} on Si(111)-(7x7) [72], for a doublet of the HOMO of a hexagon prone C_{60}.

components of the LUMO on the bottom row.

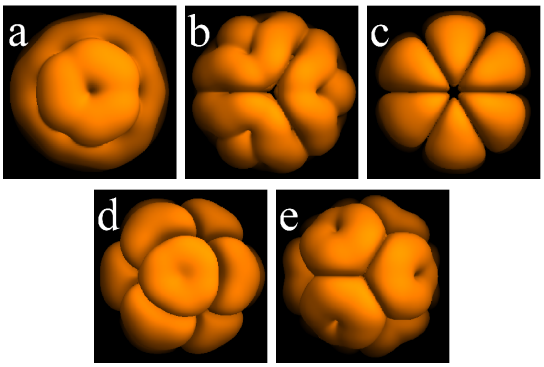

Figure 5.6: Theoretical STM scans of surface-adsorbed C_{60}, produced using HMO theory, with the surface interaction introduced through modification of the Hückel Hamiltonian. The C_{60} is situated with a hexagonal face prone to the surface. (a-c) show the splitting of the HOMO into two degenerate states (a) and (b) and a singlet (c). (d) and (e) show the splitting of the LUMO, with the singlet shown in (d) and the doublet in (e).

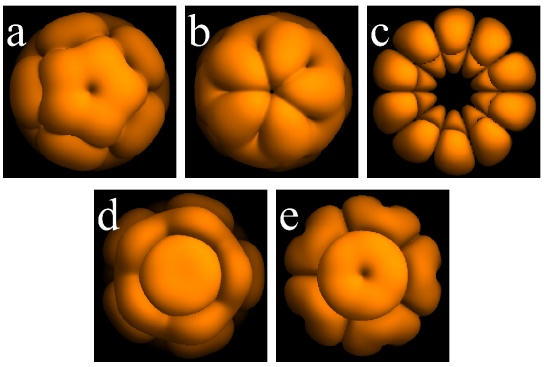

Figure 5.7: Theoretical STM scans of surface-adsorbed C_{60}, produced using HMO theory, with the surface interaction introduced through an appropriate Hamiltonian. The C_{60} is situated with a pentagonal face prone to the surface. (a-c) show the splitting of the HOMO into two degenerate states (a) and (b) and a singlet (c). (d) and (e) show the splitting of the LUMO, with the singlet shown in (d) and the doublet in (e).

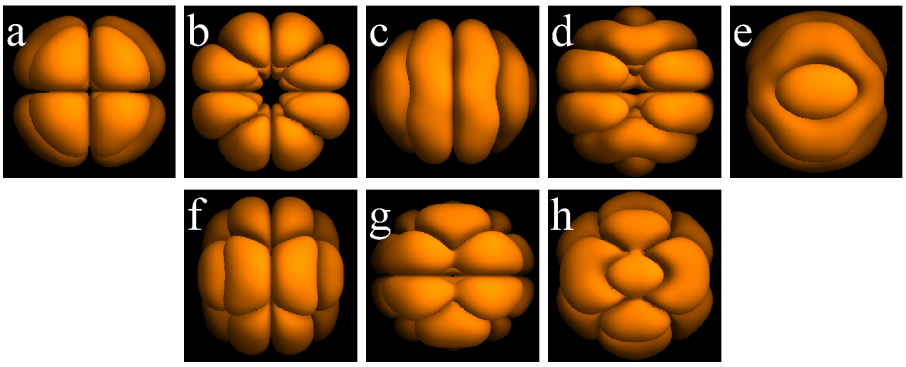

Figure 5.8: Theoretical STM scans of surface-adsorbed C_{60}, produced using HMO theory, with the surface interaction introduced through an appropriate Hamiltonian. The C_{60} is situated with a 6-6 bond prone to the surface. (a-e) show the splitting of the HOMO into five non-degenerate states. (e-g) show the splitting of the LUMO, where three singlets are formed.

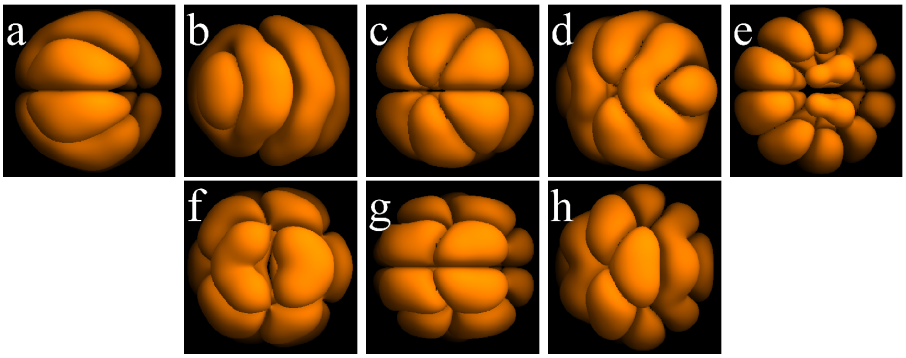

Figure 5.9: Theoretical STM scans of surface-adsorbed C_{60}, produced using HMO theory, with the surface interaction introduced through an appropriate Hamiltonian. The C_{60} is situated with a 5-6 bond prone to the surface. (a-e) show the splitting of the HOMO into five non-degenerate states. (e-g) show the splitting of the LUMO, where three singlets are formed.

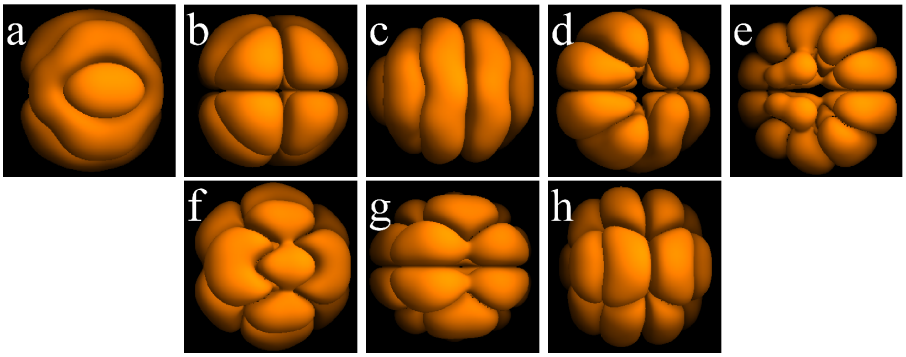

Figure 5.10: Theoretical STM scans of surface-adsorbed C_{60}, produced using HMO theory, with the surface interaction introduced through an appropriate Hamiltonian. The C_{60} is situated with an atom bond prone to the surface. (a-e) show the splitting of the HOMO into five non-degenerate states. (e-g) show the splitting of the LUMO, where three singlets are formed.

5.3 Utilising the 'Derivative Rule'

The theoretical STM images obtained so far have all assumed a simple s type tip state, that allows a simple Tersoff-Hamann relation to be used to obtain the effective current used in constructing the images. While experimentally obtaining such a tip state is desirable, the exact nature of the apex of the probe is often unknown, and can only be implied from the nature of the images obtained. Accurately ascertaining the tip structure from experimental images shall be considered in more detail as this work progresses. However, the start point to looking at this is to see how different forms of atomic orbitals associated with the tip alter the observed STM images.

To model the images obtained from the different states, Chen's derivative rule is utilised (see section 3.1.3, and in particular table 3.1). To see what effect this has on the resultant images, theoretical STM scans can be constructed from the MOs of C_{60}. The images are constructed in an identical fashion as when an s tip state is considered, with the difference that the appropriate derivative of the MO is used instead of the MO explicitly.

Figure 5.11 shows theoretical STM scans of the H_5^D component of the HOMO, as would be obtained for a variety of tip states. It can be seen from this that the image obtained can be greatly affected by the structure of the tip. It should also be noted that this collection of images is far from complete in the possible images that could be obtained from the p and d orbitals. For the s type orbital, which has spherical symmetry, there is only one possible image which can be obtained, as the orbitals is identical in all directions. However, for the p and d type orbitals, where the orbital has different characteristics dependent on it's position in space, the relative orientation of the orbital with respect to the sample is important. As a simple example, if a p orbital is considered, it is clear that the orbital does not necessarily have to point in the x, y or z directions of the scan. It is free to point in any direction, and as such the resultant image would be constructed from a linear combination of the derivatives of the MO with respect to x, y and z. Likewise, for the d orbitals, the orbitals considered merely form a

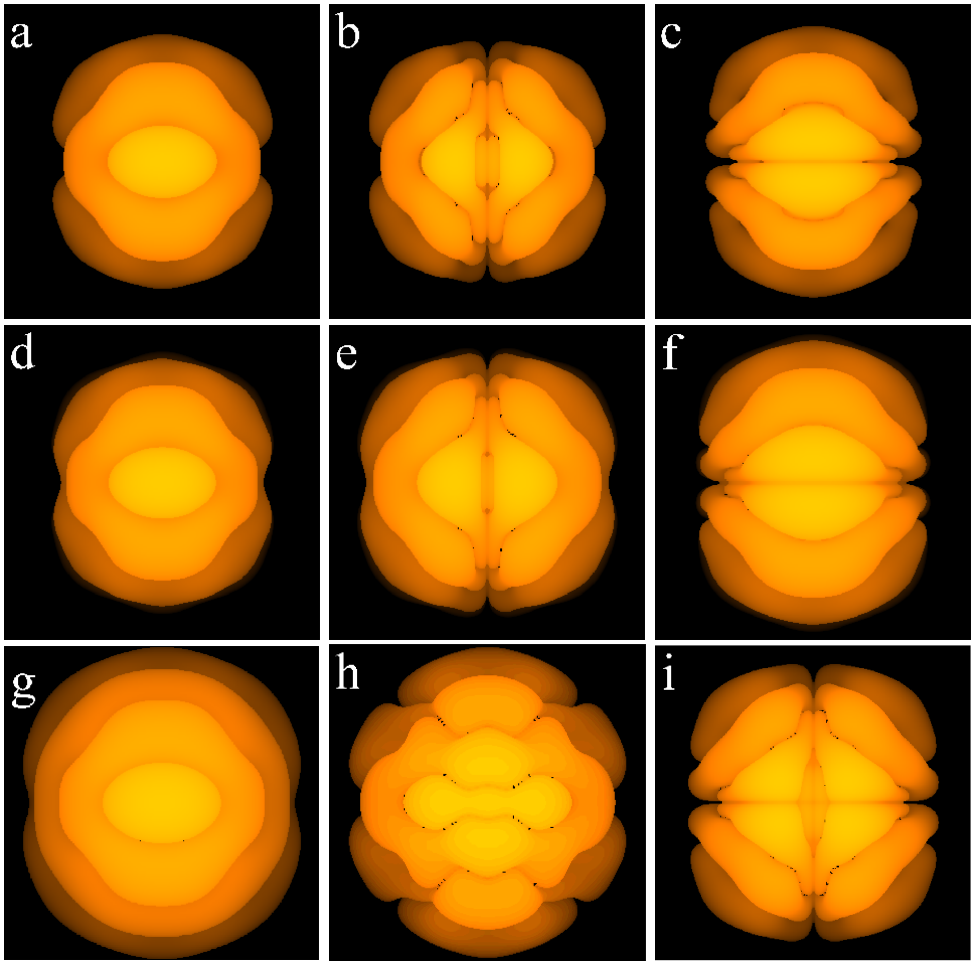

Figure 5.11: Theoretical STM images of the H_5^D MO as imaged through a tip atomic orbital of (a) s-type, (b) p_x-type, (c) p_y-type, (d) p_z-type, (e) d_{xz}-type, (f) d_{yz}-type, (g) $d_{3z^2-r^2}$-type, (h) $d_{x^2-y^2}$-type, and (i) d_{xy}-type.

basis set for a particular orbital that would be observed experimentally. However, the images shown convey some important ideas that allow them to be understood from a simple perspective.

There are a number of similarities within the set of images in figure 5.11. The images constructed from the s (a), p_z (d) and $d_{3z^2-r^2}$ (g) tip states all show similarities, as do the images from the p_x (b) and a d_{xz} (e) tip states, and the p_y (c) and d_{yz} (f) states. The differences and similarities within these comparisons can be explained by considering the form of the orbital making up the tip state.

Figure 5.12 shows the system where a simple p_z orbital is imaged through the same atomic orbitals as used to construct the images in figure 5.11, with the arrows indicating the approximate regions in which the contribution to the tunnelling current from the tip will be greatest. It can be seen that those orbitals

that provide similar images in figure 5.11 have a similarity in their orbital structure where tunnelling occurs. The two lobed structures of the p_x and p_y orbitals matches well with the lower two lobes of the four lobed d_{xz} and the d_{yz} orbitals respectively, and as such give similar images in STM. Likewise, the s, p_z and $d_{3z^2-r^2}$ tip orbitals have a similar contribution in the central region of the STM, although towards the edges of the image, the ring present around the $d_{3z^2-r^2}$ orbital can have a contribution which accounts for the additional feature in this STM image. Differences would still be expected between the images obtained from p and d orbitals, due to the slightly different decay characteristics. For example, comparing the p_x and d_{xz} orbitals, there is slower decay in the z direction of the d orbital due to the additional z contribution, and as such differences would be expected. However, as can been in figure 5.11, it is the general features that remain consistent between the images.

This idea in interpreting the STM images is clearly an approximation to how an image is derived. The tip orbital (or sample MO for that matter) does not have a defined structure as shown in figure 5.12 where the contour value picked to construct the image represents a given probability of the electron distribution, rather than the full distribution itself. However, it does follow that the closest points between the tip and sample contours will have the greatest contribution to the tunnelling current due to the exponential decay of the MOs. This is because an increased distance between points of equal electron density will intuitively result in less tunnelling current being observed, and it is on this premise that this idea is based. This simple idea is useful as a starting point in interpreting STM images, and will be revisited when considering the images obtained when two C_{60} molecules interact.

5.4 Modelling a Functionalised Tip

Using the techniques outlined above it is possible to model the way in which the MOs of a C_{60} molecule split when an external interaction is present. Whereas previously, the interaction with the surface was considered, in this section, the

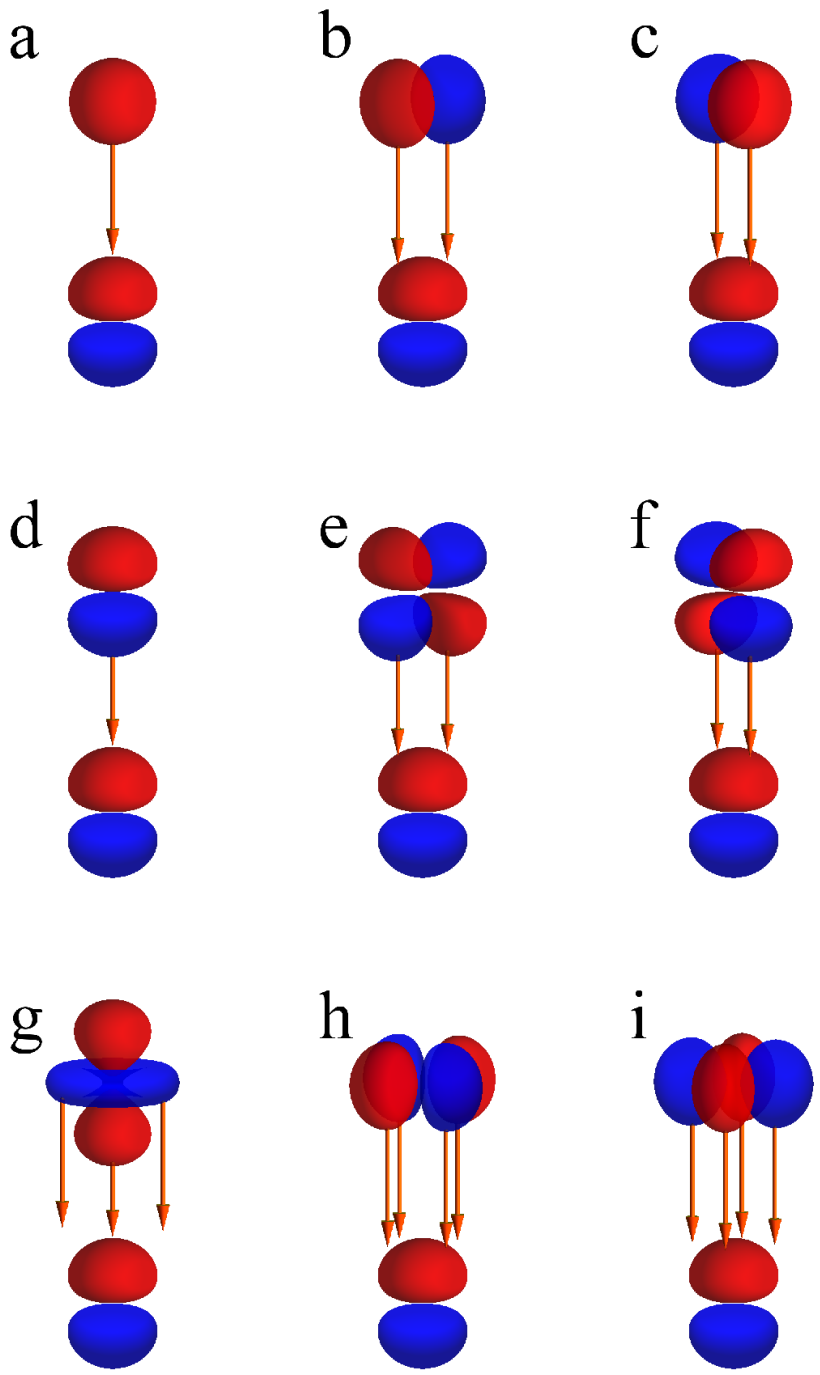

Figure 5.12: Interpretation of the tunnelling between two atomic orbitals, showing a comparison between different tip states. The arrows provide an approximation to the regions of the tip that will provide the most tunnelling current. A p_z orbital is shown to represent the sample interacting with a (a) s-type, (b) p_x-type, (c) p_y-type, (d) p_z-type, (e) d_{xz}-type, (f) d_{yz}-type, (g) $d_{3z^2-r^2}$-type, (h) $d_{x^2-y^2}$-type, and (i) d_{xy}-type, tip orbital.

external interaction under consideration is the bonding mechanism present when a C_{60} molecule is deliberately bound to an STM tip when the probe is functionalised. The system which will be investigated is that where the functionalised tip interacts with the Si(111)-(7x7) surface.

The structure of the Si(111)-(7x7) surface is outlined in section 2.5. The important part of the unit cell that needs to be considered during STM is the twelve adatoms that form the uppermost layer of the structure, as it is these that have the most significant contribution to the tunnelling current. Each of these atoms has an sp^3 dangling bond associated with it that contributes to the STM imaging. Although not listed in table 3.1, the derivative rule can still be used to model the current contribution from an sp^3 hybridised orbital, where it is found that the current differs from that from a p_z orbital by a multiplicative constant only [5]. As HMO theory does not deal in absolute values of the tunnelling current, any multiplicative constant is lost in the proportionality relationship, and as such no error is introduced by modelling the sp^3 orbital as a p_z orbital.

When a surface interaction was considered, the function used to construct the surface Hamiltonian was chosen to decay in the z direction, perpendicular to the surface. To use the same technique to model the bond between the C_{60} and the tip, it is necessary to relax this assumption, and allow the decay to be in some direction away from the z axis of the tip. This is introduced as the nature of the bond between the C_{60} and the probe can not be predicted without knowledge of the atomic structure of the tip. The same idea is used, where r_m, the distance at which the energy reaches a minimum, is defined from a plane perpendicular from the direction of decay, and all distances taken from this plane. However, in practice, the energy lowering is introduced not by rotating the function, but by rotating the molecule (and hence keeping the energy change as a function of z only). The MOs are calculated from this orientation, and then the MOs themselves are rotated to align the molecule in the correct spatial orientation. This is done via a set of five angles, $\lambda^E, \lambda^M, \theta^E, \theta^M$ and κ^M. The superscripts E and M represent the rotations of the molecule for the energy function (E), and the spatial orientation of the molecule (M). These angles act with the three

dimensional counter-clockwise rotation matrices R_x, R_y and R_z to completely define the C_{60} geometry.

With the molecule defined with the x, y and z axes through three 6-6 bonds (with the y axis through a vertical bond), the rotational matrices are applied to the atoms of C_{60} to correctly align it to the desired orientation. For the energy lowering interaction, a rotation in two angles is applied to all the carbon atoms, i.e.:

$$R_x\left(\lambda^E\right).R_y\left(\theta^E\right).C_i, \tag{5.13}$$

where C_i is the position of the ith carbon atom. Note that a rotation in z is not required as this simply rotates the molecule in the same plane that defines the energy function, and so does not alter the energy change in any way. This allows the surface Hamiltonian to be constructed which acts on a new basis defined by the rotated p orbitals. In turn, this allows diagonalisation of the Hamiltonian, and the determination of the MOs, which can then be rotated to the desired alignment through the transformations:

$$(x', y', z') = R_z\left(\kappa^M\right).R_x\left(\lambda^M\right).R_y\left(\theta^M\right).(x, y, z), \tag{5.14}$$

where (x', y', z') represents the transformed coordinates.

If the interaction with a single adatom is considered, the p_z orbital used to model the adatom is symmetric with respect to a rotation in z. Thus, the R_z rotation only has the effect of rotating the obtained image. It is found that as long as the effective current is not chosen to be to small, the large interadatom spacing means that the obtained image can be approximated by considering each adatom independently. This implies that in the region in between adatoms where more than one adatom will contribute, the observed current is small. This means that for investigative purposes, it is possible to just look at the interaction with a single adatom to try to explain a given experimental image, meaning that the R_z rotation is redundant, and κ^M has no bearing on the image obtained. In general, the experimentally derived current appears to relate to large enough values of the effective current for this assumption to hold. However, there are cases when this is not true, as will be considered in chapter 8.

In addition to the four angles used to orient the C_{60} and the MO, the particular MO involved in tunnelling is not known. All of the experimental work shown as a comparison in this section have been taken at a positive sample bias, and as such the tunnelling process is from the occupied states of the tip absorbed molecule to the unoccupied states of the sample. It is therefore the split HOMO that is involved in tunnelling, with the way in which the five-fold degenerate HOMO splits dependant on the molecular orientation considered when introducing the energy lowering function E_s. It is expected that if these states are significantly different in energy, the split levels of the HOMO may be imaged separately, depending on the bias applied. As the energy of these levels can not be predicted by HMO theory, there is no way to know which MOs will be imaged for a particular bias, and as such, simulations need be run with each of the MOs to obtain suitable matches with the experimental data.

For a given set of theoretical parameters, an image is constructed in two different ways. For investigative purposes, the only interaction considered is that with a single p_z orbital used to model the sp^3 orbital of the adatoms. This is simple to construct, as the resultant image is a plot of the derivative of the MO with respect to z (as dictated by the derivative rule). The theoretical raster scan is constructed by fixing the p_z orbital at the origin and scanning over this with the C_{60} molecule in the same way as the theoretical images have been constructed previously. To verify the results found, a theoretical scan is undertaken over the full unit cell. In this case, the centre of the unit cell is situated at the origin, and a p_z orbital assigned to each adatom position, which is then replicated to cover the region of interest. An image is constructed in the same way as normal, with the slight modification that the current contribution from all adatoms within a fixed radius is considered. The size of this radius has an influence on the speed of the calculation, although this is generally less important in these scans, as the images are predominantly being constructed to verify results obtained from the simple scans. For the results here the radius is picked to be the same as the interadatom separation, so that the current from all neighbouring adatoms is always considered.

When analysing experimentally derived data, the theoretical parameters are varied until a comparable image is obtained. The size of the parameter space means that an exhaustive search is not possible, although it is possible to greatly restrict the range of some of the parameters due to the symmetry of the molecule, as the MOs will be identical for equivalent molecular orientations. It is also found that unless E_s decays significantly in either x or y, the theoretical images obtained are comparable within the errors associated with the experimental data. As such, the most crucial parameters in interpreting the experimental images are λ^M and θ^M which define the way the molecule is oriented in space, with little error introduced by considering the energy decaying in the z direction of the scan.

In interpreting experiment, it is important to consider any symmetry that is shown in the image. This often relates to a particular symmetry operation of the molecule that is conserved in the MO, and can indicate the molecular orientation of the tip-adsorbed C_{60}. Figure 5.13 shows three comparisons between experimental and theoretically derived images, all of which show traces of the symmetry that underlines the molecular orientation. In figure 5.13a, the experimental image has (approximately) two perpendicular planes of symmetry and a C_2 rotation, that strongly suggests that the tip-adsorbed molecule is situated with a 6-6 bond in the z direction. The experimental image has one lobe slightly brighter than the other (hence why the symmetry operations are approximate) which can be simply explained through a slight tilt on the molecule. Indeed, when the theoretical images are constructed, the most suitable match is found by introducing a slight tilt away from the 6-6 bond.

In the experimental image shown in figure 5.13b there is a five-fold symmetry that is apparent. The true state of the tip can not be ascertained prior to scanning, and as such this is particularly significant, as C_{60} is one of the few molecules to possess such symmetry, and is therefore a strong indication that the images are indeed obtained through imaging tip-adsorbed C_{60}. When the theoretical scans are constructed, agreement is found with a pentagonal face in the z direction as expected, which also accurately replicates the experimentally observed node in the centre of the image. Finally, in figure 5.13c the experimental image contains

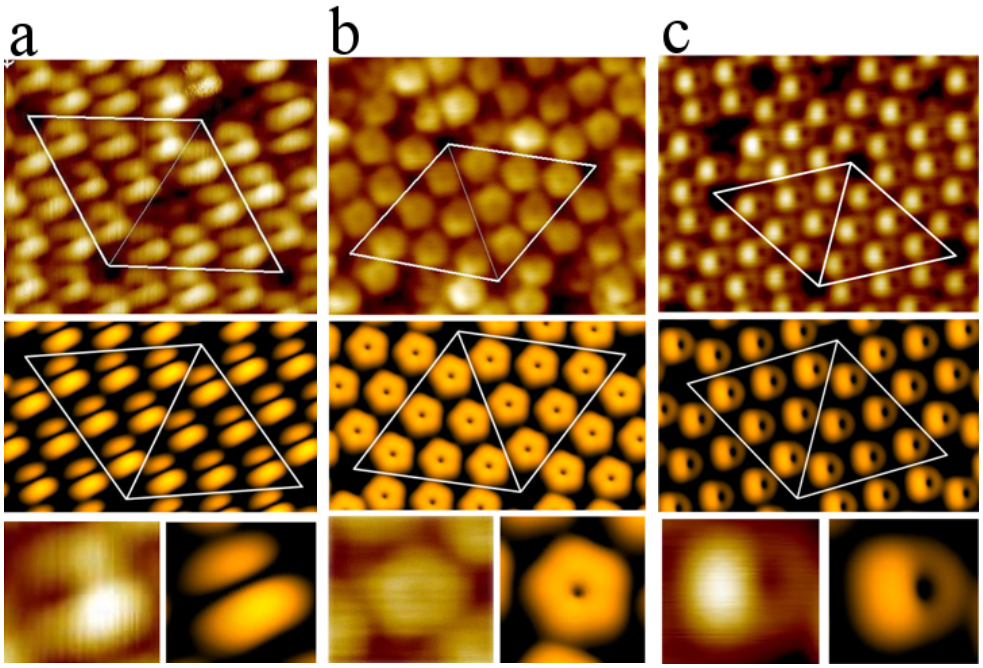

Figure 5.13: Experimental images and the theoretical interpretation for when a C_{60} functionalised tip is scanned over a Si(111)-(7x7) surface. The upper most images show the experimental data, with the image below showing the theoretical interpretation. The image from a single adatom is shown below these with the experimental image to the left of the theory. From left to right, the molecular orientation of the C_{60} is with approximately a $6-6$ bond, pentagonal face, and a $5-6$ bond pointing towards the surface.

only one plane of symmetry, which does not definitively suggest a particular orientation, although does limit the possibilities to any C_s point present on the great circle that passes directly through a 6-6 bond. The most accurate match with experiment is found where the molecule is situated with a 5-6 bond approximately in the z direction. In fact, a slight tilt towards the pentagonal face is suggested, although the lowest point on the molecule is still the 5-6 bond.

The work presented in this chapter has shown how theoretical STM images can be obtained using a LCAO method to obtain expressions for the MOs, with the focus on the C_{60} molecule, where the MOs may be obtained through either EHMO or HMO theory. Two methods of introducing an external interaction are considered for both a surface-adsorbed, and a tip-adsorbed molecule, and the way in which the imaging is affected by different tip structure considered. The work relating to the imaging through a C_{60} functionalised tip has been published in work we have undertaken for *Physical Review Letters* [91]

Chapter 6

C_{60} - C_{60} Interaction (STM)

In the previous chapter theoretical images were obtained to simulate the case where a C_{60} functionalised tip scans over a Si(111)-(7x7) surface. In this section, this idea is extended to analyse the case where the C_{60} molecule on the tip images a second C_{60} molecule adsorbed on to the surface during STM. Investigating this case introduces a whole new range of variables into the model, so the origin of these variables and their physical significance is first discussed. The process through which a successful match between theory and experiment can be obtained is then explained, with emphasis placed on the reverse imaging of the tip state from the surrounding surface, to ascertain the orientation of the tip molecule, and the symmetry of the resultant image to deduce the molecular orientation of the surface molecule. Finally a comparison with the theoretical work undertaken by Rurali *et al.* [62] is made for different bonding sites on the Si(111)-(7x7) surface. A large portion of this work is shown in work we have published in *Physical Review B* [68].

6.1 Constructing the Model

The work undertaken in chapter 5 showed how to model the cases where a C_{60} molecule was adsorbed onto either a surface or the SPM probe. Now, elements of both of these need to be combined to show the form of the STM images when

a tip-adsorbed C_{60} images a surface-adsorbed C_{60}. HMO theory will again be used, and the external interaction will be introduced by constructing a suitable Hamiltonian. Previously, it was assumed that the surface interaction acted only in the direction normal to the surface. While this seems to work accurately for simple surfaces such as Au(111) or Ag(111), a large portion of the experimental comparison will be with molecules adsorbed on Si(111)-(7x7), which has considerably more complicated bonding sites. Where this is the case, this assumption is relaxed, and the energy function allowed to decay along an axis different to the axis perpendicular to the surface.

Figure 6.1 shows a graphical representation of the system under consideration. ζ^T and ζ^S indicate the direction in which the surface interaction is introduced and is altered via two pairs of variables (not shown), λ^{ET} and θ^{ET} for the tip-adsorbed molecule, and λ^{ES} and θ^{ES} for the surface-adsorbed molecule. These angles are used in the same way as indicated in equation (5.13), with a rotation around the y axis applied first, followed by a rotation about x. There are then three variables associated with each molecule that define the molecular orientation of each. These are labelled $\lambda^{MT}, \theta^{MT}$ and κ^{MT} for the tip-adsorbed molecule and $\lambda^{MS}, \theta^{MS}$ and κ^{MS} for the surface-adsorbed molecule. These are applied in the same way as in equation (5.14), with rotations around y, followed by x, followed by z. As was the case when investigating the functionalised tip previously, one of the rotations in z has the effect of rotating the resultant image, and does not change its appearance in any way. As such, for investigative purposes, one of these may be neglected, and where this is the case, it is κ^{MT} associated with the tip molecule that is chosen. However, as will be shown, careful analysis of an experimental image can fix the molecular orientation of the tip-adsorbed molecule, and as such it is not always necessary to neglect it.

As was the case when looking at the interaction between the functionalised tip and the Si(111)-(7x7) surface, all experimental images which are investigated here have been taken at positive sample bias, and as such tunnelling is from the occupied states of the tip, to the unoccupied states of the sample. In relation to the two C_{60} molecules, it is therefore assumed that the image is formed from

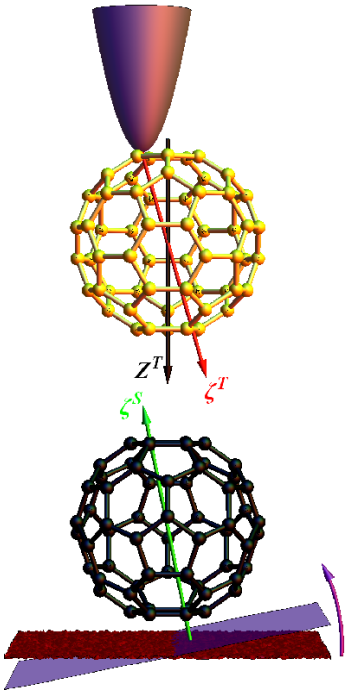

Figure 6.1: Graphical representation of the system under consideration. ζ^T and ζ^S represent the direction in which the external interaction is incorporated for the tip and surface molecules respectively, while Z^T, represents the z direction of the scan.

the convolution of a(the) MO(s) of the tip-adsorbed molecule with a(the) MO(s) of the surface-adsorbed molecule. Thus, in constructing an image for two given orientations, variations are still possible due to the choice of MOs involved in the tunnelling process. The number of possible MOs will be dependent on the molecular orientation as described in tables 5.4-5.7, which in general will be five singlets for the tip-adsorbed molecule, and three singlets for the surface-adsorbed molecule, unless a molecule is situated in a high symmetry orientation, when doublets will be present.

6.1.1 Modelling the Tunnelling Current

In modelling the tunnelling current, Chen's derivative rule may still be utilised. For a functionalised tip where the MOs of the tip-adsorbed molecule may be expressed as a LCAO, the interaction between individual sample and tip orbitals may be treated independently, and as such I' consists of a simple sum over all interacting orbitals. That the expression for I' is separable in this way is due to the derivation of the derivative rule, which has its roots in the evaluation of the

integral associated with Bardeen's matrix element (equation (3.3)). Placing the expression for the MO of the functionalised tip into this integral, and noting that the MO is a linear combination, the integral can be divided into a sum of individual integrals associated with the atomic orbitals that form the MO. As each of these integrals relate to the interaction between a sample and a single atomic orbital, they can be simplified using the derivative rule to give an effective current that is the sum of derivatives of the sample orbital, evaluated at the appropriate atomic centres, i.e.:

$$I'(R_0) = \sum_j c_j d[\chi](r_j)^2, \tag{6.1}$$

where c_j, is the coefficient of the jth atomic orbital defined from the MO and $d[\chi](r_j)$ is the appropriate derivative of the sample MO χ, evaluated at the atomic centre of the jth orbital (r_j). Note that R_0 represents the molecular centre of the functionalised tip, and r_j is the jth atomic centre that is directly determined from R_0.

In the case where HMO theory is used, and the electronic basis is a linear combination of p orbitals, $d[\chi]$ will always relate to the first derivative in the direction in which the p orbital points, defined as i. Thus, for a C_{60} functionalised tip interacting with a sample χ, I' becomes:

$$I'(R_0) = \sum_j^{60} \left(c_j \frac{\partial \chi(r_j)}{\partial i} \right)^2. \tag{6.2}$$

As the sample molecule is also a C_{60} it is computationally beneficial to also express χ as an LCAO, giving I' as the further summation:

$$I'(R_0) = \sum_j^{60} \sum_k^{60} \left(c_j c_k \frac{\partial p_k^S(r_j)}{\partial i} \right)^2, \tag{6.3}$$

where k sums over the sample p^S orbitals. In practice, it is simplest computationally to divide the derivative in the i direction into a linear combination of derivatives in the x, y and z directions. This is valid as the radial p orbital can be equivalently written as a linear combination of p_x, p_y and p_z orbitals, and hence, the summation can be divided still further to give:

$$I'(R_0) = \sum_l^{x,y,z} \sum_j^{60} \sum_k^{60} \left(c_l c_j c_k \frac{\partial p_l^S(r_j)}{\partial i} \right)^2, \tag{6.4}$$

with l summing over the three forms of p orbital, and c_l representing the coefficient of the appropriate p orbital as defined by the linear combination that makes up the radial p orbital.

When constructing a constant current theoretical image, this expression can be solved to give the height, z, that results in a particular value of I'. The size of the summation causes an increase in the computational time at each point in the raster scan, and so to be of use as an investigative tool, the expression requires simplification. Equation (6.4) sums over all 60 of the atomic orbitals of both molecules, which, when divided into individual p_x, p_y and p_z contributions, results in 10800 individual contributions to the effective current. However, a number of these interactions will have negligible contribution to the overall current, due to the increased spatial distance, and hence minimal overlap, of the atomic orbitals at the atomic positions. As such, a large number can be neglected. For investigative purposes, it is possible to eliminate all but the contributions from the nearest six atomic orbitals on each molecule (108 interactions) with only small error. Where necessary these can then be verified by including more interactions, with all the images shown here found from the nearest 10 atomic orbitals (300 interactions). A selection of images were also constructed using the full 10800 interactions to check the validity of this assumption, with it found that these images and those obtained using the nearest 10 orbitals, were indistinguishable.

6.2 Theoretical Images

To aid in the interpretation of the experimental images, it is beneficial to use any reflectional or rotational symmetry the images possess to approximate the molecular orientation of the two C_{60}s and reduce the number of parameters which may be varied. When isolated, C_{60} is described by the highly symmetric icosahedral point group, I_h, although when an external interaction is present, in this case through bonding with the tip or substrate, it has been shown that the molecular distortion that is induced lowers this symmetry. Even so, a number of symmetry operations are expected to be preserved depending on the orientation of the

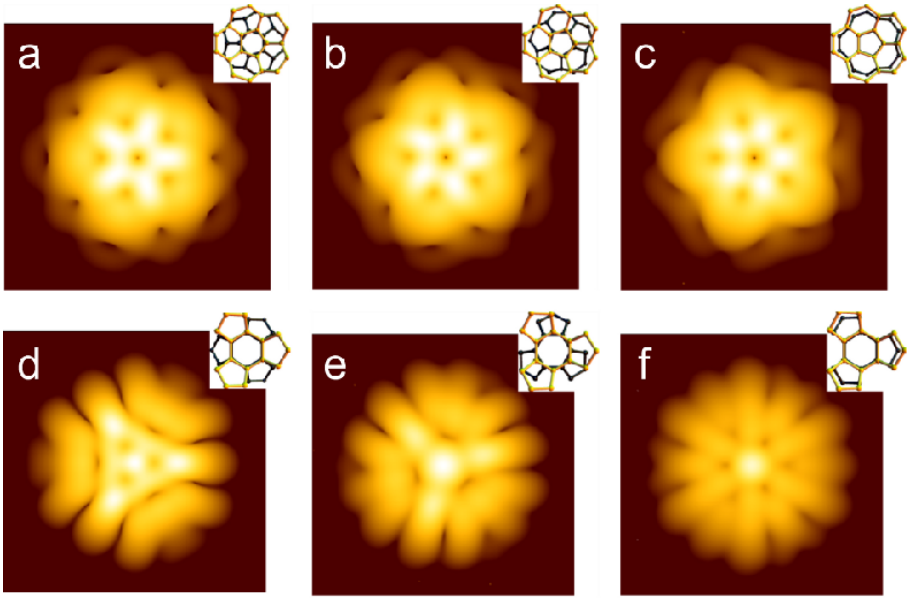

Figure 6.2: (Theoretical STM images for the case where a pentagonal face on each molecule are aligned ($\theta^{MT} = \theta^{MS} = \text{ArcTan}\left[\phi^{-1}\right]$) ((a) $\kappa^{MT} = 0$, (b) $\kappa^{MT} = 2\pi/20$, (c) $\kappa^{MT} = 2\pi/10$), and two hexagonal faces are aligned ($\theta^{MT} = \theta^{MS} = \text{ArcTan}\left[\phi^{2}\right]$) ((d) $\kappa^{MT} = 0$, (e) $\kappa^{MT} = 2\pi/12$, (f) $\kappa^{MT} = 2\pi/6$). The relative orientations of the two molecules are shown inset of each image, with the lighter (yellow online) molecule showing the orientation of the tip-adsorbed molecule, and the black molecule showing the orientation of the surface adsorbed molecule.

molecule.

Figure 6.2 shows possibilities for the STM images obtained for the case where the tip and sample molecules are situated with pentagonal faces aligned with one another (a, b, c), and when the molecules have hexagonal faces aligned (d, e, f). In constructing these images, a generic surface is assumed, with the external interaction acting solely in the z direction. The relative molecular orientations are shown inset of the theoretical images by looking through the bottom half of the tip adsorbed molecule (yellow in figure 6.2) onto the upper half of the surface-adsorbed molecule (black in figure 6.2) at the point where the two molecules are exactly aligned during the scan. From the theoretical images, two key features should be noted which are indicative of the higher symmetry orientations. First, it can be seen in all the images shown, that the relevant rotational symmetry is conserved in the images, i.e. a, b and c have C_5 rotational symmetry, and d, e and f have C_3 rotational symmetry. Second, when the reflections in the z plane are aligned for both molecules (a, c, d, f), this reflection is preserved, and is present in the image obtained.

The results obtained in figure 6.2 are comparable to those obtained by Hauptmann *et al.* [94]. There, the C_{60}-C_{60} interaction was modelled by considering orbitals formed from two-dimensional Gaussians which provided a three-fold symmetric pattern for the electron distribution on each hexagonal face. The electron density associated with the HOMO is known to be localised around the 6-6 bonds, and so the Gaussian functions are chosen to represent a large electron distribution over these bonds. For the LUMO, the electron density is around the 5-6 bonds, so the opposite is used, with the large electron distribution over these bonds. For imaging purposes, only the uppermost face of the C_{60} is considered, with the convolution of the LUMO and HOMO representation taken to construct the final image.

The comparison between the results here and the experimental and theoretical results obtained by Hauptmann *et al.* is shown in figure 6.3, where it can be seen that by considering MOs which encompass more than just the uppermost face, and the split in energy of the MOs due to the external interactions, a theoretical representation which more closely resembles the experimental images is obtained. In particular, for image (i), where the surface molecule is adsorbed with a pentagonal face prone, the local three-fold symmetry at the center of the image is more clearly represented. The experimental image shown in (d) also shows evidence of a slight darkening within the triangular feature, that is also observed in the image produced from the method presented here (j), but not in the Gaussian approximation (g).

In the work by Hauptmann *et al.* [94], the experimental images were of C_{60} monolayers being imaged through a C_{60} functionalised tip. However, often the interaction between the tip-adsorbed C_{60} and a single surface-adsorbed C_{60} will be of greater interest, due to the removal of the intermolecular interactions within the monolayer, which results in data relating more to the independent C_{60}-C_{60} interaction. It is this that is considered in figure 6.4 where unpublished experimental data [50] is shown of a C_{60} functionalised tip, interacting with C_{60} molecules adsorbed on to the Si(111)-(7x7) surface.

Figure 6.4a shows an experimental image where the contrast has been adjusted

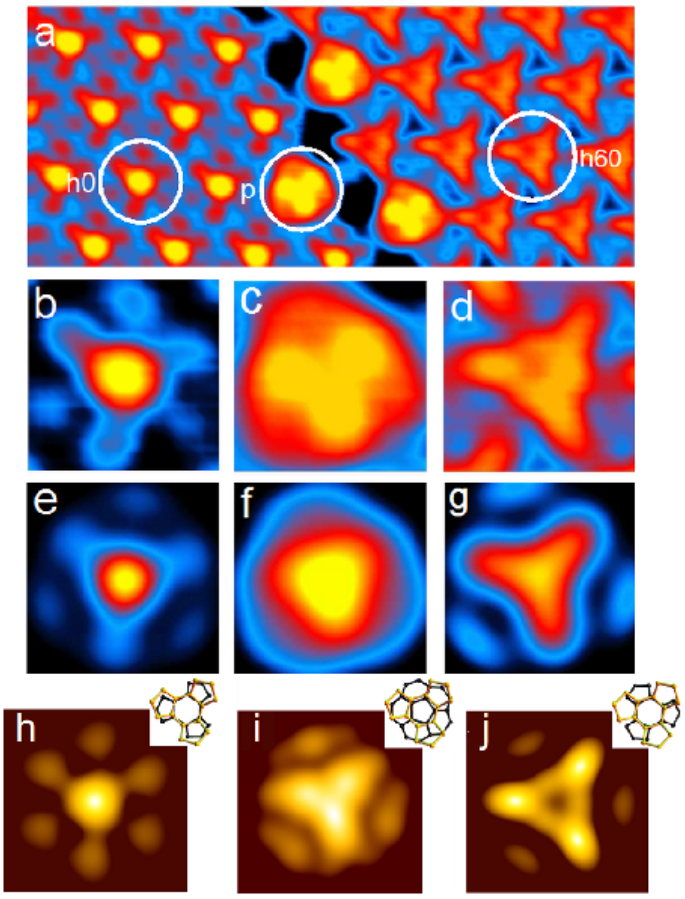

Figure 6.3: Comparison of experimentally and theoretically obtained images (experiment:a-d,theory:e-g), and theoretically obtained images using the method presented here (h-j). The relevant orientations of the two molecules are shown inset of each of the theoretical image obtained from this method (as described in figure 6.2), in close agreement with the orientations postulated by Hauptmann *et al.* [94]. The orientation of the tip-adsorbed molecule in (h-j) is defined by $\theta^{MT} = \mathrm{ArcTan}[\phi^2], \lambda^{MT} = 0$ and $\kappa^{MT} = -0.1$. The surface-adsorbed molecules are defined by: (h), $\theta^{MS} = \mathrm{ArcTan}[\phi^2], \lambda^{MS} = 0, \kappa^{MS} = 0.9$, (i), $\theta^{MS} = \mathrm{ArcTan}[\phi^{-1}], \lambda^{MS} = 0, \kappa^{MS} = 0$, (j), $\theta^{MS} = \mathrm{ArcTan}[\phi^2], \lambda^{MS} = 0, \kappa^{MS} = 0.1$

such that the interactions between the C_{60} functionalised tip and the adatoms of the silicon surface are made clear. The two molecules that will be investigated are highlighted by the black circle and white square. However, the first step in interpreting the data is to elucidate the tip state. Using the same approach as outlined in section 5.4 the orientation of the tip-adsorbed molecule can be found. The experimental image of the silicon unit cell has been magnified and reproduced in figure 6.4b, where it can be seen that the image from each adatom is formed as a two lobed structure. The symmetry of this image suggests that the tip-adsorbed molecule is oriented with a 6-6 bond pointing towards the adatom, but with a slight tilt away from this bond to account for the difference in bright-

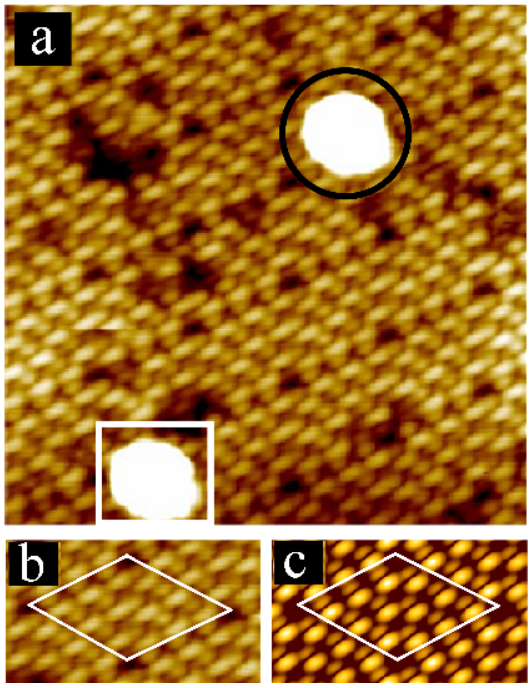

Figure 6.4: Experimental image and theoretical comparison of the interaction between a tip-adsorbed C_{60} and the Si(111)-(7x7) surface. (a) shows the experimental image with the contrast adjusted to highlight the interaction between the tip and the silicon adatoms. Also within this image are two C_{60} molecules indicated by the black circle and the white square. (b) shows a magnified region of the silicon surface with the unit cell outlined in white, whereas (c) shows the theoretical interpretation of this (again with the unit cell outlined in white), where the parameters associated with the molecular orientation are $\theta^{MT} = -0.1$, $\lambda^{MT} = -0.1$ and $\kappa^{MT} = 2.1$. (Experimental scan parameters: $V = 2.4$V, $\langle I_t \rangle = 500$pA, $A_0 = 1.5$nm)

ness of the two lobes. Using this as the start point, the molecular orientation can be found by repeated imaging of the surface with slight alterations to the parameters associated with this orientation. The most accurate representation of this is shown in figure 6.4c, where a theoretical STM scan is shown with the molecular orientation given by the angles $\theta^{MT} = -0.1$, $\lambda^{MT} = -0.1$, and $\kappa^{MT} = 2.1$.

With the orientation of the tip-adsorbed molecule elucidated, it is then simpler to interpret the experimental images relating to the C_{60}-C_{60} interaction on the assumption that the interaction between the two C_{60}s does not alter the position of the tip-adsorbed molecule. While it is a consideration that the interaction between the two could cause some deviation, there is no experimental evidence that a change in tip state is observed when the surface molecule is scanned, as the image formed between the tip and the adatom does not change after scanning a C_{60}. In addition, the theoretical matches provide a good description of the

experimentally derived images (as will be shown), and as such it is deduced that any localized 'wobbling' as the tip passes over the molecule is small.

In interpreting the C_{60}-C_{60} images, the molecule indicated by the black circle in figure 6.4 will be considered first. The theoretical interpretation and the experimental image is shown in figures 6.5a and b. The scaling of the experimental image (b) has been adjusted to best pick out the features of the intermolecular interaction. This experimental image has (approximately) two planes of reflection perpendicular to each other, as well as an approximate C_2 rotation, indicating that both molecules must be approximately aligned with a 6-6 bond facing each other, either with the bonds aligned, or perpendicular to each other. This is consistent with the orientation elucidated for the tip-adsorbed molecule, and so this information can be used as a starting point to ascertain the molecular orientation of the sample adsorbed molecule. Setting the sample-adsorbed molecule's molecular orientation such that a 6-6 bond is perpendicular to the surface, and then allowing the parameters to vary, results in the theoretical image shown in figure 6.5a as the most suitable comparison with experiment, where it can be seen good agreement is found between the two. The molecular orientation in this case is defined by the angles $\theta^{MS} = 0$, $\lambda^{MS} = 0$ and $\kappa^{MS} = 0.6$. A slight difference exists in the theoretical comparison when compared to the experiment in the upper right region of the image, where an additional feature is observed experimentally. This could be explained by slight deviations of the tip orientations during scanning, an increased interaction with the underlying substrate at the outermost edge of the imaging, or possibly due to contributions from other MOs lying close in energy to that considered. However, the crucial features in the central region of the image are well produced from the theoretical interpretation.

With a suitable theoretical interpretation of the experimental image found, the comparative orientations can be shown, and it is this that is depicted in figure 6.5c. In this image, the tip-adsorbed molecule is represented in yellow, and the sample-adsorbed molecule in black. The molecular positions are chosen such that the two molecules have their z axes directly aligned, with the viewpoint picked so that the image looks from the molecular centre of the tip-

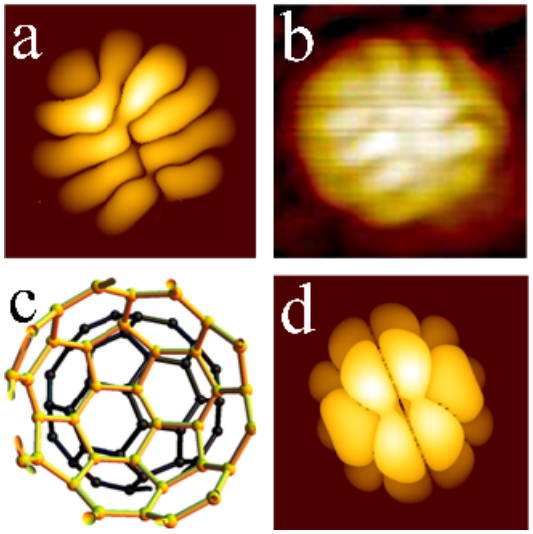

Figure 6.5: Comparison of theoretical and experimental STM images for the C_{60}-C_{60} interaction. The theoretical image is shown in (a) with molecular orientation defined by the rotations $\theta^{MS} = 0$, $\lambda^{MS} = 0$ and $\kappa^{MS} = 0.6$. (b) shows the experimental image, with the contrast adjusted to pick out the intermolecular features. (c) shows the relative orientations of the two molecules, with the tip-adsorbed molecule shown in yellow, and the sample-adsorbed molecule in black, while (d) shows a theoretical image of the sample MO involved in the tunnelling process as if imaged through an s-type orbital.

adsorbed molecule, and through this molecule at the sample-adsorbed molecule. As was predicted, the relative orientations are with the two 6-6 bonds very closely aligned to one another. The bonds are roughly parallel to each other, as a suitable theoretical image could not be obtained by considering the two perpendicular to one another. Using this orientation for the surface-adsorbed molecule, figure 6.5d shows a theoretical image of what *would* be seen if the sample molecule was to be imaged through an s-type tip state, at the appropriate bias to pick out the MO contributing to the C_{60}-C_{60} interaction.

In the case shown in figure 6.5, the symmetry of the image could be used to elucidate the approximate molecular orientations of the two molecules as a starting point for the analysis. However, in general, this will not be the case for most experimentally observed images. Even so, the method can still be used in these more complicated cases, as shown for the second molecule on the experimental image, depicted by the white circle in figure 6.4a, where a more 'trial and error' style approach needs to be taken. Here, the tip-adsorbed molecule will be oriented in the same way as for the previous match, and as such it is only the orientation of the surface molecule, and the MOs associated with it, that need to

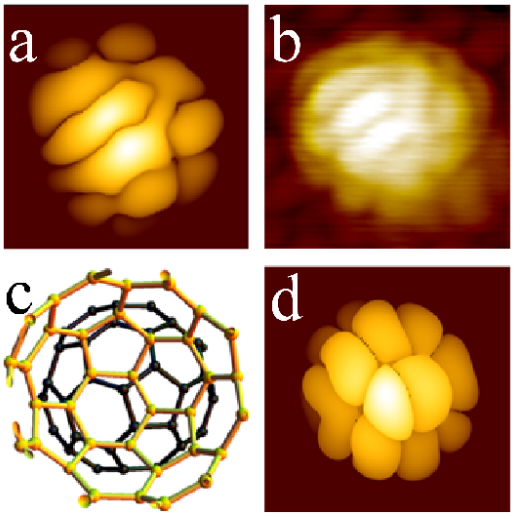

Figure 6.6: Comparison of theoretical and experimental STM images for the C_{60}-C_{60} interaction. The theoretical image is shown in (a) with molecular orientation defined by the rotations $\theta^{MS} = 0.65$, $\lambda^{MS} = -0.2$ and $\kappa^{MS} = -0.7$. (b) shows the experimental image, with the contrast adjusted to pick out the intermolecular features. (c) shows the relative orientations of the two molecules, with the tip-adsorbed molecule shown in yellow, and the sample-adsorbed molecule in black, while (d) shows a theoretical image of the sample MO involved in the tunnelling process as if imaged through an s-type orbital.

be varied to obtain the match. In this case, the process used to obtain the molecular orientation was to create an initial library of images for the interaction with each MO of the surface-adsorbed molecule, with the molecule oriented with either a hexagon, pentagon, 5-6 bond, or atom prone to the surface. In this case the surface molecule is assumed to not be oriented with a 6-6 bond normal to the surface, as this would result in both molecules possessing a C_2 rotation which, as discussed, would be seen in the experimental image. Once these images are produced it is straightforward to analyse the data to find an image that approximately matches the experimental work, and the various parameters can then be altered until the most suitable match is found. Using this process, a good match with experiment is again found, and it this that is shown in figure 6.6.

In figure 6.6a the theoretical STM image is shown as an interpretation of the experimental image shown in (b). Again, the scaling of the experimental image has been adjusted to pick out the intermolecular contrast within the image. The comparison between the experimental and theoretical images is again good, with the surface-adsorbed molecule this time situated with a 5-6 bond, approximately oriented in the z direction (the angles used to obtain this orientation are $\theta^{MS} =$

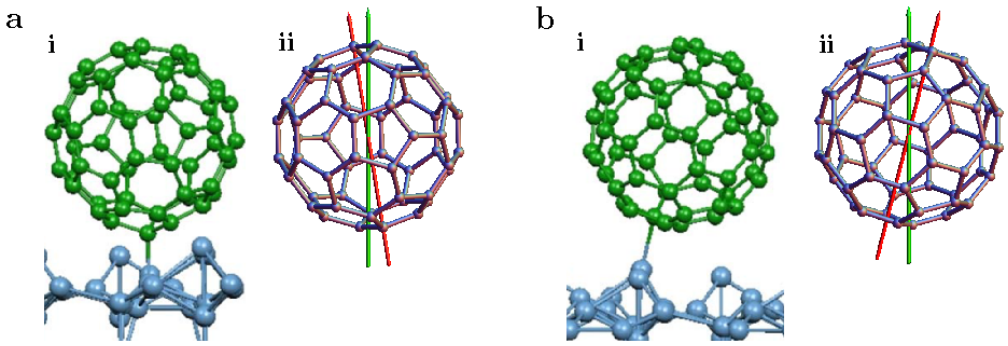

Figure 6.7: Comparison of the molecular orientations found using the method presented here, and that obtained using a tight binding technique by Rurali *et al.*. [62] (a) (i) molecular orientation of an R_f binding site as defined by Rurali *et al.*, (ii) the orientation of the surface adsorbed molecule from figure 6.5 ($\theta^{ES} = 0$, $\lambda^{ES} = -0.05$). In (ii) the green arrow points normal to the surface, and the red arrow indicates the direction along which the energy function decays. (b) (i) Molecular orientation for an M_u binding site, and (ii) for the molecular orientations as found in figure 6.6 ($\theta^{ES} = 0$, $\lambda^{ES} = 0.65$).

0.65, $\lambda^{MS} = -0.2$ and $\kappa^{MS} = -0.7$). The relative molecular orientations is shown in figure 6.6c, where it can be seen that the tip-adsorbed molecule is oriented identically to previously (as expected), and the surface molecule tilted slightly away from the single bond towards the atomic position. This orientation would suggest that a reflectional plane may exist in the observed image, as the 6-6 bond of the tip-adsorbed molecule is close to the alignment of the reflectional plane passing perpendicular to the 5-6 bond of the sample molecule. However, the slight deviations in the orientations from this, both with a tilt towards the atom in the surface-adsorbed molecule, and with respect to a rotation around the z axis, mean that this symmetry is lost.

For these two matches, the orientations of the surface adsorbed molecules can be compared with the theoretical results obtained by Rurali *et al.*, [62] where, through the utilisation of a tight-binding technique to obtain the most energetically favourable bonding sites, seven stable configurations were postulated for different sites on the Si(111)-(7x7) surface. One of these is the corner hole (CH) orientation, where the molecule is situated in the gap between six adatoms of the surface structure. The remaining six orientations are all with the C_{60} situated within a triangle defined by three adatoms, with three different sites (C, M and R) providing two possibilities each dependent on whether these sites are on the faulted or unfaulted section of the Si(111)-(7x7) unit cell, represented by the

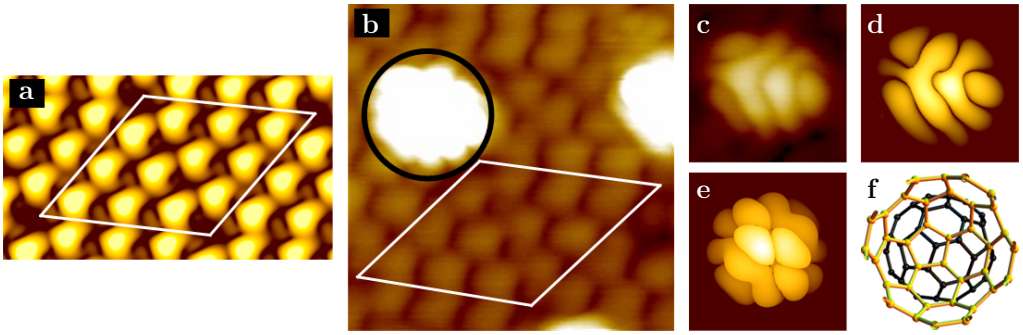

Figure 6.8: Comparison between experimentally and theoretically obtained STM images. (a) Theoretical simulation for the C_{60}-adatom interaction as a comparison to the experimental image (b) (Si(111)-(7x7) unit cell highlighted in white) ($\theta^{MT} = 0.75$, $\lambda^{MT} = 0$, $\kappa^{MT} = 2.95$). (c) Experimental image of the circled molecule, and (d) the theoretical comparison. (e) The sample-adsorbed molecules MO as imaged through an s-type tip,(f) the relative orientation of the two C_{60}s depicted in the same way as in figure 6.2, ($\theta^{MS} = 0.65$, $\lambda^{MS} = -0.2$, $\kappa^{MS} = -1.05$). (Experimental scan parameters: $V = 2.3$V, $\langle I_t \rangle = 300$pA, $A_0 = 1.5$nm)

subscripts f or u respectively (full details of these sites are given in Rurali *et al.* [62]). Analysis of experimental results by Du *et al.* [63] indicate the presence of five of these orientations, namely the CH,M_u,M_f,C_f and C_u bonding sites.

A comparison between the bonding sites proposed by Rurali *et al.* [62] and the results found here is shown in figure 6.7, where excellent agreement is found with two of these bonding sites (the R_f and M_u sites). Figure 6.7a corresponds to the orientation deduced in figure 6.5, which shows good agreement with the R_f bonding site, and figure 6.7b shows the molecular orientation from the match in figure 6.6, in agreement with the M_u bonding site. In both cases, the orientation deduced by Rurali *et al.* is shown in (i), and the orientation found from the method shown here in (ii). The agreement is particularly close for the M_u bonding site in figure 6.7b, where the axis depicting the energy reducing function, aligns closely with the Si-C bond.

The results obtained here correlate well with some of the orientations postulated in Rurali *et al.* [62] and as such, to further reduce the complexity of this particular system it can be beneficial to use these orientations as starting points for the molecular orientations of the surface adsorbed molecules. One such case is shown in figure 6.8, where the surface adsorbed molecule is in the M_u configuration. Again, the interaction with the tip-adsorbed molecule and the adatoms on the surface can be used to elucidate the tip configuration. In this case the

interaction with the adatom provides the match shown in figure 6.8a where the molecule is situated with a 5-6 bond approximately facing the surface. Taking this orientation and the MO function, along with the orientation predicted for the surface molecule for the M_u bonding site, the result shown in figure 6.8d is obtained, where again excellent agreement is found with the experimental data (shown in figure 6.8c).

In making these comparisons it is important to consider the errors associated with the orientational parameters of the molecules. It is difficult to quantify this error, as a suitable match is obtained by eye as opposed to a specific quantitative process. Also, the different parameters have a varying effect on the image, and as such the error of each is different. Even so, it is possible to gain some insight into how the parameters affect the image by allowing each parameter to vary from a given orientation. In addition to this, the possibility of obtaining a false agreement with experiment appears to be very small, although the parameter space is obviously too large to consider every possibility. However, from the simulations undertaken the images appear to be, in the vast majority of cases, unique.

In figure 6.9, images are constructed where both C_{60} molecules are situated with a 6-6 bond aligned with one another, such that in the central image, (e), all of the orientational rotations are equal to zero. In the surrounding images, the orientation of the sample molecule is altered by changing the values of θ^{MT} and λ^{MT}, to observe the effect on the image, where the range of these angles plotted in figure 6.9 is $\pm 5^{\circ}$ for both θ^{MT} and λ^{MT}. It can be seen from this that differences exist in the images. Even though the general form of the image is similar in each case (as would be expected for a small rotation) within the central region, the brightness of the surrounding lobes changes depending on the rotation. This difference in intensity would be expected to be observable in STM.

The images in figure 6.9 show how both θ^{MT} and λ^{MT} affect the resultant images. However, it is also important to consider the relative orientation with respect to a rotation around the z axis, as given by the angle κ^{MS}. Note κ^{MT} will have the opposite effect as κ^{MS}, although this is has been fixed by comparison

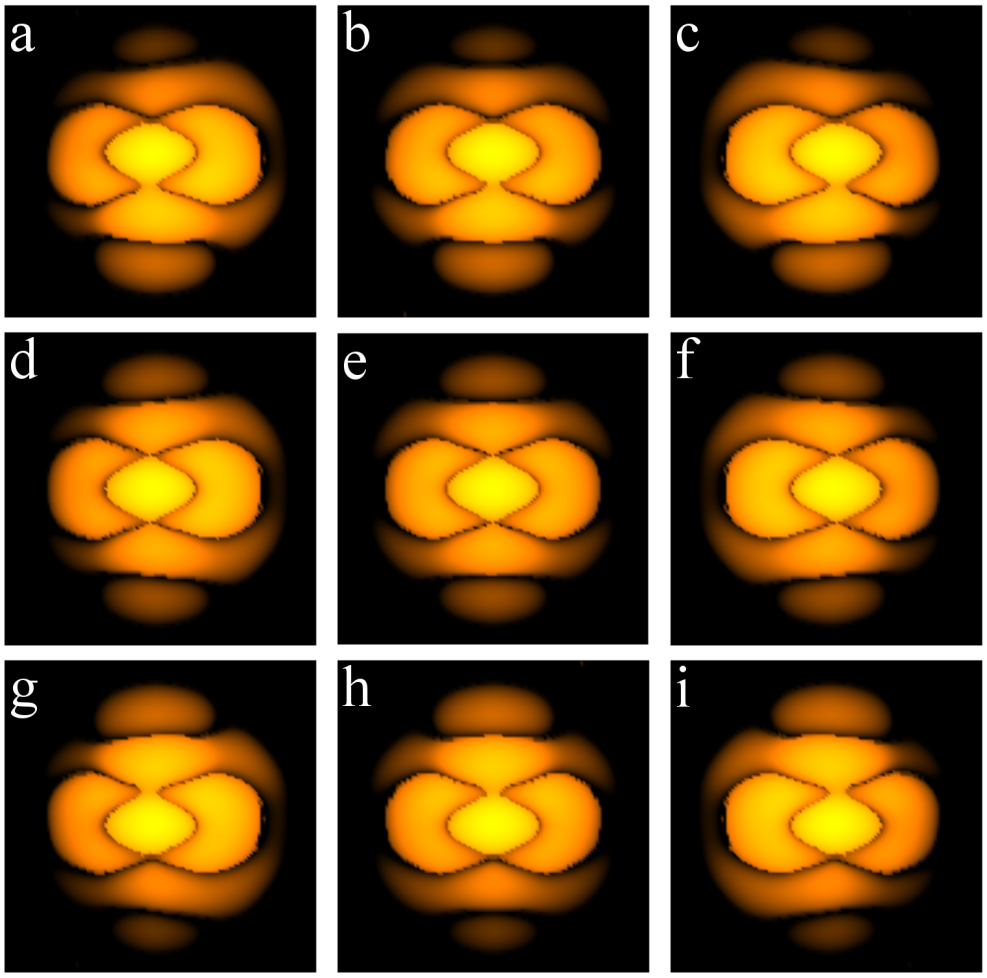

Figure 6.9: Theoretical STM images of a surface-adsorbed C_{60} imaged through a C_{60} functionalised tip, showing the change in the image due to a rotation of the tip molecule. All rotations are equal to zero with the exception of θ^{MT} and λ^{MT} which take the values (a) $\theta^{MT} = -5°$, $\lambda^{MT} = -5°$ (b) $\theta^{MT} = -5°$, $\lambda^{MT} = 0°$ (c) $\theta^{MT} = -5°$, $\lambda^{MT} = 5°$ (d) $\theta^{MT} = 0°$, $\lambda^{MT} = -5°$ (e) $\theta^{MT} = 0°$, $\lambda^{MT} = 0°$ (f) $\theta^{MT} = 0°$, $\lambda^{MT} = 5°$ (g) $\theta^{MT} = 5°$, $\lambda^{MT} = -5°$ (h) $\theta^{MT} = 5°$, $\lambda^{MT} = 0°$ (i) $\theta^{MT} = 5°$, $\lambda^{MT} = 5°$

with the image formed due to the interaction between the adatom and the functionalised tip, and so κ^{MS} is altered here. Figure 6.10 shows three images for this case where all angles are set equal to zero, except for κ^{MS} which takes values of $-5°$ (a), 0 (b), and $+5°$ (c). Again, it can be seen that differences are observed in the imaging, although in this case, the alteration to the image is less significant than for when θ^{MT} and λ^{MT} were altered in figure 6.9.

The angles used to represent the rotation of the axis along which the energy function decays is much less simple to investigate, as the image does not change in a simple way as any of θ^{ET}, θ^{ES}, λ^{ET} or λ^{ES} change. That is to say that there are regions within the parameter space were a set deviation will have a

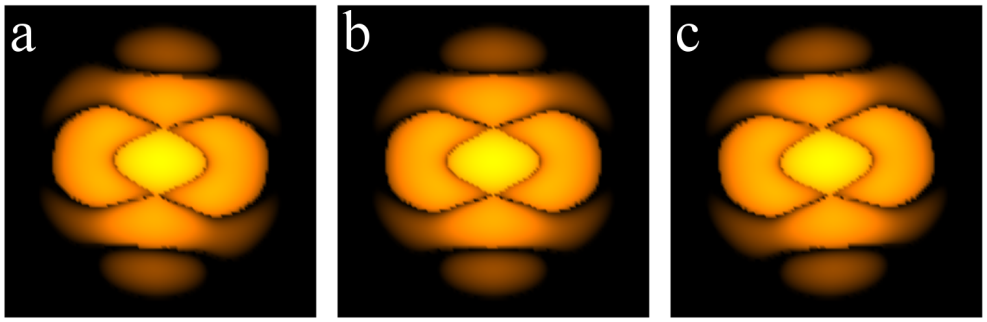

Figure 6.10: Theoretical STM images of a surface-adsorbed C_{60} imaged through a C_{60} functionalised tip, showing the change in the image due to a rotation of the tip molecule. All rotations are equal to zero with the exception of κ^{MS}, which takes values of (a) $-5°$, (b) $0°$ and (c) $5°$

great effect on the image, and regions within the space where the difference will be very small. In actual fact, it is found that this is also true for the angles associated with the molecular orientation considered in figure 6.9, although to a much less extent. As such, the error ideally needs to be ascertained separately for each individual case. Simulations undertaken for the experimental comparisons shown in this chapter, indicate that the orientations are accurate to within around $\pm 5°$ in any direction. However, it is also worth noting that the assignment of this error is somewhat subjective, due to the images being analysed by eye. Even so, this error of around $\pm 5°$ seems suitable as a guide.

A large portion of the work shown in this chapter has been published in *Physical Review B* [68]. Using the techniques shown, it is possible to ascertain information about the tip state and the sample from a single STM image. The system considered here has been with a C_{60} functionalised tip interacting with a surface-adsorbed C_{60}. However, the method is equally applicable to other systems containing molecules that can have their MOs written as a LCAO. This idea will be revisited in a different context in chapter 10.

Chapter 7

AFM of C_{60}

Thus far, a method has been presented that allows the experimentally observed STM images relating to various systems of C_{60} to be interpreted using simple theoretical techniques. In this section, these techniques will be extended to investigate the images obtained during AFM, with particular emphasis placed on imaging during the repulsive regime. Theoretical images will be constructed firstly, for the simple case where a C_{60} on a surface is imaged through a 1s atomic orbital, before the effects of altering this tip state to a variety of atomic forms are investigated. The C_{60}-C_{60} interaction is then investigated looking only at the repulsive interaction, before the attractive interaction is introduced for all the images considered.

7.1 The Force from Two Atomic Orbitals

As described in section 3.2, the force observed during AFM can have its basis in either the attractive regime, due to the vdW interaction, or the repulsive regime, due to the force bought about through the Pauli repulsion when the tip and sample are bought within close proximity. Gross and co-workers showed in a series of papers [7, 30, 95] that to obtain the highest resolution during AFM, it is necessary to image within the repulsive regime, and so it is this interaction that will be given the most consideration.

The mathematics behind the theoretical technique used to model this is also outlined in section 3.2, so will not be repeated here. However in summary, if the wavefunctions of both the tip and sample are known, the force observed due to the Pauli exclusion can be calculated by first, fixing one of the wavefunctions, and then orthogonalising the second wavefunction. The difference in kinetic energy between the orthogonalised and unorthogonalised states can then be utilised to calculate the potential energy change, which can then be used to find either the force or the frequency shift observed experimentally.

To calculate the orthogonalised state, equation (3.15) is used:

$$|\Psi(2)'\rangle = \frac{|\Psi(2)\rangle - \langle\Psi(1)|\Psi(2)\rangle\,|\Psi(1)\rangle}{\sqrt{1 - |\,\langle\Psi(1)|\Psi(2)\rangle\,|^2}}, \tag{7.1}$$

while equation (3.17) is used to determine the change in kinetic energy:

$$\Delta E_{\text{kin}} = \langle\Psi(2)'|\hat{T}|\Psi(2)'\rangle - \langle\Psi(2)|\hat{T}|\Psi(2)\rangle\,. \tag{7.2}$$

Here, $\Psi(2)$ defines the tip wavefunction which is a function of the tip position (X, Y, Z), although for clarity this is not explicitly indicated within the equations at this point. To understand the computational process, it is useful to expand the kinetic energy change in terms of the original functions $\Psi(1)$ and $\Psi(2)$. Noticing that $\langle\Psi(1)|\Psi(2)\rangle = S_{12}$, the overlap between the states, we can first define:

$$\begin{aligned} \eta(1) &= -\frac{S_{12}}{\sqrt{1 - |S_{12}|^2}} \\ \eta(2) &= \frac{1}{\sqrt{1 - |S_{12}|^2}}, \end{aligned} \tag{7.3}$$

which allows equation (7.2) to be expanded to give:

$$\begin{aligned} \Delta E_{\text{kin}} &= \langle\eta(2)\Psi(2) + \eta(1)\Psi(1)|\hat{T}|\eta(2)\Psi(2) + \eta(1)\Psi(1)\rangle - \langle\Psi(2)|\hat{T}|\Psi(2)\rangle \\ &= \eta(1)^2\,\langle\Psi(1)|\hat{T}|\Psi(1)\rangle + \eta(1)\eta(2)\left(\langle\Psi(1)|\hat{T}|\Psi(2)\rangle + \langle\Psi(2)|\hat{T}|\Psi(1)\rangle\right) \\ &\quad + \left(\eta(2)^2 - 1\right)\langle\Psi(2)|\hat{T}|\Psi(2)\rangle\,. \end{aligned} \tag{7.4}$$

For the systems considered here, all of the integrals within equation (7.4) can be calculated analytically either through the use of GTOs, or using STOs alongside the expressions in appendix A. Thus, for a given tip position, the kinetic energy

change can be easily found. However, to construct an image, it is the interaction energy that needs to be considered which is related to ΔE_{kin} through the improper integral:

$$\Delta E_{\text{int}}(X,Y,Z) = \frac{1}{Z}\lim_{\gamma\to\infty}\int_{Z}^{\gamma}\Delta E_{\text{kin}}(X,Y,Z')dZ', \tag{7.5}$$

where the dependence on the tip position is shown through (X,Y,Z), and Z' integrates over the space between the tip-sample separation and the case where the tip is infinitely far away.

Calculating the integral in equation (7.5) would slow down any computational process to the point where it is no longer suitable for investigative work. However, progress can be made by instead calculating the force, by taking the negative of the first derivative of $\Delta E_{\text{int}}(X,Y,Z)$ with respect to the tip position Z, giving:

$$\begin{aligned} F(X,Y,Z) &= -\frac{\partial}{\partial Z}\Delta E_{\text{int}}(X,Y,Z) \\ &= -\frac{\partial}{\partial Z}\left(\frac{1}{Z}\lim_{\gamma\to\infty}\int_{Z}^{\gamma}\Delta E_{\text{kin}}(X,Y,Z')dZ'\right) \\ &= -\left(\frac{1}{Z}\frac{\partial}{\partial Z}\lim_{\gamma\to\infty}\int_{Z}^{\gamma}\Delta E_{\text{kin}}(X,Y,Z')dZ' \right. \\ &\qquad \left. -\frac{1}{Z^2}\lim_{\gamma\to\infty}\int_{Z}^{\gamma}\Delta E_{\text{kin}}(X,Y,Z')dZ'\right). \end{aligned} \tag{7.6}$$

By expanding the indefinite integral, the remaining derivative within equation (7.6) can be derived. At the upper bound, as $\gamma\to\infty$ the integral will evaluate to a numerical value, and will not be a function of Z. Hence, this derivative will be zero. At the lower bound, the integral is being taken with respect to the tip height, and evaluated at the tip position Z. Thus, finding its derivative with respect to Z will simply return the initial function. With this in mind, equation (7.6) can be written as:

$$\begin{aligned} F(X,Y,Z) &= -\left(-\left(\frac{1}{Z}\Delta E_{\text{kin}}(X,Y,Z)\right)-\frac{1}{Z^2}\lim_{\gamma\to\infty}\int_{Z}^{\gamma}\Delta E_{\text{kin}}(X,Y,Z')dZ'\right) \\ &= \frac{1}{Z}\Delta E_{\text{kin}}(X,Y,Z)+\frac{1}{Z^2}\lim_{\gamma\to\infty}\int_{Z}^{\gamma}\Delta E_{\text{kin}}(X,Y,Z')dZ'. \end{aligned} \tag{7.7}$$

Calculating the force from this expression still requires the evaluation of the integral present in equation (7.5). In general, the expressions which will be encountered are too complicated to obtain analytical solutions for the integral. This

is primarily due to the $\frac{1}{\sqrt{1-S_{1,2}^2}}$ term which cannot be subdivided easily into a series of sums. One approach to obtaining a solution is to use a binomial expansion on this term, and this, alongside the use of GTOs, allows an analytical form to be obtained. However, the time taken to both determine the form, and extract the value of the function for given parameters, renders this of little use, even for the simple case of two interacting s-type orbitals.

Progress can be made in obtaining a value for the force, by using GTOs, and obtaining solutions to the integral numerically (here a Monte-Carlo technique is used alongside the STO-6G Gaussian basis set). Figure 7.1 shows two sets of constant height plots where the two terms within equation (7.7) have been calculated and plotted separately, alongside the full force function. The two cases under consideration are where two p_z orbitals interact, and where a p_y tip state interacts with a p_x sample state, with the tip height taken to be 4 Bohrs. It can be seen from this, that all the images for the same interaction are visually the same (in fact the $\frac{1}{Z}\Delta E_{\text{kin}}(X,Y,Z)$ term has a greater contribution to $F(X,Y,Z)$ than the $\frac{1}{Z^2}\lim_{\gamma\to\infty}\int_Z^\gamma \Delta E_{\text{kin}}(X,Y,Z')dZ'$ term in this case). The same result is found for the interaction between all combinations of the $1s, 2s$ and $2p$ orbitals, and for varying tip heights between 1 and 8 Bohrs.

Considering the results shown in figure 7.1, it is possible to considerably simplify equation (7.7). It has been shown that qualitatively there is very little difference between the images produced from the $\frac{1}{Z}\Delta E_{\text{kin}}(X,Y,Z)$ term and the $\frac{1}{Z^2}\lim_{\gamma\to\infty}\int_Z^\gamma \Delta E_{\text{kin}}(X,Y,Z')dZ'$ term. As such, the term containing the integral can be approximated as some multiple of the kinetic energy change, i.e.:

$$\frac{1}{Z^2}\lim_{\gamma\to\infty}\int_Z^\gamma \Delta E_{\text{kin}}(X,Y,Z')dZ' \approx k\frac{1}{Z}\Delta E_{\text{kin}}(X,Y,Z), \tag{7.8}$$

where k is a multiplicative constant. Equation (7.7) then simplifies to:

$$\begin{aligned} F(X,Y,Z) &\approx \frac{1}{Z}\Delta E_{\text{kin}}(X,Y,Z) + k\frac{1}{Z}\Delta E_{\text{kin}}(X,Y,Z) \\ &\approx \frac{1}{Z}\left(1+k\right)\Delta E_{\text{kin}}(X,Y,Z), \end{aligned} \tag{7.9}$$

resulting in an expression that directly relates the force to the change in kinetic energy. Furthermore, if a constant height scan is considered, Z will be a constant.

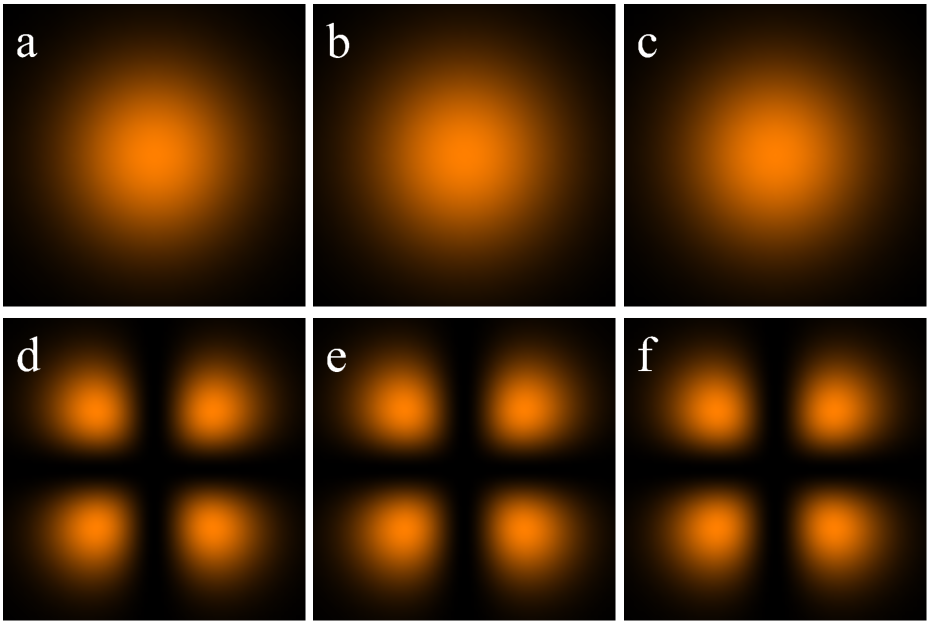

Figure 7.1: Plots showing the similarity of the interaction and kinetic energy changes as a function of the X and Y scan directions, for when two p_z orbitals interact and when a p_x and a p_y orbital interact. The figures show, (a-c) ΔE_{kin}, ΔE_{int}, and the sum of the two respectively, for two interacting p_z orbitals, and (d-f) the same for a p_x orbital interacting with a p_y orbital.

As such, the simple proportionality relationship is produced relating the force to the kinetic energy change at constant height:

$$F(X,Y) \quad \propto \quad \Delta E_{\text{kin}}(X,Y). \tag{7.10}$$

7.2 Imaging C_{60}

The model thus far takes into account the interaction between a single electron associated with an atomic orbital of the tip, and an electron associated with an atomic orbital of the sample. However, this is the simplest possible case, and needs expanding if it is to be used for modelling real, multi-electron systems. The first system to be considered will be where a C_{60} adsorbed on a generic surface, is imaged through a 1s tip state, which physically, could represent a hydrogen terminated probe. In this way, it is only the sample that is multi-electron in nature.

Unlike STM, which probes only the frontier orbitals, AFM involves the interaction between *all* the electrons present in the system. Thus, for the C_{60} molecule

present on the sample the electronic states associated with each of the 360 electrons present within the molecule would need to be considered to completely describe the interaction. However, if the distance between the tip and sample is not to small, the increased separation will mean that the wavefunction associated with the lower lying orbitals will already have decayed sufficiently, such that the overlap between them and the tip orbitals will give a negligible change in kinetic energy. As such, it is only the valence electrons which need to be considered within this region. For molecules, the electronic wavefunctions relating to the valence electrons may be described by the associated MOs, and as such HMO and EHMO theory may be used in the modelling.

If initially, only one of the electrons in the sample is considered, $\Psi(1)$ can be defined as the sample electronic state given by the MO under consideration, and, assuming we are using an LCAO method to determine the MOs, can be defined as the sum:

$$\Psi(1) = \sum_i c_i \chi_i, \tag{7.11}$$

where i sums over the atomic orbitals χ, that make up the basis, and c_i is the ith coefficient defined by the MO. With the tip wavefunction, $\Psi(2)$, defined as a 1s orbital, the overlap of the two wavefunctions is:

$$\begin{aligned} S_{12} &= \langle \sum_i c_i \chi_i | 1s \rangle \\ &= \sum_i c_i \langle \chi_i | 1s \rangle , \end{aligned} \tag{7.12}$$

resulting in a sum of atomic orbital overlaps, which can be easily calculated either using GTOs, or with STOs using the expressions in appendix A.

Equation (7.12) provides a simple way to obtain a numerical value for $\eta(1)$ and $\eta(2)$ when the centres of the two wavefunctions are fixed. Turning our attention to equation (7.4) to obtain the change in kinetic energy for this system, substitut-

ing the definitions of $\Psi(1)$ and $\Psi(2)$ gives:

$$\begin{aligned}\Delta E_{\text{kin}} &= \eta(1)^2\langle\sum_i c_i\chi_i|\hat{T}|\sum_j c_j\chi_j\rangle+\eta(1)\eta(2)\left(\langle\sum_i c_i\chi_i|\hat{T}|1s\rangle+\langle 1s|\hat{T}|\sum_i c_i\chi_i\rangle\right)\\ &\quad+\left(\eta(2)^2-1\right)\langle 1s|\hat{T}|1s\rangle\\ &= \eta(1)^2\sum_i c_i\sum_j c_j\langle\chi_i|\hat{T}|\chi_j\rangle+\eta(1)\eta(2)\sum_i c_i\left(\langle\chi_i|\hat{T}|1s\rangle+\langle 1s|\hat{T}|\chi_i\rangle\right)\\ &\quad+\left(\eta(2)^2-1\right)\langle 1s|\hat{T}|1s\rangle\,, \end{aligned} \tag{7.13}$$

where i and j sum over the atomic orbitals that form the basis set of the MOs. All of the integrals that need to be calculated in this expression can be done so either through an STO or GTO basis, and as such, it is possible to calculate the kinetic energy change associated with the interaction between a 1s electron and an electron within a given MO. To extend this to the full interaction, it is necessary to sum the kinetic energy change induced for each electron under consideration within the molecule. Furthermore, as the interaction is formed from a combination of atomic orbital interactions, the proportionality relationship derived in equation (7.10) remains valid, giving the force at fixed tip height as:

$$F(X,Y) \propto \sum_i \Delta E_{\text{kin}}\left(\Psi(1)_i\right), \tag{7.14}$$

where i sums over the kinetic energy change associated with each MO (given by $\Psi(1)$). In obtaining this relationship, the assumption is made that the change in one of the tip MOs due to the orthogonalisation does not directly alter the form of the other MOs, and the interactions are independent of one another. While the electron distribution of one electron does in principle affect the others through the Pauli exclusion principle, this effect is assumed negligible, as the change in the MOs is expected to be small.

7.2.1 Theoretical Images

With the theoretical model in place, it is now possible to obtain theoretical images of a constant height AFM scan. The first images to be considered will be those obtained when the tip takes a simple s-type state (as considered above).

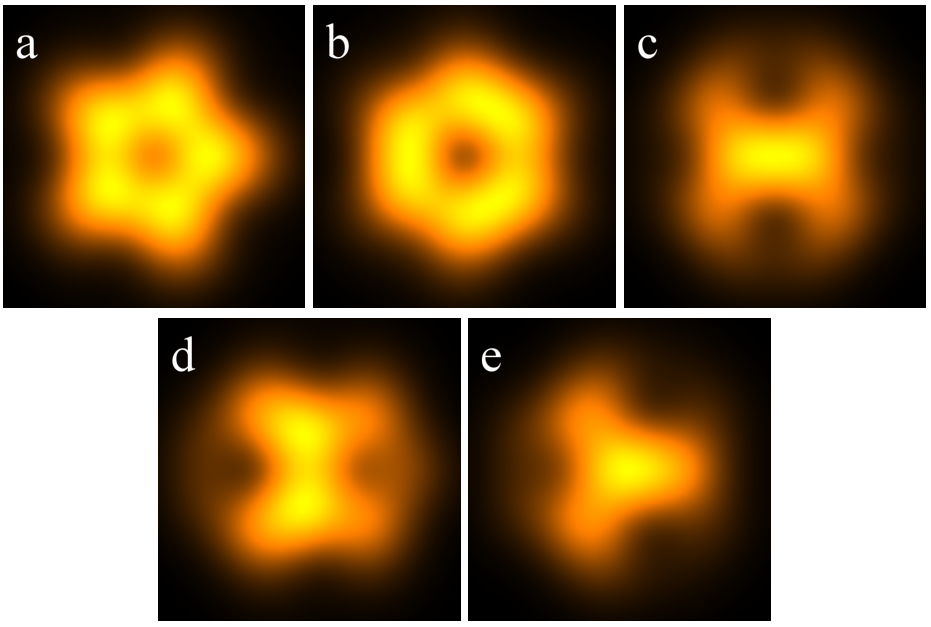

Figure 7.2: Theoretical AFM images of the interaction between a C_{60} and an s orbital, modelling the images obtained when the C_{60} is oriented with (a) a pentagonal face, (b) a hexagonal face, (c) a 6-6 bond, (d) a 5-6 bond, and (e) an atom, in the Z direction of the scan.

This will then be extended to look at molecular interactions by considering the C_{60}-C_{60} repulsive interaction, and the images obtained from this.

7.2.2 C_{60} Interacting with an s-type Tip

Through equation (7.14), and by using HMO theory to obtain the MOs, the repulsive force can be obtained as a function of the X and Y scan directions. A constant height image can then be obtained through a theoretical raster scan over X and Y, by evaluating the force at each point. The images shown in figure 7.2 show what would be obtained for a selection of molecular orientations of the C_{60}. For these images, only the repulsive interaction is considered, and as such relates to the imaging that would be obtained well within the repulsive regime, where the Pauli force is considerably greater than the attractive interaction. Each of the images shown are taken with a tip centred $9.5a_0$ from the C_{60} molecular centre.

As a comparison to the images shown in figure 7.2, a theoretical constant height scan of the electron density is shown for the pentagon and hexagon prone ori-

entations in figure 7.3. It can be seen that similarities exist between the two images, with the electron density picking out the most prominent features imaged in AFM. Due to the nature of the Pauli repulsion, which has been shown to be related to the overlap of the electronic states of the tip and sample, it is to be expected that regions of high electron density correlate with regions of high repulsion.

In the simplified assumption that the repulsive force observed originates from the interaction with a single tip electron, the link between the electron density and the resultant AFM image can be investigated. The electron density is a measure of the probability of finding an electron at a given point in space. For a fixed separation and tip state, it is clear that in the regions where the electron density is higher, the overlap with the tip state will also be higher, and it is this that causes the resulting change in kinetic energy, and hence the repulsive force. The overlap is also dependant on the wavefunction of the tip state, and more particularly the rate of decay of that function. It therefore follows, that for a highly localised electron that has a rapidly decaying wavefunction, the resultant force will more closely map to the electron density than for a slowly decaying function. To see this in the theoretical images, a purely theoretical tip state can be constructed from a single Gaussian. By increasing the exponent, the tip state becomes more localised, with the impact this has on the images then observable. Figure 7.4 shows four cases for the hexagon prone surface molecule, where this exponent has been taken to be -0.1, -1, -10 and -100. It can be seen that when the electron is highly delocalised (i.e. a low magnitude exponent is used), less detail is seen in the image, and as the magnitude of the exponent increases, more and

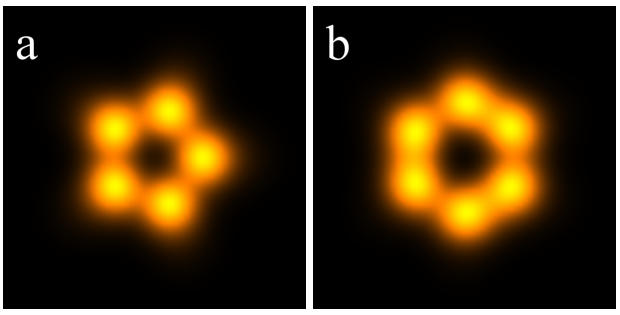

Figure 7.3: Theoretical scan of the electron density of C_{60} obtained through HMO theory for a pentagon and hexagon prone surface adsorbed molecule.

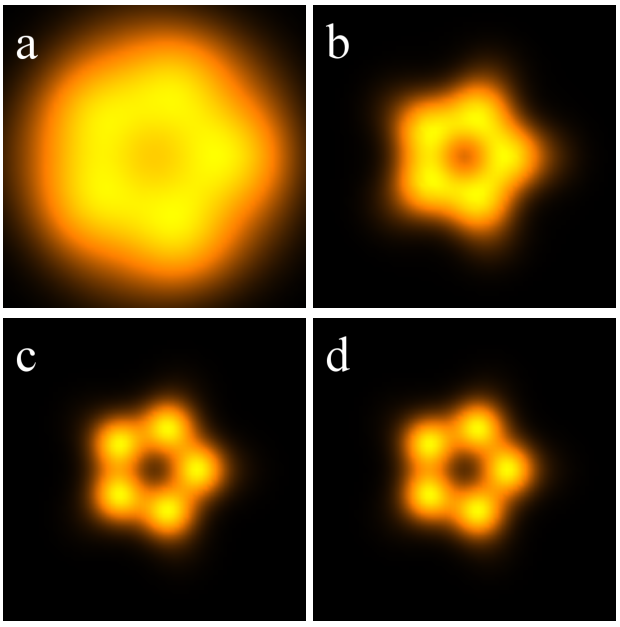

Figure 7.4: Theoretical scans of the repulsive force observed when a C_{60} adsorbed with a pentagonal face prone to the surface interacts with a tip state described by a normalised Gaussian of varying decay rate. The exponents of the Gaussians are (a) -0.1, (b) -1, (c) -10, (d) -100.

more detail is observed.

7.2.3 Choosing the Ideal Tip State

The increase in detail as the exponent of the Gaussian increases has implications with respect to desired tip states. The more localised the tip electron, the more detailed an AFM image should be obtainable. However, this is only usually true if the interaction is predominantly with a single tip electron. It is expected (and simulations suggest) that this is a valid assumption if the valence electrons are s and/or p like in nature. With respect to the p orbitals, if one of these orbitals was to point straight down from the tip (i.e. a p_z orbital), it can be assumed that it would form the predominant contribution to the kinetic energy change, as the two orthogonal p_x and p_y orbitals decay rapidly in the z direction, and the s orbital of the same level will have a similar effect on the image, whilst also decaying slightly more rapidly. As such, quantitatively, the images from tips that possess this characteristic can be modelled in this way. Furthermore, for the purpose of imaging these are the ideal form of tips both in STM and AFM, and allow the easiest interpretation of the experimental data.

The elements with the most rapidly decaying valence orbitals are those that possess f-type orbitals in their valence shell. However, the spatial distribution of the f-type orbitals makes it highly unlikely that there would only be one orbital that has a significant contribution to the Pauli repulsion. The ideal orbital for imaging would be an f_{z^3} orbital pointing in the z direction, as this would allow the predominant interaction to be with a single lobe of the orbital. However, unlike the case for the p orbital basis, the orthogonal orbitals to the f_{z^3} orbital would not decay rapidly in the z direction in all cases. Thus, any electrons present in these orbitals would contribute to the repulsion and convolute the resultant AFM image. Likewise, there is a similar situation when considering valence d orbitals. The ideal orbital for imaging would be the $d_{2z^2-x^2-y^2}$ orbital pointing in the z direction. However, contributions from the d_{xz} and d_{yz} orbitals would also be expected to have significant contribution to the repulsive force, and again, the resultant image would be a convolution of these states.

With this in mind, it would seem that to obtain the highest resolution, and most easily interpretable AFM images, the ideal tip would be formed from an element with s or p character in the valence shell. This restricts the selection to the first two columns of the periodic table for those elements with s valence electrons, and the final four columns for those with p character (with the exception of helium, which has a full s level, although this could not be used as a SPM probe). As we require the electrons to be localised as much as possible, elements which contain more protons are preferable, as this increases the rate of decay of the associated orbitals. As well as this, the closer the orbital to the nuclei, the more localised the electron, and as such, elements which have valence electrons with a low principal quantum number would be beneficial. This suggests that elements in the top right of the periodic table would make the most suitable AFM tip states, with the optimum being fluorine (as the low n noble gases can not be bonded to an SPM probe). This can be seen if the Slater exponent of various elements is considered as shown in table 7.1. All of these values are taken from Clementi and Raimondi [89], with the exception of the Slater exponent for xenon, which is taken from Clementi *et al.* [96].

Table 7.1: The Slater exponents of the valence orbital of various elements

Element	Slater Exponent	Orbital type
Lithium	0.640	2s
Carbon	1.568	2p
Oxygen	2.227	2p
Fluorine	2.550	2p
Silicon	1.428	3p
Chlorine	2.039	3p
Bromine	2.257	4p
Xenon	2.485	5p

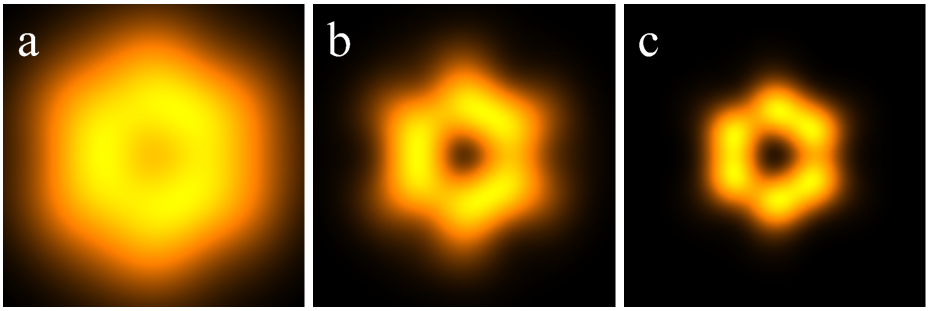

Figure 7.5: Theoretical AFM scans of C_{60}, using a (a) lithium, (b) boron, and (c) fluorine tip. For these tips, the Slater exponent roughly doubles between each image going from (a) to (c).

The information in table 7.1 shows the trends described whereby the further right in the periodic table the greater the Slater exponent, and the more localised the electron will be. Also, as the principal quantum number increases within the same column, the Slater exponent decrease. If we briefly return to C_{60} it is possible to run theoretical scans of how the images would appear for a selection of these different tip states. Figure 7.5 shows this for the cases where a lithium, boron and fluorine tip are used and the difference in the detail observed can be seen. It can be seen that for lithium, the uppermost features of the images are more spread out compared to the fluorine tip, although interestingly, more of the detail of the side of the C_{60} is obtained with a lithium tip. This is again due to the localisation of the electron, as the more disperse electron associated with the lithium tip has a comparatively greater overlap with the lower regions of the molecule, and comparatively less overlap with the uppermost parts, when compared against the fluorine tip. For planar molecules this would not be significant, although when considering three dimensional molecules this could be a desirable characteristic of the tip.

Xenon is included in table 7.1, as even though it is a noble gas, it is sufficiently far down the periodic table that it is more easily ionised, and hence can be bonded to the SPM probe. Indeed, work undertaken by Mohn *et al.* [44] compared the AFM images obtained when using a Xe and a CO functionalised tip. It was found that although high resolution was achievable with a Xe tip, a clearer image was obtained through CO functionlisation. This is in spite of oxygen having a lower Slater exponent, and hence less localised electrons. A simple explanation for this could be that the p orbital of the xenon atom is pointing at an angle away from the z axis, and there is a contribution coming from the orthogonal orbitals, which will hence have a slower decay rate in the z direction. For CO this is not a problem, as it is known that the molecule is bonded with the C-O bond in the z direction, and hence there will be a p orbital pointing in the z direction (this will be discussed in more detail in chapter 10). Thus, the problem in obtaining the ideal tip is not just in having elements that have a rapid decay of their valence shell wavefunctions, but also in ensuring the orbitals are aligned with the z direction of the scan, which is inherently difficult, and is also part of the reason why CO is so successful with high resolution AFM imaging. The results here imply that if a similar molecule could be utilised with fluorine at the tip apex (there are numerous fluorocarbons as possibilities), the maximum resolution of imaging would be obtained.

7.2.4 C_{60} Imaging C_{60}

Previously, the repulsive interaction has only been considered with a single atomic orbital of the tip. This now needs extending to look at the case where two C_{60}s are interacting, which results in a large increase in the computational expense of the calculation. Instead of considering the interaction with one orbital, the interaction with all the p orbitals that form the basis in HMO theory needs to be considered, as well as the interaction between each MO of one molecule with each MO of the other. Despite this large computational increase, images can still be constructed within a reasonable time frame if only the interaction between the

significantly contributing orbitals is considered. To do this, the overlap between all the orbitals on one molecule with all the orbitals on the other is calculated, and only those orbitals with a large overlap are considered in the calculation of the kinetic energy change. As all the overlaps are still calculated, the complete orthogonalisation calculation remains, which greatly reduces the error this assumption imparts on the calculation. For the images shown here, all overlaps greater than 10% of the largest overlap are considered at each point of the raster scan. Select scans were also undertaken reducing this amount to 1%, with no difference observed in the images.

Figure 7.6 shows a selection of the images obtained for a variety of different tip and sample orientations. The images chosen are where highly symmetric orientations are aligned to show the symmetry of the resultant images. As with the STM images, any symmetry operations that remain in the two molecular orientations are preserved in the resultant AFM images.

To understand these images it is again necessary to consider the electron density associated with each molecule. Figure 7.6a and b represent the case where one of the 6-6 bonds on each molecule form the predominant interaction, with figure 7.6a showing the image when the two 6-6 bonds are aligned, and figure 7.6b showing the case where they are perpendicular to one another. The electron density of C_{60} is greater along the 6-6 bond than the 5-6 bond, and slightly greater towards the atomic centres than the middle of the bonds, so in both cases, the interaction is with regions of high electron density. When the bonds are aligned, the maximum intermolecular electronic overlap (and hence kinetic energy change) occurs at the centre of the image, when the atoms and bonds of each molecule align in Z. Moving away from the centre in the line of the bond preserves the electronic overlap to a greater extent than when moving perpendicular to the bond, and as such the central feature is elongated in the direction of the bonds (in the X direction in figure 7.6a). When in the centre of the scan, the molecules are situated with the bonds perpendicular to one another (figure 7.6b), the predominant electronic overlap originates from the interaction between the centre of the two bonds. As the electron density is slightly greater

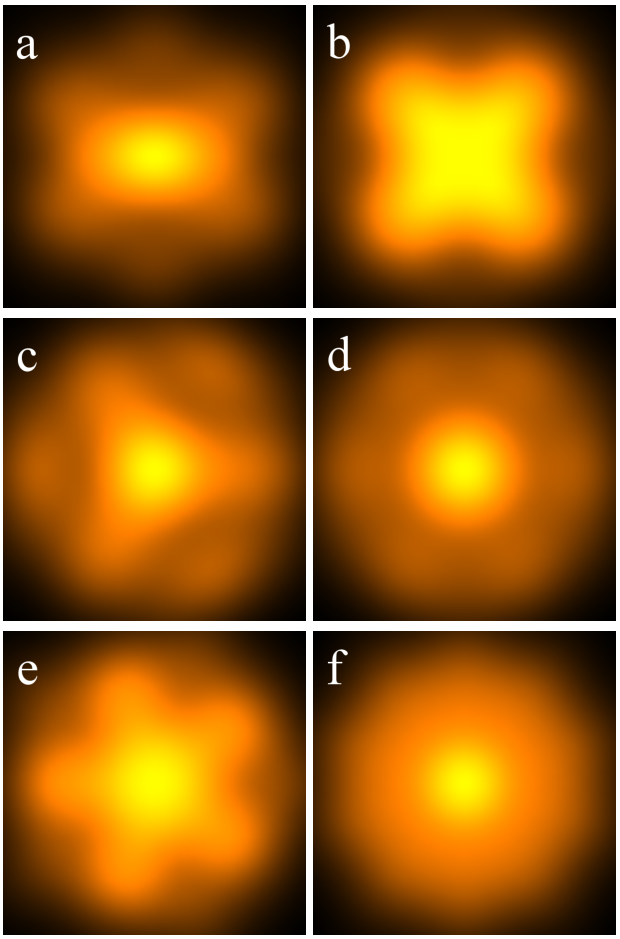

Figure 7.6: Theoretical scans of the repulsive interaction between two C_{60} molecules. The molecular orientations are (a) both molecules have a 6-6 bond interacting, with the bonds on each molecule aligned, (b) as (a) but with the 6-6 bonds on each molecule perpendicular to each other (i.e. a $\frac{\pi}{2}$ rotation around Z of the tip molecule), (c) two hexagonal faces directly aligned, (d) as (c) but with a rotation of $\frac{\pi}{3}$ around Z of the tip molecule, (e) two pentagonal faces aligned, and (f) as (e) but with a rotation of $\frac{\pi}{5}$ around Z of the tip molecule.

towards the atomic centres, this does not relate to the strongest interaction observed. This occurs (very close to), when two atomic centres are aligned in Z, and hence the image has a four-fold symmetry, relating to each case where two of the atoms associated with the 6-6 bonds on each molecule align. Interestingly, this introduces an image with a level of symmetry not present in the individual C_{60} molecules (namely a C_4 rotation). This occurs, as the system of the two molecule when aligned in this way is described by the S_4 point group, which contains the four-fold S_4 improper rotation.

Figure 7.6c and d show the repulsive interaction when two hexagonal faces interact. Again, considering the electron density allows the images to be explained. In figure 7.6c, the two interacting hexagonal faces are aligned with a mismatch

in the bonds such that a 6-6 bond faces a 5-6 bond and vice-versa. When the two molecules are aligned in Z, the atomic positions approximately align, and so a strong interaction is still observed, although the intermolecular electronic overlap is not maximised as the bonds are mismatched. When moving away from the centre of the image (and hence away from the alignment of the molecules in Z), certain directions result in a stronger interaction. This is again due to the intermolecular overlap, as moving the tip away from the centre in the direction of a 5-6 bond of the sample molecule, results in an increasing overlap between two pairs of 6-6 bonds, whereas moving away in the direction of a 6-6 sample bond results in only one pair of 6-6 bonds overlapping, and hence a weaker force is observed. In figure 7.6d, the molecules are aligned with the bonds matching (i.e. a 6-6 bond faces a 6-6 bond and a 5-6 bond faces a 5-6 bond), and as such a strong interaction is observed at the centre of the image. In this case moving away from the centre greatly reduces the force interaction, although moving along the line of a pair of bonds maintains some of the electronic overlap, resulting in a slightly greater force, and the resultant six fold symmetry that is observed in the image. This result shows the importance of the electron density as opposed to the atomic centres in understanding the repulsive force, as in both cases, the hexagonal faces are centred with atoms aligned in Z. If the atomic centres were playing a key role, it would be expected that the images would be very similar, which is not what is predicted.

In figure 7.6e and f, two pentagonal faces interact, and as such it is 5-6 bonds that are involved in the interpretation. As these do not carry much of the electron density of C_{60}, it is predominantly the atomic centres that contribute to these images. Figure 7.6e shows the case where the atomic positions are misaligned in Z, such that each atom aligns with a 5-6 bond on the other molecule. Although these atomic positions do not align, a strong interaction can still be expected at the centre of the image, as in this position all of the atomic centres contribute equally to the force, and all have a significant (if not optimal) effect on the observed force. When moving the tip away from the centre, five-fold symmetry is present in the image as the strongest interaction occurs when two atomic centres

related through a diagonal of the pentagonal face, align with two corresponding atoms on the other molecule. This occurs when moving the tip molecule such that the centre of the 5-6 bond travels over the atomic centre of the surface adsorbed molecule. Figure 7.6f shows the case where the atomic centres are aligned, and hence, a strong interaction is observed at the centre of the image. In this case, if the tip is moved away from the centre, the force reduces rapidly. An indication of a ten-fold rotation can faintly be observed in the repulsive image, relating to the slight increase in intermolecular overlap if the tip is moved such that an atomic centre follows the line of a 5-6 bond, although this difference is barely observable in the image.

One important result to come out from this is that for the C_{60}-C_{60} interaction, there is no way to determine which of the molecules is oriented in which way, just that the relative orientation of the two is known. That is that the images obtained are identical if the orientation of the two molecules is swapped. This is because the repulsive force is dependant on the electron density of both molecules, which, with the exception of slight deviations due to the bonding interactions, is expected to be the same in both cases. This is in comparison to STM, where the orientations of each molecule *can* be determined, as the image is formed form the HOMO of one molecule and the LUMO of the other, which are different functions.

7.3 Modelling the Attractive Interaction

So far in this chapter it is only the repulsive force which has been considered, with these images relating to the case where the Pauli repulsion is significantly greater than the long range interaction. However, if this is the case it would be expected that a molecular distortion would occur due to the large forces involved which could change the observed image. As such, the images produced so far can only be considered an approximation of the real case where the attractive interaction is negligible.

If images are obtained around the region of the minimum energy separation (r_m in relation to a LJ potential), the net force acting between the tip and sample will be small. As such, any molecular distortion is expected to be minimal, and the results obtained should accurately predict how the real AFM images would be observed. However, the minimum in energy is formed due to the competing attractive and repulsive interactions and as such it is necessary to incorporate this long range interaction into the imaging, and it is this that shall now be considered.

7.3.1 C_{60} Interacting with an Atomically Sharp Tip

The attractive interaction between C_{60} and a given tip atom can be modelled by considering the LJ potential between a single carbon and the atomic species under consideration. By associating a LJ potential with each atomic position on the C_{60}, the full potential energy expression at a given tip position can be formed through a simple summation of the functions. This follows the idea previously proposed by Girifalco [97], where the C_{60}-C_{60} interaction was considered as a collection of interacting graphite like carbon atoms (this will be considered in more detail shortly).

As the repulsive interaction is already considered using the techniques outlined above, it is only the attractive r^{-6} relationship of the LJ potential that is required. It has been shown that the kinetic energy change is approximately proportional to both the interaction energy, and the force, and as such it is this kinetic energy change which has been plotted previously. This means that the magnitude of the repulsive interaction is not known, so to incorporate both the attractive and repulsive interactions into a single form, a variable must be present which varies the strength of the repulsive term. Thus, the complete form of the potential energy is given by the equation:

$$E = \kappa \sum_i \Delta E_{\text{kin}} \left(\Psi(1)_i\right) + \epsilon \left(-2\frac{r_m}{r}\right)^6, \tag{7.15}$$

where κ is varied to increase or decrease the strength of the repulsive interaction. As κ is unknown, it is possible to simplify this expression by dividing through

by 2ϵ, to give the simple form:

$$E' = \kappa' \sum_i \Delta E_{\text{kin}} \left(\Psi(1)_i\right) - \left(\frac{r_m}{r}\right)^6, \tag{7.16}$$

or for the force:

$$F' = \kappa' \sum_i \Delta E_{\text{kin}} \left(\Psi(1)_i\right) + \frac{\partial}{\partial Z}\left(\frac{r_m}{r}\right)^6, \tag{7.17}$$

noting that r is a function of the tip height Z, and the negative derivative is taken to find the force. Also, even though ΔE_{kin} is a function of the Z tip direction, it has been shown that the energy and force are roughly proportional, so the effect of this derivative is lost in the multiplicative constant κ. In using these equations the only new information required is therefore r_m, which is chosen depending on the tip state.

The relative contribution of the repulsive interaction can be divided into three main categories. A large value of κ' relates to the case considered in the previous section where the repulsion dominates over the attractive interaction. Opposite to this is when κ' is small, which relates to the case where the attraction is dominant, resulting in a spherical, featureless, AFM image. The region of interest is where κ' is chosen such that both interactions contribute. Within this region, κ' can take a range of values where the general features of the image remain the same, it is only the relative intensities which change.

In figure 7.7, the interaction is assumed to be between C_{60} and an s orbital associated with a hydrogen atom (to match the case considered in figure 7.2). r_m is chosen to be $5.7a_0$, although it is found that this value does not have a great influence on the resultant image as κ' may be varied to compensate. Clearly, this is particular to the method, and if the magnitude of the interaction was important then a more accurate value of r_m may be required. However, as the images only aim to qualitatively describe the experimental AFM, κ' can be varied accordingly. The value of κ' in figure 7.7 has been chosen such that the repulsive interaction is slightly greater than the attractive interaction to pick out the main features of the image. The height of all the scans has been chosen at $12a_0$ above the molecular centre of the C_{60}. This means that the separation at the centre

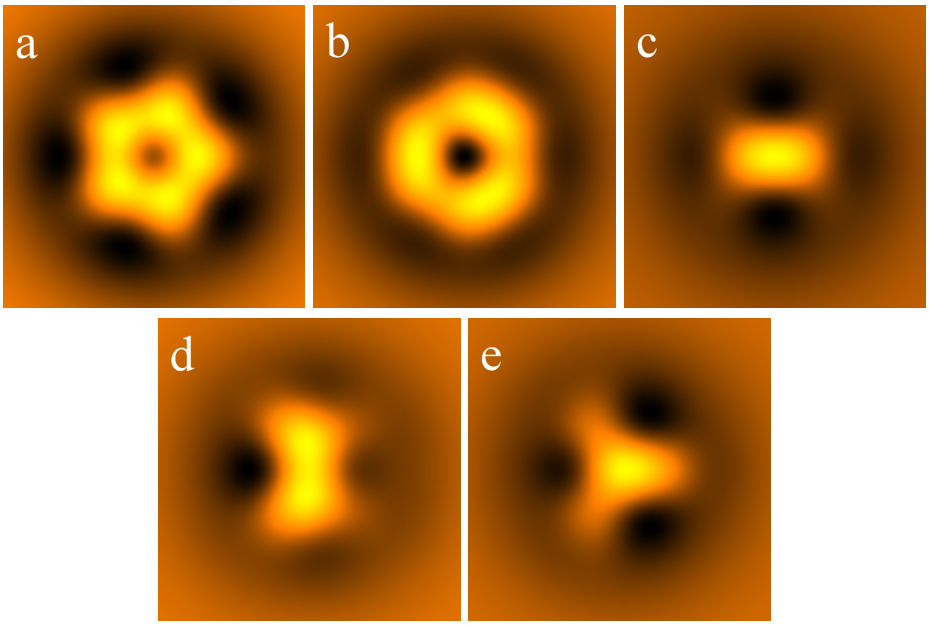

Figure 7.7: Theoretical AFM scans incorporating both the attractive and repulsive interaction for when C_{60} interacts with an s orbital associated with a hydrogen atom. The C_{60} is oriented with (a) a pentagonal face, (b) a hexagonal face, (c) a 6-6 bond, (d) a 5-6 bond, and (e) an atom, in the Z direction of the scan.

of the image is slightly closer than r_m, so the repulsion should dominate, while further away from the image, the attractive interaction would be expected to be more significant.

Figure 7.7 shows that by incorporating the attractive interaction the uppermost features of the repulsive interaction are accentuated due to the dark regions within the scan. This is due to the combination of the positive and negative interactions which increases the range of the linear scale. Where the repulsive interaction is strong a large positive value is obtained for the force, resulting in the bright yellow regions in the plots. Where a weak repulsion is observed, the attractive (negative) force dominates, and a large negative value is obtained resulting in the black regions.

Having incorporated both interactions into the imaging, it is then possible to compare the results with those obtained experimentally. Figure 7.8 shows a comparison between the theoretical image obtained using the methods described, and an experimental image obtained with an uncertain (although likely silicon) tip state. The image has been constructed at a height of $14a_0$, using $r_m = 7.5a_0$ to model the carbon-silicon interaction, with the C_{60} assumed to interact with a

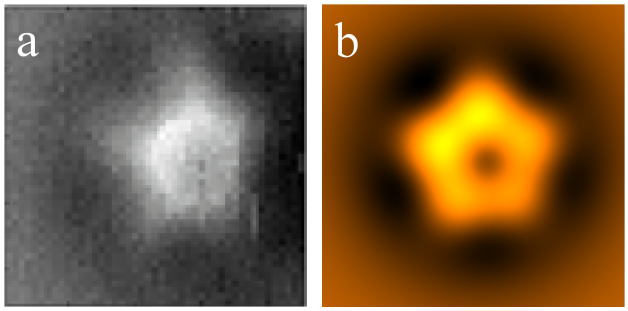

Figure 7.8: Experimental (a) and theoretical (b) comparison of the AFM image obtained when a C_{60} interacts with an uncertain tip state, likely to be silicon.

p_z orbital of silicon. As can be seen, excellent agreement is found between the two when the C_{60} is oriented on the surface with a tilt slightly away (around 3 degrees) from the pentagonal face towards the 5-6 bond.

7.3.2 C_{60}-C_{60} Interaction

The attractive interaction between two C_{60} molecules has been considered in the past in the form of the Girifalco potential [97], which treats the interaction through a LJ-type potential distributed evenly over two hard spheres. This has been shown to accurately predict the experimentally observed interaction, particularly in the attractive regime [91]. The empirical form of the Girifalco potential is based on the carbon-carbon interaction within graphite, and is given by the equation (in atomic units):

$$E = \left(\frac{5.07}{r'}\right)^{12} - \left(\frac{3.89}{r'}\right)^{6}, \tag{7.18}$$

noting that here, r' is the separation between the surface of the hard spheres with a radius of $13.5a_0$.

Using the r^{-6} relationship within the Girifalco potential, theoretical AFM images can be constructed of the C_{60}-C_{60} interaction in the same way as shown for the interaction with an s-type tip above. The minimum potential energy occurs within the Girifalco potential when the molecular centres of the two C_{60}s are separated by around $19a_0$. Thus, the theoretical images are constructed with a closest separation of $18.5a_0$, to correspond to the case where the attractive and repulsive interactions both contribute significantly to the force. The strength of

the repulsive interaction is again varied to obtain a suitable theoretical image that shows the main features to be expected experimentally.

Figure 7.9 shows the images relating to the same cases considered in figure 7.6, but with the attractive interaction incorporated. Again, it can be seen that the uppermost features of the image are emphasised due to the increased range of the observed force. Also, a lot of the detail relating to the weaker repulsive interaction is lost when incorporating the attractive force, as is particularly shown in figure 7.9d and f, when two hexagonal and pentagonal faces interact respectively. In these two images, where the atomic positions align at the origin, a very small deviation from the centre results in a greatly reduced repulsive force (as explained earlier). However, as the attractive force is still very strong in this region, a black ring relating to this strong negative force is observed.

Similarly to the STM work considered in the previous chapter, the techniques shown here allow the repulsive force and the AFM images to be modelled for any system where the MOs may be written as a LCAO. Although, in this chapter the focus has again been on C_{60}, the methods are still expected to be widely applicable. At this stage in this work no comparison with experiment is given, as at the time of writing only one experimental image relating to the C_{60}-C_{60} interaction has been obtained. This will be considered in the following chapter.

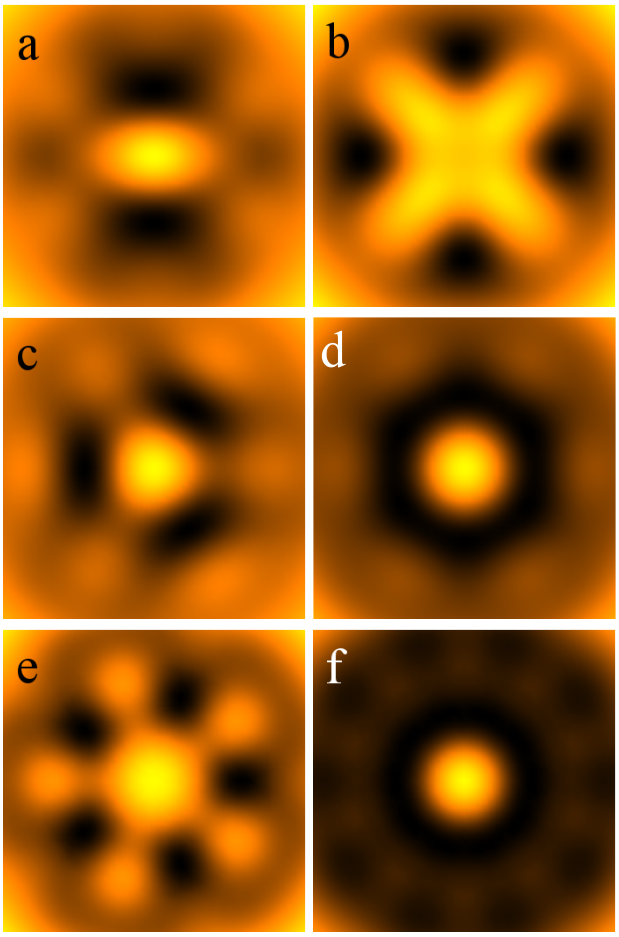

Figure 7.9: Theoretical scans of the attractive and repulsive interaction between two C_{60} molecules. The molecular orientations follow that in figure 7.6, where (a) both molecules have a 6-6 bond interacting, with the bonds on each molecule aligned, (b) as (a) but with the 6-6 bonds on each molecule perpendicular to each other (i.e. a $\frac{\pi}{2}$ rotation around Z of the tip molecule), (c) two hexagonal faces directly aligned, (d) as (c) but with a rotation of $\frac{\pi}{3}$ around Z of the tip molecule, (e) two pentagonal faces aligned, and (f) as (e) but with a rotation of $\frac{\pi}{5}$ around Z of the tip molecule.

Chapter 8

From STM to AFM

In the previous chapters, techniques have been set out to model both STM and AFM images of C_{60}, both when adsorbed on a surface, and as part of a functionalised SPM probe. In this chapter, these techniques will be used to obtain the molecular orientations of two C_{60}s, one adsorbed on the surface, and one adsorbed on the tip. A complete set of images will be obtained to compare with experiment. Firstly, a comparison will be made with STM images, where to begin with, the surface-adsorbed molecule will be imaged with a 'clean' s-type tip. Then, images will be obtained of the tip-adsorbed C_{60} through reverse imaging from the adatoms of the Si(111)-(7x7) surface, before the images produced through the convolution of tip- and sample-adsorbed molecules are shown. The tip-adsorbed molecule will then be imaged in joint STM/AFM mode (where a small bias is applied during AFM), and theoretical images of the functionalised tip produced to model this, before finally, the AFM image obtained when the two molecules interact is modelled.

Figure 8.1 shows the first experimental images to be considered. Here, an area has been scanned with a tip that gives images that would be expected with an s or p_z type tip state (i.e. the images resemble how the MOs of the molecule would appear). The two molecules under consideration are indicated by the two circles, with the molecule within the solid circle remaining adsorbed on the surface throughout the experiment. The molecule surrounded by the dashed circle has

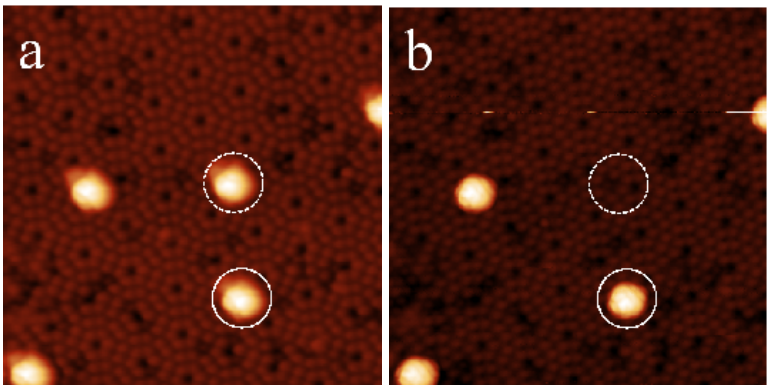

Figure 8.1: Experimental STM images showing the pick-up of an individual C_{60} molecule. (a) shows the scan region before pick up of the molecule indicated by the dashed circle. (b) shows the region after pick up, noting that the molecule is no longer present within the scan. The molecule surrounded by the solid circle is the surface-adsorbed molecule that is analysed.

been deliberately adsorbed onto the apex of the probe to form the C_{60} functionalised tip, as can be seen from the two figures, where in the second image, the molecule is no longer present (note the defect to the right of the surface-adsorbed molecule that ensures the same area is being imaged).

The image of the surface-adsorbed molecule is enlarged in figure 8.2 for both tip states shown in figure 8.1. Using the techniques outlined in this work, the molecular orientation is deduced for both the tip- and sample-adsorbed molecules. In this instance, the surface-adsorbed molecule is present in the R_f configuration, with the molecule situated approximately with an atom prone to the surface. The tip-adsorbed molecule is slightly harder to determine, as the interaction with the adatom produces a somewhat featureless image. However, the image obtained when the two C_{60}s interact is suitably distinctive to determine the molecular orientation. The theoretical comparison is shown in figure 8.1 alongside filtered images of the experimental data. The filter applied is a difference of Gaussians routine, built into the edge detection feature within the GIMP software package. This relies on blurring the image using two different Gaussians of different radii, with the resultant images then subtracted from one another to produce the filtered image. Unlike previously, a filter is used in this case as the raw experimental data has produced a slightly blurred image in which it is difficult to detect the key features. By introducing the filter, the edges are much clearer in the image, allowing for more accurate interpretation of the data. The tip-adsorbed C_{60}

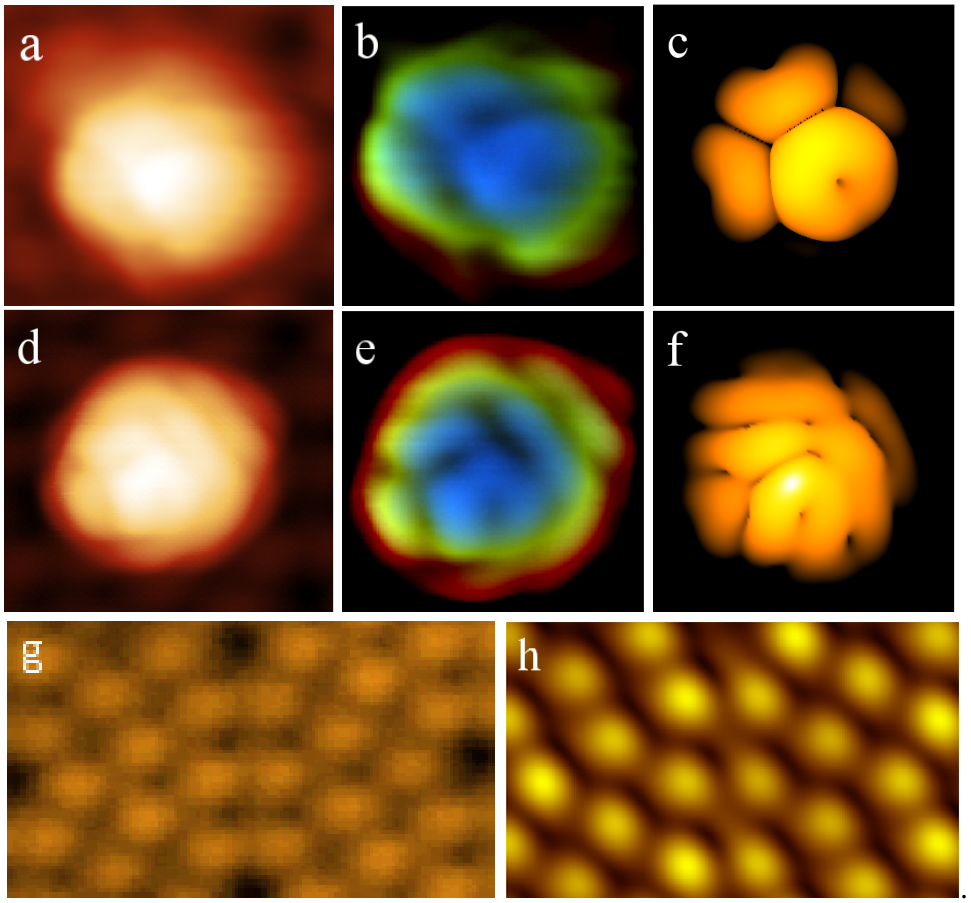

Figure 8.2: Comparison of experimental and theoretical STM images. (a) shows an experimental constant current STM image of the surface-adsorbed C_{60} under analysis, before tip-functionalisation, (b) shows filtered images using a difference of Gaussians technique, and (c) is the theoretical interpretation of the image. (d-f) show equivalent results for after tip functionalisation with the C_{60}, and (g) shows the experimental image from the adatom-C_{60} interaction, alongside the theoretical interpretation (h).

is oriented with a slight tilt away from the pentagonal face towards the 5-6 bond. The experimental data obtained in this case is not as clear as some of that shown previously, making interpretation of the data slightly more ambiguous. While in each case the individual images do not conclusively suggest particular molecular orientations, the fact that there is agreement between all the images (as will be shown) gives a strong indication that the orientations have been correctly deduced.

The next step experimentally is to bring the probe closer to the sample to allow imaging in AFM. However, when changing between STM and AFM, the removal of the bias, as well as possible fluctuations in the tip state, means that the tip-adsorbed C_{60} molecule may not remain in the same orientation. Thus, when

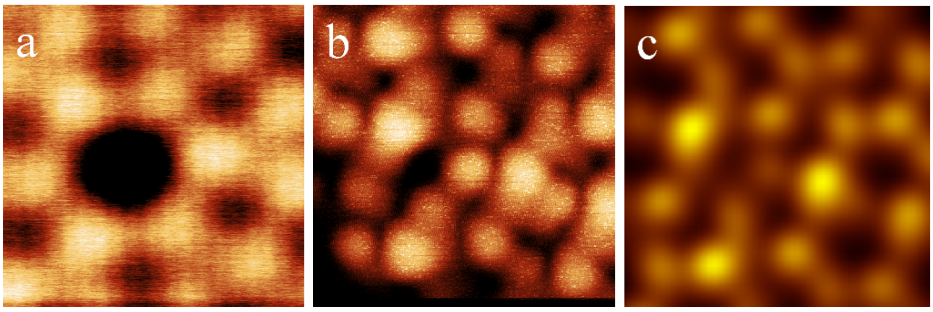

Figure 8.3: Experimental and theoretical interpretation of the joint AFM/STM images obtained where a C_{60} functionalised tip interacts with the adatoms of the Si(111)-(7x7) surface. (a) is the AFM image, showing only an attractive interaction, (b) shows the STM image obtained simultaneously to (a), and (c) is the theoretical interpretation of (b).

the mode of imaging is changed, the tip has been scanned over the adatoms on the surface to elucidate the tip structure. To do this, a corner hole, where the Si(111)-(7x7) unit cells join, is utilised. This is undertaken in two stages, the first of which is shown in figure 8.3. Here, an AFM image has been obtained within the attractive regime while simultaneously applying a small bias to induce a weak tunnelling current. In the attractive regime, the force interaction can be accurately modelled by treating the C_{60} as a hard sphere. As such a featureless image would be expected, depicting the spherical nature of the tip, and it is this that is observed. However, information can be obtained by considering the image formed from the tunnelling current. The experimental image does not appear to follow the positions of the adatoms, which suggests that the image is formed from a convolution of the tip-sample interaction from neighbouring adatoms. If the tip-adsorbed C_{60} is assumed to be in the same orientation as deduced previously, and a theoretical constant height scan over the corner hole is produced, the image shown in figure 8.3c is produced. The radial dependency on the electron distribution ensures that the further the C_{60} is imaged away from the surface, the larger the image obtained. Thus, it can be deduced that at the height at which the experiment has been undertaken, the imaging from the neighbouring adatoms combine to give the convoluted image seen. The MOs used to construct the theoretical image are not the same as those used to match the C_{60}-C_{60} STM image previously. However, as the bias differs between the two experiments, it is not unexpected that a different portion of the MO spectra is imaged.

It has been shown that the tip-adsorbed molecule has not changed orientation

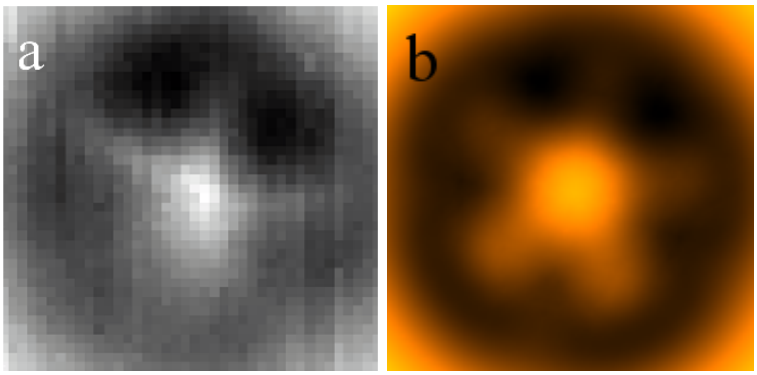

Figure 8.4: Experimental (a) and theoretical (b) AFM images for the C_{60}-C_{60} interaction.

when changing between STM/AFM. In the final part of the experimental work, a three dimensional force map was constructed looking at the interaction between the two C_{60}s. This was done using an atom tracking system [98], that allowed the tip to remain centred on the sample molecule during the scan, and thus alleviating problems with thermal drift. The results of this are shown in figure 8.4, alongside a theoretical interpretation obtained using HMO theory. The orientation of the sample molecule is the same as that determined earlier, although the tip-adsorbed molecule is tilted at a slightly different angle to give the most accurate match with experiment. However, the difference is only slight (around 1 degree), and with a strong repulsive force being observed, slight molecular deviations can be expected. The experimental images show a clear five-fold symmetry in both the energy and the force which is depicted in the theoretical interpretation. In addition, the additional darkening observed in the upper two features is also predicted theoretically, and is introduced due to the tilt away from the pentagonal face of the tip-adsorbed molecule.

A further selection of the experimentally derived images are shown in figure 8.5. These show the change in the images obtained with respect to the tip height. The important result here, is the relation between the interaction energy and the force. As expected, the image obtained for the energy change mirrors that obtained for the force, although the same features are observed in the energy at a lower tip height. This shows that even when the interaction is highly repulsive, the image from the energy change remains similar, showing that any molecular distortion, or deviation in the electron density, is not having a significant effect on the re-

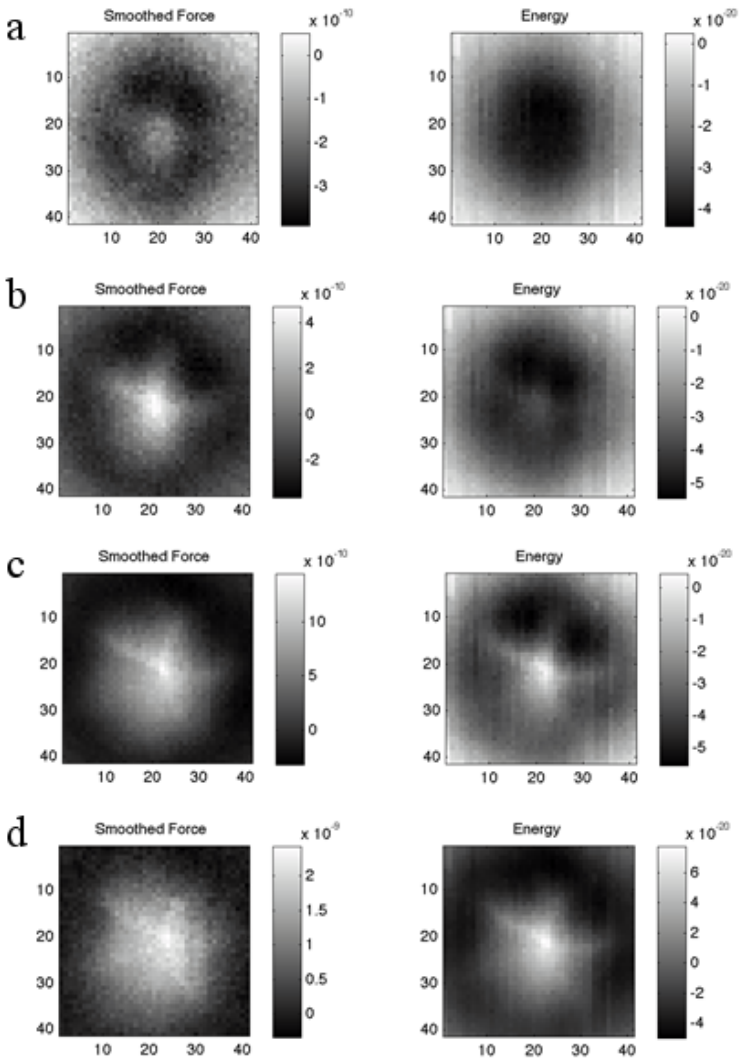

Figure 8.5: Selection of experimental AFM constant height images of the C_{60}-C_{60} interaction. The images show a decrease in tip height going from (a)-(d) [50]

sults, even at close proximity. This suggests that the method proposed may still be valid at closer separation than previously expected.

Chapter 9

Modelling the Repulsive Force Through the Electronic Overlap

In this section of the work, the ideas introduced in chapter 7 will be further examined, and the link between the observed force between two C_{60}s and the intermolecular electronic overlap will be investigated. In doing so, the lowest energy configuration for two C_{60}s will be postulated, with an explanation given as to why these results are the case.

9.1 The Electronic Overlap

In section 7.1, the relationship between the observed force, the interaction energy and the change in kinetic energy was discussed, with the result that they could all be approximated through a proportionality relationship with each other. An expression was derived to allow the change in kinetic energy to be calculated for two arbitrary atomic orbitals, which can then be used to look at two interacting MOs formed as a LCAO.

The expression for the kinetic energy change relies on the orthogonalisation of one of the MOs such that the Pauli exclusion principle is satisfied. This change is then defined as the difference in the kinetic energy of the orthogonalised and unorthogonalised states. Thus, the greater the change in the wavefunction, the

more it would be expected the kinetic energy changes. To understand this relationship, the expression for the Gram-Schmidt orthogonalisation (repeated below from equation (3.15)) utilised here can be examined.

$$|\Psi(2)'\rangle = \frac{|\Psi(2)\rangle - S_{12}\,|\Psi(1)\rangle}{\sqrt{1-|S_{12}|^2}}. \tag{9.1}$$

It can be seen from this that the orthogonalised wavefunction is a function of the overlap between the two unorthogonalised states. As previously, this expression may be split into two functions termed $\eta(1)$ and $\eta(2)$, where

$$\begin{aligned} \eta(1) &= -\frac{S_{12}}{\sqrt{1-|S_{12}|^2}} \\ \eta(2) &= \frac{1}{\sqrt{1-|S_{12}|^2}}. \end{aligned} \tag{9.2}$$

These two functions are related to each other through the normalisation of the state, and as such, both give an indication as to the extent of the orthogonalisation. It is therefore intuitive that both of these functions could relate to the kinetic energy change and hence the interaction energy associated with the Pauli repulsion.

9.1.1 Comparing the Force with the Degree of Orthogonalisation

To see how the degree of orthogonalisation relates to the interaction energy, a comparison can be given between the three dimensional scans of the kinetic energy change (which has been shown to be proportional to the force), and one of $\eta(1)$ or $\eta(2)$. As both of these functions relate to the extent of the orthogonalisation, and they are related to each other through the normalisation, it does not matter which is chosen, and so the simplest of these, $\eta(2)$ will be investigated.

Figure 9.1 shows a comparison of the repulsive C_{60}-C_{60} interaction considered in chapter 7 calculated through the change in kinetic energy (see figure 7.6), alongside images calculated from the intermolecular electronic overlap through $\eta(2)$, noting that in both of these sets of images, no attractive interaction is considered.

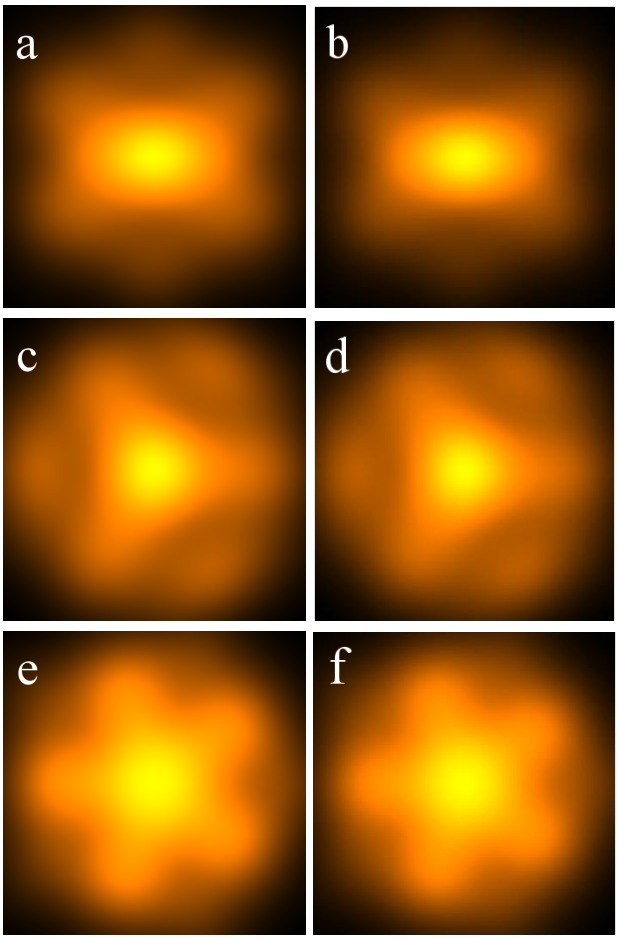

Figure 9.1: Theoretical scans of the repulsive interaction between two C_{60} molecules calculated from the change in kinetic energy (a,c,e), and the intermoleculare electronic overlap (b,d,f). The molecular orientations are as follows, where (a) and (b) show the case where both molecules have a 6-6 bond interacting, with the bonds on each molecule aligned, (c) and (d) show two hexagonal faces directly aligned, and (e) and (f) show two pentagonal faces aligned.

As can be seen from these images, while small differences do exist in the relative intensities at various parts of the images, the agreement between the two approaches is generally excellent.

While the images in figure 9.1 appear very similar, there is a large difference in computational time, with the overlap calculation reducing the time by over a factor of 10.

9.1.2 Orientational Dependence of the C_{60}-C_{60} Force Interaction

All of the work undertaken so far on modelling the force interaction has been in the context of applying it to AFM imaging. However, understanding the repulsive force has more general uses away from SPM, and it is this that shall now be considered. The C_{60}-C_{60} interaction shall still be investigated, although now, it is the way in which the repulsive force depends on the relative orientations of the two molecules that shall be considered.

9.1.2.1 Rotating One C_{60} in the xz Plane

It has been shown previously that at large distance, the attractive force can be accurately modelled using two interacting spheres through the Girifalco potential. Thus, as an approximation, the attractive force will be assumed constant for all molecular orientations. With this assumption, it is therefore intuitive that at a fixed separation, the orientations which have the least intermolecular electronic overlap, and hence a smaller $\eta(2)$ value, will result in a weaker repulsive force, and hence a lowest minimum energy value. This is because the minimum energy value relates to the point at which the attractive and repulsive forces exactly cancel each other (as the derivative at the minimum is zero, indicating no net force). Therefore, the molecular separation would need to decrease, resulting in a greater attractive force, and hence lower energy at the minimum.

In the data that follows, the two C_{60}s will be separated along the z axis, with one of the molecules fixed with either a 6-6 bond, 5-6 bond, atom, hexagonal face, or pentagonal face along the z axis. The second molecule is then rotated in the xz plane which rotates the molecule around a great circle passing through the line of the 6-6 bond, such that the interaction with a 6-6 bond, atom, pentagonal face, 5-6 bond, and hexagonal face prone molecule is considered. By applying the rotation up to π radians, the reflections of these cases are also considered.

Figure 9.2 shows a selection of plots for each of the fixed orientations, with the

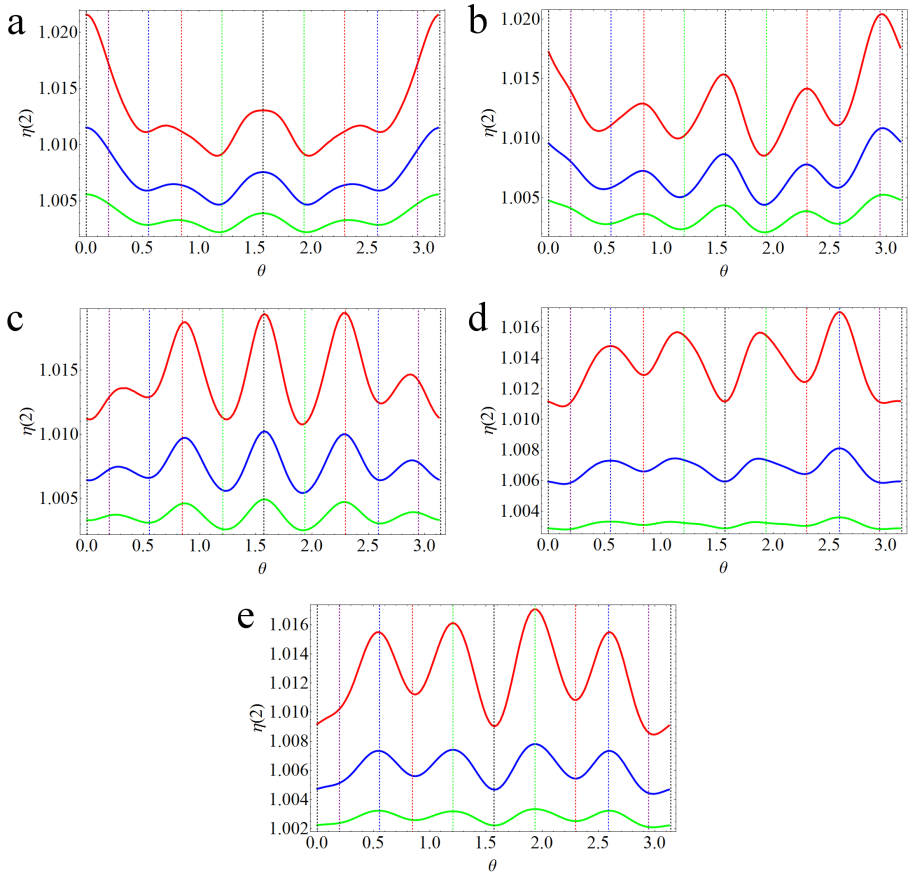

Figure 9.2: Theoretical plots of the intermolecular electronic overlap between two C_{60} molecules. The orientation of one molecule is varied through a rotation in the xz plane, represented by the angle θ. The orientation of the other molecule is with (a) a 6-6 bond, (b) an atom, (c) a 5-6 bond, (d) a pentagonal face, and (e) a hexagonal face along the z axis. The separation between molecular centres is 17.5a.u. (red), 18a.u. (blue) and 18.5a.u. (green). The dashed vertical lines represent certain orientations of the rotated molecule, with a 6-6 bond (black), atom (purple), pentagonal face (blue), 5-6 bond (red) and a hexagonal face (green) aligned with the z axis.

separation taken to be 17.5a.u. (shown in red), 18a.u. (blue) and 18.5a.u. (green) between the molecular centres. As can be seen, in each of the cases the minima and maxima of $\eta(2)$ with respect to the molecular orientation of the second C_{60} remains the same at each of the separations considered. That is to say that the position of the minimum and maximum intermolecular overlap is dependent entirely on the molecular orientation, and not on the separation between molecules.

From the data plotted in figure 9.2 the most and least energetically favourable orientations can be explored for when one of the molecules is fixed in position. Taking each case in turn, figure 9.2a shows the case where one of the C_{60}s is fixed with a 6-6 bond aligned along the z axis. It is found that the highest en-

ergy orientation of the second molecule is also with a 6-6 bond aligned along z, with a higher overlap (and hence a greater repulsive force, relating to a higher minimum energy point), found when the 6-6 bonds are aligned ($\theta = 0, \pi$), than when they are perpendicular to one another ($\theta = \pi/2$). The minimum overlap is found where the second C_{60} has a hexagonal face aligned along the z axis ($\theta \approx 1.21, 1.93$).

As would be expected, both of these results can be explained by considering the electron density associated with both molecules. As discussed, the electron density of C_{60} is greater around the 6-6 bonds than the 5-6 bonds, and hence, the fixed molecule has an area of high electron density interacting with the second molecule. When two 6-6 bonds are aligned, two areas of high electron density interact, and as such the overlap is increased, and the degree of orthogonalisation of the wavefunction is also increased. When the 6-6 bonds are perpendicular to one another, a strong interaction is still expected, as shown by the local maxima at $\theta = \pi/2$ (noting this is not necessarily a local maxima of the energy, merely a local maxima in the two dimensional space considered). However, the overlap will be decreased due to the misalignment of the atomic positions of each molecule. When a hexagonal face is aligned along z, the regions of high electron density are situated away from the axis, along the 6-6 bonds of the hexagon. Thus, there is a 'dip' in the electron density in the middle of the hexagon which accounts for the reduced overlap with the 6-6 bond, and hence the minima observed. It is for this reason that a local minima is observed when a pentagonal face is aligned along z ($\theta \approx 0.55, 2.60$). However, as the atomic positions are closer to the z axis than when a hexagonal face is present, a significant overlap is maintained, and the minima is not as deep. As expected for this data set, the results are symmetrical around $\theta = \pi/2$, due to the reflectional symmetry in the yz plane present in the molecule with a 6-6 bond fixed along the z axis.

The remaining sets of data in figure 9.2 can be explained using similar arguments relating to the electron density. In figure 9.2b, where the first molecule is fixed with an atom aligned along the z axis, the minimum is again found when a hexagonal face of the second molecule is aligned along z ($\theta = 1.93$). The

reason for this is again due to the dip in the electron density in the centre of the hexagon. However, unlike figure 9.2a, there is a difference in the overlap between the two different hexagonal face orientations (i.e. when $\theta \approx 1.21, 1.93$). These two different rotations have the effect of reflecting the hexagon in the yz plane, such that the positions of the 5-6 and 6-6 bonds within the hexagon are interchanged. The first molecule is oriented with an atom along the z axis, and has its 6-6 bond aligned along the x axis. At the minimum overlap point ($\theta \approx 1.93$), this 6-6 bond is aligned with a 5-6 bond of the second molecule. At the position corresponding to the slightly higher overlap ($\theta \approx 1.21$), the 6-6 bond of the atom prone molecule interacts with a 6-6 bond within the hexagon, resulting in a slightly greater intermolecular overlap. The maximum overlap in this case is found when both molecules have atomic positions along the z axis, and also have the 6-6 bonds associated with each aligned. This is found at the molecular orientation corresponding to $\theta \approx 2.95$.

Figure 9.2c shows the change in overlap when one C_{60} is fixed with a 5-6 bond along the z axis. The minimum overlap is again found when a hexagonal face of the second molecule is aligned along z ($\theta \approx 1.93$, which can again be explained by the low electron density in the central region of the hexagon. In considering the maximum overlap, there are three orientations that give similar overlaps. These are the two cases where the 5-6 bonds align with the z axis ($\theta \approx 0.85, 2.30$), and when the 6-6 bond is aligned in the z axis, with the two bonds in the same plane. The differences are small between the three, although the overlap obtained when $\theta \approx 2.30$ is slightly greater, corresponding to the case where the two 6-6 bonds adjacent to the 5-6 bond align. Interestingly, the overlap found when a 6-6 bond of one molecule is perpendicular to the 5-6 bond of the other molecule ($\theta = 0, \pi$) forms a local minima in the space considered. In this case there is only small overlap, as none of the atomic positions align, and the high density region associated with the 6-6 bond interacts with the low density region of the 5-6 bond.

Figures 9.2d and e, where a pentagonal (d) and hexagonal (e) face align along the z axis show very similar trends to one another. This is because both have a

region of low electron density in the middle of the face, meaning that minimal overlap will be observed when the second molecule is situated with a bond or atom aligned with z, and much greater when two faces interact. In both cases the minimum overlap is found when an atom is situated along the z axis. The explanation of the hexagon-atom interaction is the same as considered previously, as both molecules are identical, and as such are interchangeable, with the minimum overlap found when the 6-6 bond of the atom is oriented across a 5-6 bond of a hexagon. This also holds true when considering the interaction with the pentagonal face, although this corresponds to a different value of θ ($\theta \approx 0.19$) due to the different orientation of the fixed molecule. The maxima are in both cases found when the same face is aligned along the z axis. With the hexagonal face, the highest overlap is when the bonds of each molecule are aligned ($\theta \approx 1.93$), with the opposite case (where the 5-6 bonds align with the 6-6 bonds ($\theta \approx 1.21$)) giving less overlap. For the interacting pentagonal faces, the most overlap is when the pentagons mirror each other ($\theta \approx 2.60$), compared with when the atoms align with the bonds ($\theta \approx 0.55$).

With each case considered separately, the next step is to combine the data together for the different intermolecular separations, and it is this that is shown in the series of plots in figure 9.3. The plots shown are for an increasing distance between the molecular centres, with figure 9.3a having a separation of 17.5a.u., which increases in steps of 0.5a.u. up to figure 9.3f, which has a separation of 20a.u.. It can be seen that as this separation increases, some of the trends within the plots change, meaning it is difficult to elucidate a lot of the relative differences between the different orientations. However, the minimum and maximum overlap values *are* consistent as the distance between the molecules increases. The minimum overlap configuration is predicted to be with an atom of one molecule, and a hexagonal face of the other aligned along the z axis, which greatly reduces the overlap as discussed previously. The maximum overlap is found to be when two 6-6 bonds interact, such that the bonds are aligned, which again, was discussed previously.

The change in the trends as the separation increases is in part due to the structure

of C_{60}. The intermolecular separation is maintained constant for the different orientations in terms of the molecular centres. However, the separation between nearest interacting atoms will be different for differing orientations at constant distance between their centres. Each of the atoms within C_{60} are situated on a sphere, and as such the minimum distance between atoms on each molecule occurs when both have an atom aligned along the z axis. If, for example, two hexagonal faces were interacting, the distance between the hexagonal planes would be greater than this, and as such, the electronic wavefunction would have more time to decay (as it is formed from a LCAO associated with each atomic position). As well as this, the p orbitals which form the basis would point further away from the z axis, again increasing the decay rate in the z direction. This behaviour is what is seen in the plots in figure 9.3, where the relative overlaps relating to the 6-6, 5-6 and atom prone orientations remaining relatively similar, but those for the pentagon and hexagon prone orientations decreasing as the intermolecular separation increases.

With this is mind, care must be taken in interpreting the results obtained. A constant separation between the molecular centres was chosen due to the nature in which the Girifalco potential accurately predicts the attractive behaviour, which has its basis in two interacting spheres. However, it could well be that slight deviations from this occur at slightly shorter range (where the repulsive interaction is significant), which would give a degree of orientational dependence on the attractive interaction. However, the minimum and maximum *have* been consistently predicted for the different separations considered, and so it is highly likely this result is valid.

9.1.2.2 Rotating One C_{60} in the xy Plane

The orientations considered thus far only consider a small proportion of the parameter space, as only a single rotation has been considered. However, this rotation has considered all of the high symmetric orientations, which, given the symmetrical nature of the electron density associated with C_{60}, would be expected

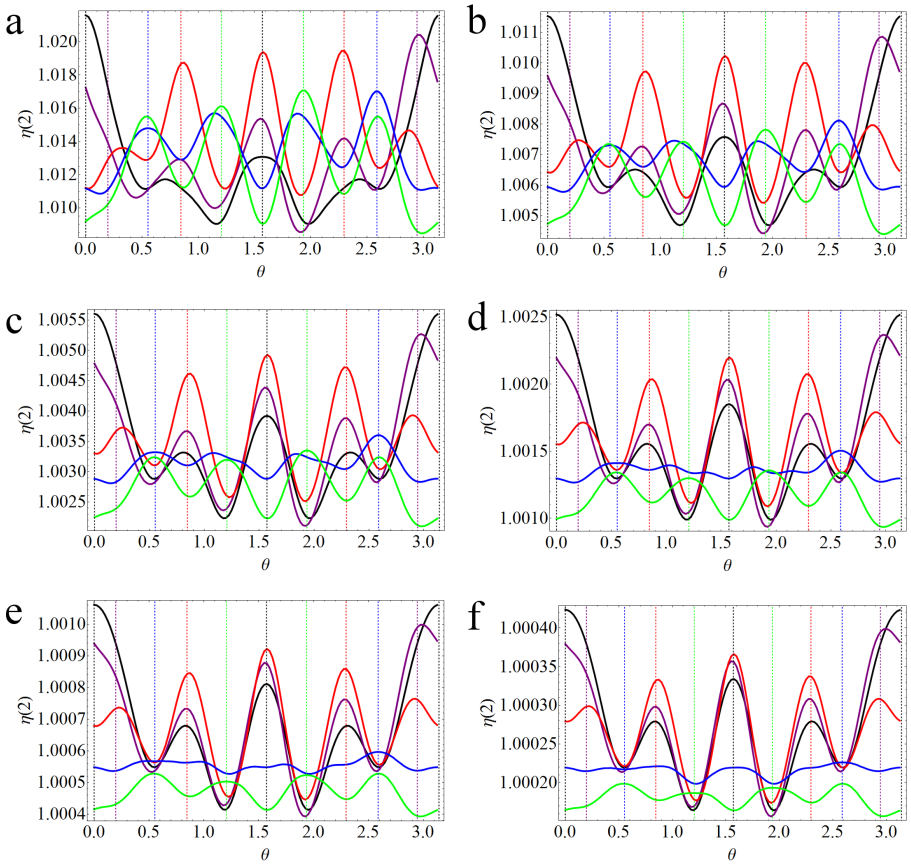

Figure 9.3: Theoretical plots of the intermolecular electronic overlap between two C_{60} molecules. The orientation of one molecule is varied through a rotation in the xz plane, represented by the angle θ. The orientation of the other molecules are shown is with a 6-6 bond (black), an atom (purple), a 5-6 bond (blue), a pentagonal face (red), and a hexagonal face (green) along the z axis. The dashed vertical lines represent certain orientations of the rotated molecule, with the same colours relating to the same molecular orientations. The intermolecular separations are (a) 17.5a.u. , (b) 18a.u. , (c) 18.5a.u. , (d) 19a.u. , (e) 19.5a.u. and (f) 20a.u.

to encompass the minimum and maximum overlaps. To extend the parameter space a little further, a rotation in the xy plane of one of the molecules will now be considered for a variety of relative molecular orientations.

Again, only the highly symmetric orientations will be considered, with both molecules having a fixed orientation along the z axis, before applying a rotation around this axis in the xy plane. A full 2π rotation will be considered to show any periodicity in the results, with the intermolecular separation fixed at 19a.u.. Not all symmetric orientations will be considered, as using a logical approach to consider the overlap, the results can be predicted in most cases. However, examples will be shown to illustrate these points, as well as looking at orientations which are perhaps less intuitive to predict.

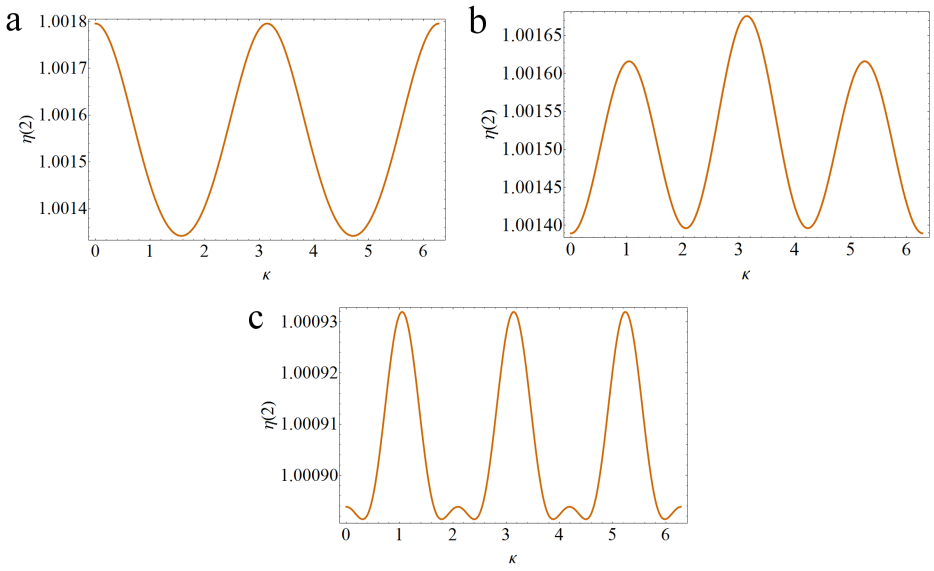

Figure 9.4: $\eta(2)$ calculated for two C_{60} molecules oriented with (a) a 6-6 bond of each molecule aligned along z, (b) an atom of each molecule aligned along z, and (c) a hexagonal face of each molecule aligned along z. One molecule is rotated in the xy plane through the angle κ.

Figure 9.4 shows three separate cases; where both molecules have a 6-6 bond along the z axis (a), where both have an atom along z (b), and where both have the centre of a hexagonal face along z (c). Each of these can be readily understood by considering the electron density as was considered previously. The simplest case shown is in figure 9.4a where two 6-6 bonds are aligned. The electron density is predominantly along the line of the bond, and as such, a maxima in the overlap is found when the bonds are aligned, shown where $\kappa = 0, \pi, 2\pi$. As the molecule rotates away from this orientation, the overlap reduces until the bonds are perpendicular to one another, resulting in the minimum overlap points at $\kappa = \pi/2, 3\pi/2$. The two fold rotational symmetry of the molecules around the z axis is observed in the π periodicity of the plot.

In figure 9.4b, both molecules are oriented with an atom aligned along the z axis. The crucial part of the structure in interpreting the overlap is the 6-6 bond associated with this atom in both cases. At $\kappa = 0$, the molecules are oriented with the 6-6 bonds pointing in opposite directions (such that each 6-6 bond aligns half way between the two 5-6 bonds of the other molecule), resulting in reduced overlap, and the minimum observed. As one of the molecules is rotated, a maximum is observed when the 6-6 bond aligns with a 5-6 bond of the other C_{60}. This

situation is represented by the peaks at $\kappa = \pi/3$ and $\kappa = 5\pi/3$. However, the maximum overlap is observed when the two 6-6 bonds align with one another at $\kappa = \pi$.

Where two hexagonal faces interact, (figure 9.4c), there is a clear three-fold periodicity, as would be expected due to the C_3 rotational symmetry associated with the hexagon. There are two distinct types of peak within this plot. The highest peaks, found at $\kappa = \pi/3, \pi, 5\pi/3$ represent the case where the 6-6 bonds of both molecules are aligned, giving the maximum possible overlap for this orientation. The second, much smaller, peak, occurs in the opposite case to this where the 6-6 bonds of the hexagonal face of one C_{60} align with the 5-6 bonds of the other (shown at $\kappa = 0, 2\pi/3, 4\pi/3$). Using the argument that the electron density is associated with the 6-6 bonds and not the 5-6 bonds, it would follow that this would actually be a *minimum* in the overlap. However, the electron density is not evenly distributed over the 5-6 bond, but is greater towards the atomic centres than in the middle of the bond. As such, deviating slightly away from these angles, and hence misaligning the atomic centres actually reduces the overlap slightly. It is for this reason that the minima occur just to the side of this smaller peak.

Using the arguments relating to the electron density it is straight forward to interpret what would be observed for other orientations. For example, if two pentagonal faces are aligned a five-fold periodicity would be expected due to the C_5 symmetry associated with the pentagonal face. A maximum would be expected when the atomic positions align, and a minimum when each atomic position aligns with the 5-6 bond on the other molecule. The result for this case is shown in figure 9.5, where it can be seen each of these trends are observed.

Using this logic is suitable in most cases to predict the trends accurately. However, in some cases, as was seen in figure 9.4c where two hexagonal faces are aligned, the results are not quite so intuitive to interpret. Figure 9.6 shows two cases where one of the C_{60}s has a 6-6 bond aligned along the z axis, with figure 9.6a showing the interaction with a pentagonal face, and figure 9.6b showing the interaction with a hexagonal face. In both cases the periodicity is double

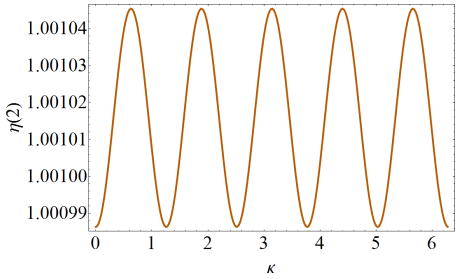

Figure 9.5: $\eta(2)$ calculated for the case where two C_{60}s are oriented with a pentagonal face aligned along the z axis, and one molecule is rotated in the xy plane through the angle κ.

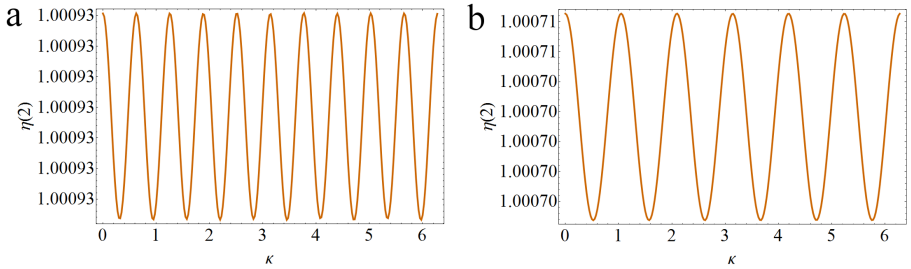

Figure 9.6: $\eta(2)$ calculated for the case where two C_{60}s are oriented with a 6-6 bond of one molecule along the z axis, and (a) a pentagonal face, and (b) a hexagonal face of the second molecule aligned along z. One molecule is rotated in the xy plane through the angle κ.

that, that may be expected, with figure 9.6a having a ten-fold periodicity, and figure 9.6b having a six-fold periodicity. This is brought about as on both the pentagonal and hexagonal faces, the areas of higher electron density (the atomic positions on the pentagon and the 6-6 bonds on the hexagon) are directly opposite the areas of lower electron density (the 5-6 bonds in both cases). As the 6-6 bond has C_2 symmetry, when one atomic centre of the bond aligns with an area of high electron density, the other centre aligns with an area of weak electron density, doubling the cases where the maximum overlap is observed.

As mentioned, the electron density associated with the 6-6 bonds is slightly localised towards the atomic centres and away from the middle of the bond. As such, it would seem intuitive that when interacting with a 6-6 bond as shown in figure 9.6 that the maxima would be observed at a slight deviation away from aligning the 6-6 bond along the z axis, with a 6-6 bond of the hexagon. However, the minimum distance between the atomic centre of the 6-6 bond aligned with the z axis, and the centre of the 6-6 bond on the hexagon is shorter than that with the atomic centre on the hexagon. This is sufficient to result in the greater overlap when aligned with the centre of the bond that is observed.

Even in these more complicated cases, using the general properties of the electron density provides enough information to determine the orientations corresponding to the high and low overlaps. This in turn implies the degree of orthogonalisation of the wavefunction, which, by extension, implies the relative strength of the repulsive force observed. Understanding the relative magnitudes of the repulsive force gives an indication as to the minimum energy orientations, and as such, a simple premise can be used to determine the relative energy favourability of certain orientations. Using the techniques shown as an investigative tool could then lead to more thorough investigation of these preferable orientations using more rigorous techniques such as DFT+vdW.

Chapter 10

Beyond C_{60}

The majority of the work thus far has looked at C_{60}, and STM and AFM images that may be obtained from systems associated with it. In this final chapter, EHMO theory will be used on two other molecules to show how the techniques developed here can be more widely applicable. Initially, pentacene will be considered, as a simple extension from C_{60}, where hydrogen is present within the molecule. A small amount of work will then be shown looking at how PTCDA may be modelled with EHMO theory.

10.1 Pentacene

Pentacene, $C_{22}H_{14}$, is a polycyclic hydrocarbon, consisting of five joined benzene rings, the atomic structure of which is shown in figure 10.1. It has played a crucial role in the recent advances in SPM, as shown by the striking AFM images obtained by Gross *et al.* [7] when imaged through a CO functionalised probe. In addition to this, STM studies have been carried out looking at the effect of different tip states on the experimental images [95].

To construct a theoretical model to investigate the images obtained for pentacene, the MOs need to be constructed. In order to incorporate the hydrogen atoms into the model, EHMO theory is utilised. STOs will be used to form the electronic basis, and the equations shown in appendix A used to evaluate the atomic over-

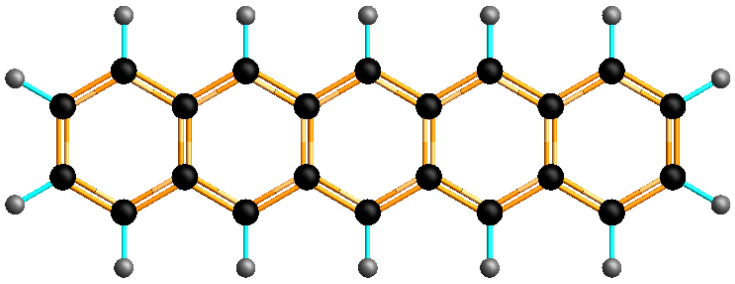

Figure 10.1: Ball & stick model of the pentacene molecule. The carbon atoms are shown in black, with the hydrogen atoms in grey.

laps. The diagonal elements of the Hamiltonian are taken in the same way as was used when modelling benzene where:

$$\begin{aligned} H_{ii}^{H_{1s}} &= -0.500\mathrm{E_h} \\ H_{ii}^{C_{2s}} &= -0.786\mathrm{E_h} \\ H_{ii}^{C_{2p}} &= -0.419\mathrm{E_h}, \end{aligned} \tag{10.1}$$

and the Wolfsberg-Helmholtz constant taken to be $K = 1.75$. As pentacene is described by the D_{2h} point group, only singlets are permitted in the MO levels. This means that the bonding interaction with the surface is not expected to have a significant effect on the form of the MOs, and as such it is not introduced here. To obtain the MOs it is therefore simply a case of diagonalising the extended Hückel Hamiltonian.

From the MOs, theoretical constant current STM images can be produced using the methods outlined earlier. Figure 10.2 shows the HOMO and the LUMO of pentacene alongside experimental images taken from the work by Gross *et al.* [28]. As expected, good agreement is found between theory and experiment in both cases.

In previous work by Gross *et al.* [28], STM images of pentacene were obtained using a carbon monoxide functionalised tip, with the interpretation given that the images were formed due to a combination of the interaction between the pentacene and p- and s- type tip states. However, in making this comparison, theoretical constant height images have been used as a comparison with experimental constant current images, leading to a possible misinterpretation of the results. If the correct comparison is made, it can be seen that the images can be

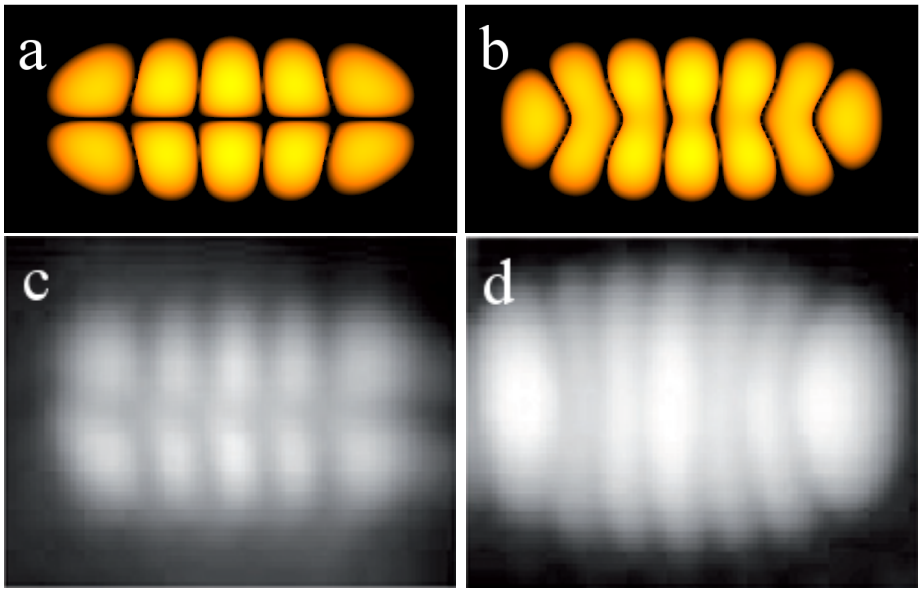

Figure 10.2: Comparison between experimental and theoretical STM images of the pentacene molecule. (a) and (b) show the theoretical images for the HOMO and LUMO of pentacene, and (c) and (d) show the corresponding experimental images obtained from Gross *et al.* [95].

reproduced by considering imaging within degenerate MOs of p character only.

Figure 10.3 shows the MOs of carbon monoxide determined using EHMO theory. The parameters associated with the carbon atom were taken to be the same as used throughout this work, while for oxygen, the Slater exponents were 2.245 and 2.225 for the $2s$ and $2p$ orbitals respectively, as predicted by Clementi and Raimondi [89]. The diagonal elements of the Hamiltonian were taken to be $-1.19\mathrm{E}_H$ for the $2s$ orbital and $-0.582\mathrm{E}_H$ for the $2p$ orbitals [90]. When imaging the HOMO of the pentacene molecule, it can be assumed that tunnelling is occurring from this level, into the LUMO of the CO molecule. Alternatively, when the LUMO of pentacene is imaged, it is the HOMO of CO from which the electrons tunnel.

The theoretical comparison proposed by Gross *et al.*[28] is shown in figure 10.4 alongside the theoretical constant current images obtained here. It can be seen from this, that these constant current images provide a better explanation of the experimental data than that proposed by Gross *et al.*. In both cases, the imaging has been formed by considering the tunnelling from the two-fold degenerate MO levels. The symmetry of the experimental STM images also shows that the CO

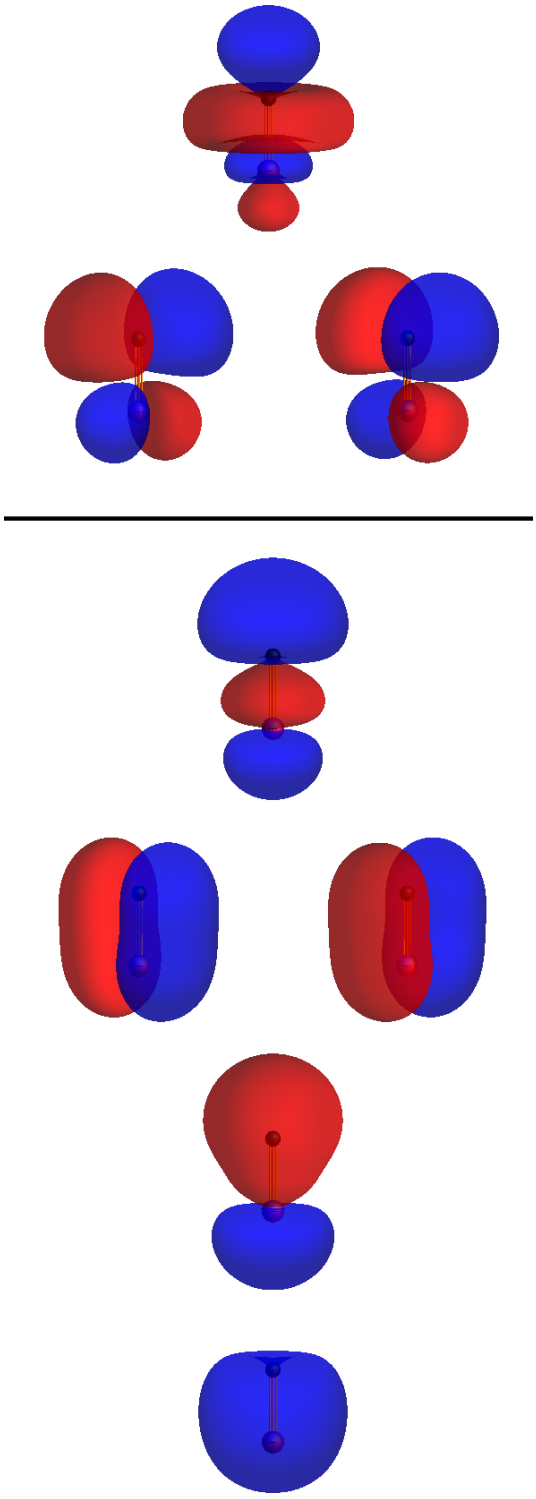

Figure 10.3: MOs of carbon monoxide, obtained through EHMO theory. Orbtials are ordered from highest energy to lowest, with the occupied orbitals below the black line.

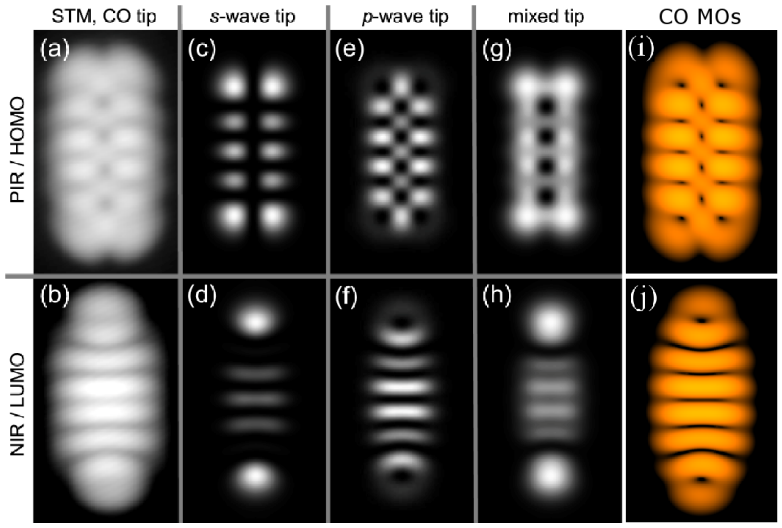

Figure 10.4: Experimental and theoretical STM images of pentacene for a selection of tip states. (a) and (b) show experimental constant current images of the HOMO and LUMO respectively. (c-h) show theoretical constant height simulations for (c-d) an s-type tip, (e-f) a p-type tip, and (g-h) a mixed s and p tip. (i) and (j) show theoretical constant current simulations using the methods shown here, and using the MOs of carbon monoxide as the tip. Images (a-h) obtained from Gross *et al.* [95]

molecule is adsorbed on to the tip pointing in the z direction (i.e. straight down from the tip). If this was not the case, and the CO was tilted at an angle, this would be seen in the STM images, where the image would be brighter on one side than the other.

When imaging the LUMO of pentacene, it would be expected that tunnelling would occur from the HOMO of the isolated CO molecule. However, the HOMO of CO only has contributions from the $2s$ and $2p_z$ atomic orbitals of oxygen. If the image was to be formed through tunnelling from this MO, the image obtained for a simple s type tip shown in figure 10.2 would be reproduced (noting that qualitatively, the images obtained from s and p_z orbitals are the same). As this does not accurately represent the experimentally determined image, the degenerate MOs below the HOMO can be considered. It is these MOs that give rise to the theoretical constant current image that provides a good match with experiment. That the tunnelling does not occur from the HOMO of isolated CO, but from the HOMO-1 could be down to the bias at which imaging occurs, or could be due to the bonding interaction between the CO and the probe that alters the energy level of the MOs. If a contribution from the HOMO was present, it would be required that it would contribute to less than 5% of the tunnelling current, so

as not to blur the image too much. However, the most clear match is found when tunnelling is considered solely from the HOMO-1 of the isolated molecule.

Where the HOMO of pentacene is imaged, it is found that if imaged at constant height, an identical image to that shown in figure 10.4e is produced from the CO MOs utilised here, where the outer edge of the image is faint. This is related to the exponential decay of the tunnelling current, meaning only a weak current is detected. At constant current, the measurement is of the tip height, and therefore changes linearly. As such, this outer region is much more pronounced in the constant current images obtained. Likewise, a constant height image of the LUMO produces the same image as figure 10.4f when the degenerate HOMO-1 is considered. In both cases, Gross *et al.* [28] argued that to accurately match the higher intensity at the edges of the image, an s type tip state is required. However, as shown here, this is not necessary, and in fact the contribution can be purely p type from the tip and obtain a suitable agreement. This shows the importance of using the correct theoretical technique to avoid misinterpretation of the experimental results.

Turning the attention to the AFM images of pentacene obtained with a CO functionalised tip, the techniques developed here can be used to construct a theoretical comparison with the experimental images. This is shown in figure 10.5 where the experimental image from ref. [7] is shown alongside a theoretical comparison, where it can be seen excellent agreement is found between the two. The bond structure is clearly depicted in both cases. However, it is interesting that the two ends of the pentacene molecule produce a stronger force interaction than the central part of the molecule. This can be explained if the electron density is considered as is shown in figure 10.5b. As discussed, it is intuitive that areas of high electron density will result in a stronger repulsion, and it can be seen that the electron density around the ends of the molecule is greater than in the centre.

This feature is easily understood by considering the diagonal elements of the extended Hückel Hamiltonian, which relates to the ionisation potential for each orbital. The greater magnitude of the ionisation potential of the $2s$ carbon orbital corresponding to that of the hydrogen orbital, suggests that the electronegativ-

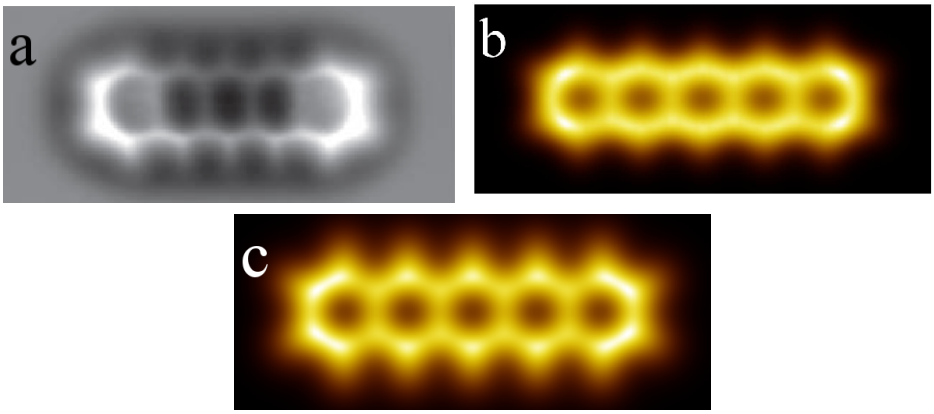

Figure 10.5: Force imaging of the pentacene molecule through a CO tip. (a) shows an experimentally derived image obtained from Gross *et al.* [7], (b) is electron density of the pentacene molecule obtained through EHMO theory, and (c) is the theoretical repulsive force interpretation when pentacene interacts with CO.

ity of the carbon atom is greater than that of the hydrogen. If the structure of pentacene is considered, each carbon at the ends of the molecule are bonded to a hydrogen, where as towards the middle of the molecule it is every alternate carbon atom that is bonded to hydrogen. The greater electronegativity of carbon compared to hydrogen, means that the carbon atoms bonded to hydrogen have a greater electron density than those that are only bonded to carbon. As such, the electron density of the pentacene molecule is concentrated towards the two ends where the carbon-hydrogen bonds are more prominent.

In constructing the repulsive force image in figure 10.5, the attractive vdW interaction has not been considered. There are two reasons for this. Firstly, an accurate interpretation of the result is obtained by only considering the repulsive force, and as such introducing the long range interaction would only serve to quantitatively match with experiment, and would not provide any new information. Secondly, the carbon oxygen bond in the CO molecule is expected to be polarised due to the difference in the electronegativities of the two elements. This means that there is a negative charge associated with the oxygen atom, and a positive charge associated with the carbon. When scanning over pentacene where, as discussed, a dipole exists within the carbon hydrogen bonds, an additional electromagnetic interaction would be expected, complicating the theoretical model. This interaction would be expected to increase the repulsive force between the CO and the carbon atoms bonded to hydrogen, which would further emphasise

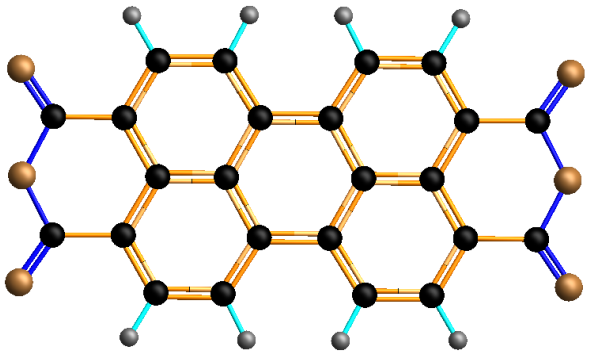

Figure 10.6: Ball & stick model of PTCDA. The carbon atoms are shown in black, the hydrogen atoms in grey, and the oxygen atoms in brown.

the features already discussed. Thus, the images formed can still be considered an accurate representation of what could be observed during AFM.

10.2 PTCDA

In the final part of the work a brief analysis of the PTCDA molecule will be undertaken, with EHMO theory utilised in the construction of theoretical AFM images. The atomic structure is shown in figure 10.6, showing that carbon, hydrogen and oxygen are all present within the molecule. The same extended Hückel parameters are used in constructing the Hamiltonian as have been used previously for hydrogen, carbon and oxygen, and again, an STO basis is utilised in constructing the MOs.

Using the MOs of CO obtained above, the repulsive force interaction can be modelled for when a CO functionalised tip is used in the imaging. The theoretical image obtained from this method is shown in figure 10.7 alongside an experimentally obtained image, and a theoretical interpretation based on the electron density taken from the work by Moll *et al.* [42]. Excellent agreement is found between the two theoretical images, with the highest force located around the upper and lower carbon atoms. Using the argument presented previously, it is these carbons that are expected to have the strongest interaction due to the difference in the electronegativity of these carbon atoms compared to the rest of the molecules. The same argument should also apply when considering the oxygen-

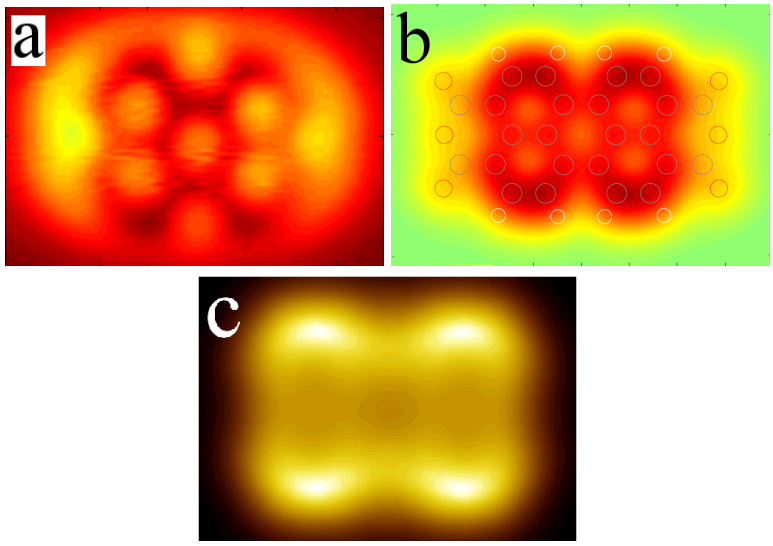

Figure 10.7: Comparison between the AFM images of PTCDA. (a) shows an experimentally derived image, and (b) a theoretical comparison, both from the work undertaken by Moll *et al.* [42]. (c) shows the theoretical repulsive force image produced using the techniques shown here.

hydrogen bonds, as the difference in the diagonal elements of the $1s$ hydrogen orbitals and the $2s$ oxygen orbital is even greater than that with the $2s$ carbon atoms. Indeed, if a scan is taken at lower tip height, it is these areas that have the greatest contribution. The larger Slater exponent associated with the oxygen atoms, means that the electrons are more localised than with the carbon atoms. Thus, at the tip height suggested by the experimental image, the electron density in the region around the oxygen atoms has already decayed significantly, and the contribution to the overall force is small.

There are definite differences between the theoretical images and the experimental image, with the areas around the two edges of the molecule appearing different to that suggested. This is because the model used (in both cases) only considers the repulsive Pauli interaction. Towards the two ends of the molecule, this repulsive force is weak, due to the decay of the orbitals associated with the oxygen atoms resulting in minimal intermolecular overlap with the CO molecule, and hence, the predominant interaction is the long range attraction. Using LJ potentials, this could be introduced using the methods shown here. However, as was the case with pentacene, PTCDA is expected to have various dipoles within the molecule associated with both the oxygen-hydrogen bonds, and the carbon-oxygen bonds. Thus, introducing LJ potentials would only be an approximation,

and, as the results can be explained without the theoretical image being constructed, only the repulsive force has been considered.

Chapter 11

Discussion and Conclusions

In this work, a number of theoretical techniques have been proposed to model a variety of SPM systems. Primarily, the focus has been on imaging the C_{60} molecule in both STM and AFM, when adsorbed on to a surface, as part of a functionalised probe, or both. Comparisons with experiment have been provided throughout to justify the methods and interpret the experimental data, with excellent agreement found. The emphasis has been placed on providing a simple and speedy computational technique to be used as an investigative tool to analyse the effects of certain parameters associated with the systems under consideration. It is envisaged that the methods presented here could in future be used in conjunction with the more rigorous, but more computationally expensive, density functional theory in the analysis of SPM, particularly in multivariate systems.

The thesis began with a basic overview of the subject area, and a brief discussion on the motivation behind the work. This was then followed by a more comprehensive analysis of the physics behind both STM and AFM, as well as introducing the concept of tip functionalisation, and a description of the Si(111)-(7x7) reconstruction. In doing so, an extensive review of the literature, describing a variety of uses and features associated with the various areas was provided.

In Chapter 3, a thorough description of the theoretical techniques used throughout the work was given, in a way to be generally applicable for a variety of systems. Bardeen's matrix element was introduced as a means to model the tun-

nelling current observed during STM, which was then subsequently extended, through the use of a Green's function, to reproduce the result obtained by Tersoff and Hamann [77], where the current is proportional to the square of the wavefunction when an s-type tip state is considered. The derivative rule, as proposed by Chen [78] was then derived using the same technique, to obtain relationships for the current when the tip is assumed to be of the form of a p or d atomic orbital. The way in which the Pauli repulsion between two states is modelled was then explained, with an expression for the change in kinetic energy derived for two arbitrary wavefunctions. HMO and EHMO theory were then introduced, and the assumptions associated with each discussed, along with their range of validity, before a brief discussion of the advantages and disadvantages of using different forms of atomic orbitals to construct an electronic basis set. Finally in this section, a general overview of some of the key group theoretical aspects was given, with the premise behind point groups and irreducible representations discussed, and the way in which these apply to the incorporation of an interaction between a molecule and a surface described.

In chapter 4 the techniques introduced in chapter 3 were put to use to model the STM images obtained from benzene. HMO and EHMO theory were both utilised in the construction of the MOs of the molecule to show the consistency between the methods, before theoretical STM images were constructed. In doing so, the techniques used in constructing the images was shown. Finally, a look at the comparison between the images obtained during constant current and constant average current (dSTM) was shown.

Chapter 5 introduced the imaging of the neutral C_{60} molecule, with the MOs constructed using both HMO and EHMO theory. The symmetry properties of C_{60} were then considered, and the degeneracies within the MO levels discussed. Two techniques were then used to incorporate the surface interaction, and the images obtained from this obtained for a variety of molecular orientations. The derivative rule was then used to see the impact of different tip states on the STM images obtained. The same techniques were then used to model the bonding interaction between the C_{60} and the probe, and the experimental images obtained when a

C_{60} functionalised tip interacts with the Si(111)-(7x7) surface were analysed and interpreted. Note, that our work describing the form of the functionalised tip has been published in *Physical Review Letters* [91].

The STM images obtained when a C_{60} functionalised tip interacts with a surface-adsorbed C_{60} was then considered in chapter 6. A comparison between a variety of experimental images was made with the theory, with emphasis placed on the high symmetry orientations where it was found that symmetry operations present in both molecular orientations were preserved in the resultant STM images. A comparison was then made between a selection of images obtained with the surface-adsorbed molecule present on a Si(111)-(7x7) surface and the images obtained theoretically. Using a structured technique where the orientation of the tip-adsorbed molecule was first resolved through inverse imaging with the silicon surface, it was found to be relatively straightforward to deduce the orientation of the surface-adsorbed molecule. In doing so, excellent agreement was found with the adsorption geometries postulated by Rurali *et al.* [62]. The bulk of this work has been published in *Physical Review B* [68].

Attention was then turned to modelling the AFM images that would be obtained when C_{60} is imaged within the repulsive regime. The theoretical technique outlined in chapter 3 were expanded to show how, for the interaction between two atomic orbitals, the change in kinetic energy is found to be proportional to both the interaction energy, and the observed force. Thus, using an LCAO technique to obtain the MOs allows simple construction of the kinetic energy change, which in turn relates qualitatively to the observed image. Images were constructed firstly, for the case where the C_{60} is imaged through a model s type hydrogen tip, before the effects of the tip state on the AFM images was investigated. Then, the C_{60}-C_{60} interaction was considered for a selection of molecule orientations. Again, emphasis is placed on the symmetry of the resultant images for certain orientations, and how these remain in the observed images. An attractive interaction was then introduced by considering the attractive r^{-6} relationship within the LJ potential, before the Girifalco potential was utilised in constructing theoretical AFM images for the C_{60}-C_{60} interaction. In chapter 8 a complete set of

SPM data for a single surface-adsorbed C_{60}, being imaged by a tip-adsorbed C_{60} is presented. With both the STM and AFM images obtained, interpreted using all of the theoretical techniques presented here.

In chapter 9, HMO theory was utilised to look at the orientational dependence of the repulsive interaction between two C_{60}s. The relationship between the repulsive force and the degree of orthogonalisation was investigated through the intermolecular electronic overlap, with the result that both give qualitatively similar result. On the assumption that the attractive interaction is independent of the molecular orientation, the change in the orthogonalisation parameter $\eta(2)$ was investigated to obtain the orientations that have the minimum and maximum overlap, and hence by extension, the lowest and highest energy configurations. The minimum was found when an atom of one molecule faces a hexagonal face of the other, while the maximum was found when two 6-6 bonds interact.

Finally, in chapter 10, molecules other than C_{60} were considered, with the STM and AFM images of pentacene and PTCDA considered when imaged through a CO functionalised tip. EHMO theory was utilised to obtain the MOs of all three molecules, with this information then used in the construction of the images. Comparison with experiment and previous theory was then given, with excellent agreement. In the case of pentacene, use of the MOs of CO directly in determining the images results in an alternative interpretation of the STM data to that suggested by Gross *et al.* [28].

One of the central features of the work is the ability to determine molecular orientation of tip-adsorbed and sample-adsorbed molecules. Techniques have been shown that not only allow this to be obtained for the individual molecules, but also simultaneously, through the deconvolution of STM and AFM images. This could be of great benefit when investigating any orientationally dependant properties, as obtaining this from a single image greatly increases the confidence in the molecular orientations prior to any further sampling. One such example could be in relation to the orientational dependence of the force interaction between the two molecules. In this case, it would be straightforward to use the inverse imaging from the surface to ascertain the orientation of the tip-adsorbed

C_{60}, then scanning over the surface-adsorbed C_{60} in STM immediately prior to obtaining a force spectra, to elucidate the sample C_{60} orientation.

The work has also aimed to understand the underlying physics behind the various forms of imaging, with preference given to an understanding of how an image is formed, rather than having a quantitatively accurate result. Using more rigorous computational methods it is often the case that although a result is accurately predicted, the reason behind that result being found is lost in the computational construct. It is for this reason that the simple techniques proposed here may act as an excellent starting point for more rigorous calculations, while still contributing to the physical understanding of the systems under consideration.

All of the theoretical data presented here has been done so with the intention of keeping the computational expense to a minimum. For the most computationally intensive calculation considered here (the repulsive interaction between two C_{60} molecules), investigative, low resolution, images can still be obtained within around 30 minutes on a standard desktop computer. For STM images of the C_{60}-C_{60} interaction, the time is no more than a few minutes for each image. Clearly, as readily available computational power increases, the construction of these type of images will become trivial, and could provide an excellent way to quickly investigate a system, both as an analytical tool in itself, and also as a way to streamline any more rigorous calculations such as those undertaken by DFT.

In order to reduce computational expense, the electronic basis was kept as simple as possible, by using a single ζ basis set, with both the values of ζ, and the diagonal elements of the Hamiltonian taken with values from the literature. However, techniques exist that allow both of these to be optimised for a particular molecule, via the Fenske-Hall method for the diagonal elements, and self-consistent EHMO theory, which treats the values of ζ as variables to be minimised. These have not been considered here, as the emphasis has always been on providing as simple a method as possible, although, in this way, double and triple zeta basis sets can be used, which may aid in achieving more quantitatively accurate results.

The force interaction presented here does not consider the effects of bond polarisation, with the repulsive regime modelled purely from the Pauli repulsion, and the attractive regime modelled empirically through atomic LJ potentials. However, where polarised molecules interact an additional Coulomb force will be observed that could alter the image. This is particular relevant when considering the CO functionalised tip considered in chapter 10, and utilised by Gross and coworkers. The difference in electronegativity between the oxygen and the carbon atoms that form the CO molecule means that the molecule is polarised, leading to a slight negative charge associated with the oxygen atom. When imaging other molecules with polarised bonds (as was considered here both with pentacene and PTCDA, which have polarised bonds), an additional force would be expected. Using the techniques here this should be quantifiable using a technique such as Mulliken analysis, where the relative charge associated with each atomic centre can be found from the MOs. This would in turn imply the polarisation of the bonds, and so allow the induced Coulomb interaction to modelled.

The techniques presented here relating to the force interaction, could in principle be extended to look at intermolecular interactions of molecules. With respect to C_{60}, a vast array of work has been published showing highly structure monolayers on a variety of surfaces (see for example refs. [99, 100, 5], amongst many others), as well as numerous works on C_{60} clusters (see refs. [101, 102]). It has been shown that the Girifalco potential [97] accurately determines the long range attractive vdW interaction [91], so a possible next step would be to combine this empirically determined relationship with the repulsive interaction calculated here, to fully describe the C_{60}-C_{60} interaction. This could then lead to the determination of preferential orientations of the two molecules, which may shed light on the structures observed.

Intriguing orientations have also been observed for the charged states of C_{60} [69], in particular for monolayers of K_4C_{60}, which display a pinwheel structure [70]. However, to understand the charged ions of C_{60} it is necessary to incorporate the symmetry reduction induced by the Jahn-Teller effect in to the theoretical model. Theoretical STM images have been constructed for the monoanion [67] while the

impact of the Jahn-Teller effect on multi-electron states has been considered for the higher charged fullerenes [103], such that theoretical STM images could be calculated for these ions. As such, the theoretical framework is in place to extend the interaction to the charged ions, to help explain the observed structures.

The effect the tip state has on the AFM images was discussed in detail in chapter 7. However, little work has been done on investigating the effect of the different tip states in STM, with respect to finding the optimum tip for detailed imaging. In order to investigate this, a move away from the proportionality relationships suggested by Tersoff and Hamann [77] and Chen [104] would need to be made, and more attention given to the construction of the multi-electron system. Relating the tip structure to the work done here, it is clear that the general proportionality relationships must remain. However, what could change is the proportionality constant which is relating to the density of states of both tip and sample. This proportionality constant could alter the current observed at a given bias, and hence allow a more detailed image to be obtained.

In considering the intermolecular overlap as a model for the repulsive interaction (chapter 9) the attractive interaction was considered as a function of the intermolecular separation, and independent of the molecular orientation. At increasing separation, the approximation that the two C_{60} be modelled by hard spheres is increasingly accurate. However, at the the shorter distances considered when the minimum energy point is considered, the model may need modification. This could be done as shown earlier in the work, where an attractive LJ potential is assigned to each of the atomic centres within the molecule. Then, rather than considering the data at constant height, a constant attractive force could be used, with the intermolecular separation altered at each point to maintain a fixed attractive force.

Appendices

Appendix A

Analytical Expressions for the Integration of STOs

In numerous sections throughout the work, it is required that analytical forms of a number of integrals associated with STOs are known. For this work, only those integrals associated with the overlap, and kinetic energy change of the $1s$, $2s$, and $2p_x, 2p_y$ and $2p_z$ orbitals are required, all of which are presented in the work by Roothaan [84]. However, the coordinate system used in this case differs from that used here, and as such the expressions need a small modification. For two atoms situated at the origin of two coordinate systems defined by $\{x, y, z\}$ and $\{x', y', z'\}$, with the z' axis defined to align with the atomic separation, the expressions by Roothaan are defined with the x and y axes parallel with the x' and y' axes but with the z axis pointing directly at the z' axis such that z aligns with $-z'$. In the work considered here, we require that z aligns with z'. This has no effect on the expressions that do not involve p orbitals, as the s-type orbitals are symmetrical with respect to a reflection in the xy plane. However, when a p orbital aligned with the z axis is considered, a change in sign of the expression is required as the orbital is antisymmetric with respect to the same reflection.

The full set of expressions is given below for both the overlap integrals and the kinetic energy integrals. The expressions involving only $1s$ and $2s$ orbitals are straightforward to use as the radial decay means there is no significance attached

to the z axis, and all that is required is the two slater exponents and the distance between the two atoms. However, for p orbitals, it is necessary to correctly align the z and z' axes. To do this, a unit vector is taken in the direction in which the p orbital points, and two rotations then applied to correctly align the axes. The resultant orbital will have p_x, p_y and p_z components. When the interaction is between a p orbital and either s orbital, the integral with both the p_x, and p_y components will be zero, and as such, all that is required is the z part of the rotated unit vector, which is used as a multiplicative constant over the final integral. Where the interaction is between two p orbitals, a unit vector is attached to both orbitals and the same rotation applied to align the axes. Due to the orthogonality of the states, each p orbital will only have a non-zero integral when interacting with the same form of orbital (i.e. p_x-p_x etc.). Two separate forms of the integral are required, with the interaction between two p_z orbitals (in the coordinate system as defined) treated differently to the p_x-p_x and p_y-p_y interaction.

In simplifying the expressions, six constants are defined:

$$\begin{aligned}
\zeta &= \frac{1}{2}\left(\zeta_a + \zeta_b\right) \\
\tau &= \frac{\zeta_a - \zeta_b}{\zeta_a + \zeta_b} \\
\rho &= \frac{1}{2}\left(\zeta_a + \zeta_b\right) R \\
\kappa &= \frac{\zeta_a^2 + \zeta_b^2}{\zeta_a^2 - \zeta_b^2} \\
\rho_a &= \zeta_a R \\
\rho_b &= \zeta_b R,
\end{aligned} \tag{A.1}$$

where ζ_a and ζ_b are the Slater exponents of the first and second atom respectively, and R is the interatomic separation. The final expressions are divided into two sections, where $\tau = 0$ (i.e. when the Slater exponents are equal) and where $\tau \neq 0$. In addition to the overlap integrals associated with the $1s, 2s$ and $2p$ states, additional integrals are given for the non-physical $0s$ and $1p$ overlaps (obtained in the usual way for an STO, using quantum numbers $n = 0, l = 0$, and $n = 1, l = 1$ respectively), as these expressions play a part in the kinetic energy expressions. It should also be noted that atomic units are used throughout.

A.1 Overlap Integrals

The integrals for the overlap integrals are shown below, firstly for the cases where $\tau = 0$, and then for when $\tau \neq 0$. A number of these expressions are identical to those published by Roothaan [84]. However, due to the difference in coordinate systems some of the expressions differ, and so for completeness all the necessary expressions are shown.

A.1.1 Equal Slater Exponent

$$
\begin{aligned}
\langle 0s|1s\rangle &= \frac{1}{\sqrt{2}}\left(1+\rho\right)e^{-\rho} \\
\langle 1s|1s\rangle &= \left(1+\rho+\frac{1}{3}\rho^2\right)e^{-\rho} \\
\langle 1p|1s\rangle &= \frac{1}{\sqrt{3}}\rho\left(1+\rho\right)e^{-\rho} \\
\langle 0s|2s\rangle &= \frac{1}{\sqrt{6}}\left(1+\rho+\frac{2}{3}\rho^2\right)e^{-\rho} \\
\langle 1s|2s\rangle &= \frac{\sqrt{3}}{2}\left(1+\rho+\frac{4}{9}\rho^2+\frac{1}{9}\rho^3\right)e^{-\rho} \\
\langle 1p|2s\rangle &= \frac{1}{6}\rho\left(1+\rho+\rho^2\right)e^{-\rho} \\
\langle 2s|2s\rangle &= \left(1+\rho+\frac{4}{9}\rho^2+\frac{1}{9}\rho^3+\frac{1}{45}\rho^4\right)e^{-\rho} \\
\langle 0s|2p\rangle &= -\frac{\sqrt{2}}{3}\rho\left(1+\rho\right)e^{-\rho} \\
\langle 1s|2p\rangle &= -\frac{1}{2}\rho\left(1+\rho+\frac{1}{3}\rho^2\right)e^{-\rho} \\
\langle 1p_{x,y}|2p_{x,y}\rangle &= -\frac{\sqrt{3}}{2}\left(-1-\rho+\frac{1}{3}\rho^3\right)e^{-\rho} \\
\langle 1p_z|2p_z\rangle &= \frac{\sqrt{3}}{2}\left(1+\rho+\frac{1}{3}\rho^2\right)e^{-\rho} \\
\langle 2s|2p\rangle &= -\frac{1}{2\sqrt{3}}\rho\left(1+\rho+\frac{7}{15}\rho^2+\frac{2}{15}\rho^3\right)e^{-\rho} \\
\langle 2p_{x,y}|2p_{x,y}\rangle &= \left(1+\rho+\frac{1}{5}\rho^2-\frac{2}{15}\rho^3-\frac{1}{15}\rho^4\right)e^{-\rho} \\
\langle 2p_z|2p_z\rangle &= \left(1+\rho+\frac{2}{5}\rho^2+\frac{1}{15}\rho^3\right)e^{-\rho}
\end{aligned}
\tag{A.2}
$$

A.1.2 Unequal Slater Exponent

$$\langle 0s|1s\rangle = \frac{\sqrt{1-\tau^2}}{\sqrt{2}\tau\rho}\left(-(1-\kappa)\,e^{-\rho_a} + ((1-\kappa)+\rho_b)\,e^{-\rho_b}\right)$$

$$\langle 1s|1s\rangle = \frac{\sqrt{1-\tau^2}}{\tau\rho}\Big(-(1-\kappa)\,(2\,(1+\kappa)+\rho_a)\,e^{-\rho_a} + (1+\kappa)\,(2\,(1-\kappa)+\rho_b)\,e^{-\rho_b}\Big)$$

$$\langle 1p|1s\rangle = \sqrt{\frac{1-\tau}{1+\tau}}\frac{1}{\sqrt{3}\tau\rho^2}\Big(-(1-\kappa)\left(2\,(1+\kappa)\,(1+\rho_a)+\rho_a^2\right)e^{-\rho_a} + (1+\kappa)\left(2\,(1-\kappa)\,(1+\rho_b)+\rho_b^2\right)e^{-\rho_b}\Big)$$

$$\langle 0s|2s\rangle = \frac{\sqrt{1-\tau^2}}{\sqrt{6}\tau\rho}\Big(-(1-\kappa)\,(1-2\kappa)\,e^{-\rho_a} + \left((1-\kappa)\,(1-2\kappa)+2\,(1-\kappa)\,\rho_b+\rho_b^2\right)e^{-\rho_b}\Big)$$

$$\langle 1s|2s\rangle = \frac{\sqrt{1-\tau^2}}{\sqrt{3}\tau\rho}\Big(-(1-\kappa)\,(2\,(1+\kappa)\,(2-3\kappa)+(1-2\kappa)\,\rho_a)\,e^{-\rho_a} + (1+\kappa)\left(2\,(1-\kappa)\,(2-3\kappa)+4\,(1-\kappa)\,\rho_b+\rho_b^2\right)e^{-\rho_b}\Big)$$

$$\langle 1p|2s\rangle = \sqrt{\frac{1-\tau}{1+\tau}}\frac{1}{\tau\rho^2}\Big(-(1-\kappa)\,(2\,(1+\kappa)\,(2-3\kappa)\,(1+\rho_a) + (1-2\kappa)\,\rho_a^2)e^{-\rho_a} + (1+\kappa)\,(2\,(1-\kappa)\,(2-3\kappa)\,(1+\rho_b) + (3-4\kappa)\,\rho_b^2+\rho_b^3)e^{-\rho_b}\Big)$$

$$\langle 2s|2s\rangle = \frac{\sqrt{1-\tau^2}}{3\tau\rho}\Big(-(1-\kappa)\,(2\,(1+\kappa)\left(7-12\kappa^2\right) + 4\,(1+\kappa)\,(2-3\kappa)\,\rho_a+(1-2\kappa)\,\rho_a^2)e^{-\rho_a} + (1+\kappa)\,(2\,(1-\kappa)\left(7-12\kappa^2\right)+4\,(1-\kappa)\,(2+3\kappa)\,\rho_b + (1+2\kappa)\,\rho_b^2)e^{-\rho_b}\Big)$$

$$\langle 0s|2p\rangle = -\sqrt{\frac{1+\tau}{1-\tau}}\frac{1}{\sqrt{2}\tau\rho^2}\Big(-2\left(1-\kappa^2\right)(1+\rho_a)\,e^{-\rho_a} + \left(2\left(1-\kappa^2\right)(1+\rho_b)+2\,(1-\kappa)\,\rho_b^2+\rho_b^3\right)e^{-\rho_b}\Big)$$

$$\langle 1s|2p\rangle = -\sqrt{\frac{1+\tau}{1-\tau}}\frac{1}{\tau\rho^2}\Big(-(1-\kappa)^2\left(6\,(1+\kappa)\,(1+\rho_a)+2\rho_a^2\right)e^{-\rho_a} + (1+\kappa)\left(6\,(1-\kappa)^2\,(1+\rho_b)+4\,(1-\kappa)\,\rho_b^2+\rho_b^3\right)e^{-\rho_b}\Big)$$

$$
\begin{aligned}
\langle 1p_{x,y}|2p_{x,y}\rangle =& -\frac{\sqrt{3}}{\sqrt{1-\tau^2}\tau\rho^3}\Bigg(-(1-\kappa)^2\left(12(1+\kappa)\left(1+\rho_a+\frac{1}{2}\rho_a^2\right)\right.\\
&\left.+2\rho_a^3\right)e^{-\rho_a}+(1+\kappa)\left(12(1-\kappa)\left(1+\rho_b+\frac{1}{2}\rho_b^2\right)\right.\\
&\left.+(3-4\kappa)\rho_b^3+\rho_b^4\right)e^{-\rho_b}\Bigg)\\
\langle 1p_z|2p_z\rangle =& \frac{\sqrt{3}}{\sqrt{1-\tau^2}\tau\rho^3}\Big(-(1-\kappa)^2\left(6(1+\kappa)(1+\rho_a)+2\rho_a^2\right)e^{-\rho_a}\\
&+(1+\kappa)\left(6(1-\kappa)^2(1+\rho_b)+4(1-\kappa)\rho_b^2+\rho_b^3\right)e^{-\rho_b}\Big)\\
\langle 2s|2p\rangle =& -\sqrt{\frac{1+\tau}{1-\tau}}\frac{1}{\sqrt{3}\tau\rho^2}\Big(-(1-\kappa)^2\left(6(1+\kappa)(3+4\kappa)(1+\rho_a)\right.\\
&\left.+2(5+6\kappa)\rho_a^2+2\rho_a^3\right)e^{-\rho_a}+(1+\kappa)\left(6(1-\kappa)^2(3+4\kappa)(1\right.\\
&\left.+\rho_b)+4(1-\kappa)(2+3\kappa)\rho_b^2+(1+2\kappa)\rho_b^3\right)e^{-\rho_b}\Big)\\
\langle 2p_{x,y}|2p_{x,y}\rangle =& -\frac{1}{\sqrt{1-\tau^2}\tau\rho^3}\Big(-(1-\kappa)^2\left(48(1+\kappa)^2\left(1+\rho_a+\frac{1}{2}\rho_a^2\right)\right.\\
&\left.+2(5+6\kappa)\rho_a^3+2\rho_a^4\right)e^{-\rho_a}+(1+\kappa)^2\left(48(1-\kappa)^2\left(1+\rho_b\right.\right.\\
&\left.\left.+\frac{1}{2}\rho_b^2\right)+2(5-6\kappa)\rho_b^3+2\rho_b^4\right)e^{-\rho_b}\Big)\\
\langle 2p_z|2p_z\rangle =& \frac{1}{\sqrt{1-\tau^2}\tau\rho^3}\Big(-(1-\kappa)^2\left(24(1+\kappa)^2(1+\rho_a)+12(1+\kappa)\rho_a^2\right.\\
&\left.+2\rho_a^3\right)e^{-\rho_a}+(1+\kappa)^2\left(24(1-\kappa)^2(1+\rho_b)+12(1-\kappa)\rho_b^2\right.\\
&\left.+2\rho_b^3\right)e^{-\rho_b}\Big)
\end{aligned}
\tag{A.3}
$$

A.2 Kinetic Energy Integrals

The second set of integrals required are the kinetic energy integrals. These are given as functions of the overlap integrals shown previously, although these do not require different forms depending on the value of τ.

$$
\begin{aligned}
-\frac{1}{2}\langle 1s|\nabla^2|1s\rangle &= -\frac{1}{2}\zeta^2\left(1+\tau\right)^2\left(\langle 1s|1s\rangle - 2\sqrt{2}\,\langle 0s|1s\rangle\right)\\
-\frac{1}{2}\langle 1s|\nabla^2|2s\rangle &= -\frac{1}{2}\zeta^2\left(1+\tau\right)^2\left(\langle 1s|2s\rangle - 2\sqrt{2}\,\langle 0s|2s\rangle\right)\\
-\frac{1}{2}\langle 2s|\nabla^2|2s\rangle &= -\frac{1}{2}\zeta^2\left(1+\tau\right)^2\left(\langle 2s|2s\rangle - \frac{4}{\sqrt{3}}\langle 1s|2s\rangle + \frac{2\sqrt{2}}{\sqrt{3}}\langle 0s|2s\rangle\right)\\
-\frac{1}{2}\langle 1s|\nabla^2|2p\rangle &= -\frac{1}{2}\zeta^2\left(1+\tau\right)^2\left(\langle 1s|2p\rangle - 2\sqrt{2}\,\langle 0s|2p\rangle\right)\\
-\frac{1}{2}\langle 2s|\nabla^2|2p\rangle &= -\frac{1}{2}\zeta^2\left(1+\tau\right)^2\left(\langle 2s|2p\rangle - \frac{4}{\sqrt{3}}\langle 1s|2p\rangle + \frac{2\sqrt{2}}{\sqrt{3}}\langle 0s|2p\rangle\right)\\
-\frac{1}{2}\langle 2p_{x,y}|\nabla^2|2p_{x,y}\rangle &= -\frac{1}{2}\zeta^2\left(1+\tau\right)^2\left(\langle 2p_{x,y}|2p_{x,y}\rangle - \frac{4}{\sqrt{3}}\langle 1p_{x,y}|2p_{x,y}\rangle\right)\\
-\frac{1}{2}\langle 2p_z|\nabla^2|2p_z\rangle &= -\frac{1}{2}\zeta^2\left(1+\tau\right)^2\left(\langle 2p_z|2p_z\rangle - \frac{4}{\sqrt{3}}\langle 1p_z|2p_z\rangle\right) \qquad \text{(A.4)}
\end{aligned}
$$

Appendix B

Character Tables

Within certain sections of this work it is necessary to use the character tables associated with particular point groups. For reference, the relevant character tables are listed below, with the symmetry operations forming the columns, and the different irreps forming the rows. Here, ϕ is the golden ratio, defined as $\phi = \frac{1}{2}\left(1+\sqrt{5}\right)$

Table B.1: Character table for the I_h point group

I_h	I	$12C_5$	$12(C_5)^2$	$20C_3$	$15C_2$	i	$12S_{10}$	$12(S_{10})^3$	$20S_6$	15σ
A_g	1	1	1	1	1	1	1	1	1	1
$T1_g$	3	ϕ	$-\phi^{-1}$	0	-1	3	$-\phi^{-1}$	ϕ	0	-1
$T2_g$	3	$-\phi^{-1}$	ϕ	0	-1	3	ϕ	$-\phi^{-1}$	0	-1
G_g	4	-1	-1	1	0	4	-1	-1	1	0
H_g	5	0	0	-1	1	5	0	0	-1	1
A_u	1	1	1	1	1	-1	-1	-1	-1	-1
$T1_u$	3	ϕ	$-\phi^{-1}$	0	-1	-3	ϕ^{-1}	$-\phi$	0	1
$T2_u$	3	$-\phi^{-1}$	ϕ	0	-1	-3	$-\phi$	ϕ^{-1}	0	1
G_u	4	-1	-1	1	0	-4	1	1	-1	0
H_u	5	0	0	-1	1	-5	0	0	1	-1

Table B.2: Character table for the C_{5v} point group

C_{5v}	I	$2C_5$	$2(C_5)^2$	$5\sigma_v$
A_1	1	1	1	1
A_2	1	1	1	-1
E_1	2	ϕ^{-1}	$-\phi$	0
E_2	2	$-\phi$	ϕ^{-1}	0

Table B.3: Character table for the C_{3v} point group

C_{3v}	I	$2C_3$	$3\sigma_v$
A_1	1	1	1
A_2	1	1	-1
E	2	-1	0

Table B.4: Character table for the C_{2v} point group

C_{2v}	I	C_2(z)	σ_v(xz)	$5\sigma_v$(yz)
A_1	1	1	1	1
A_2	1	1	-1	-1
B_1	1	-1	1	-1
B_2	1	-1	-1	1

Table B.5: Character table for the C_s point group

C_s	I	σ_h
A’	1	1
A”	1	-1

Table B.6: Character table for the C_1 point group

C_1	I
A	1

Bibliography

[1] D. M. Eigler and E. K. Schweizer, Nature **344**, 524 (1990).

[2] D. M. Eigler, C. P. Lutz, and W. E. Rudge, Nature **352**, 600 (1991).

[3] G. Binnig and H. Rohrer, Surface Science **126**, 236 (1983).

[4] G. Binnig, C. F. Quate, and C. Gerber, Phys. Rev. Lett. **56**, 930 (1986).

[5] C. Chen, *Introduction to scanning tunneling microscopy* (Oxford University Press, 2008).

[6] C. Bai, *Scanning Tunneling Microscopy and Its Application* (Springer, 2000).

[7] L. Gross, F. Mohn, N. Moll, P. Liljeroth, and G. Meyer, Science **325**, 1110 (2009).

[8] G. Binnig, H. Rohrer, C. Gerber, and E. Weibel, Phys. Rev. Lett. **50**, 120 (1983).

[9] T. Vorburger *et al.*, CIRP Annals-Manufacturing Technology **46**, 597 (1997).

[10] R. K. Prasad, *Quantum Chemistry*, 3rd ed. (New Age International, 2006).

[11] W. Haberle, J. K. H. Horber, F. Ohnesorge, D. P. E. Smith, and G. Binnig, Ultramicroscopy **42**, 1161 (1992).

[12] H. W. Kroto, J. R. Heath, S. C. O'Brien, R. F. Curl, and R. E. Smalley, Nature **318**, 162 (1985).

[13] L. Gross *et al.*, Science **337**, 1326 (2012).

[14] P. Jacobs, *Group Theory with Applications in Chemical Physics* (Cambridge University Press, 2005).

[15] S. C. Erwin and M. R. Pederson, Phys. Rev. B **47**, 14657 (1993).

[16] K. Tanigaki *et al.*, Nature **352**, 222 (1991).

[17] A. Karton, B. Chan, K. Raghavachari, and L. Radom, J. Phys. Chem. A **117**, 1834 (2013).

[18] Y. Chai *et al.*, J. Phys. Chem. **95**, 7564 (1991).

[19] M. Arndt *et al.*, Nature **401**, 680 (1999).

[20] Y. Zhao, Y.-H. Kim, A. C. Dillon, M. J. Heben, and S. B. Zhang, Phys. Rev. Lett. **94**, 155504 (2005).

[21] R. Bakry *et al.*, International Journal of Nanomedicine **2**, 639 (2007).

[22] H. Park *et al.*, Nature **407**, 57 (2000).

[23] M. Koleini and M. Brandbyge, Beilstein Journal of Nanotechnology **3**, 589 (2012).

[24] N. Néel, L. Limot, J. Kröger, and R. Berndt, Phys. Rev. B **77**, 125431 (2008).

[25] G. Schull, T. Frederiksen, A. Arnau, D. Sanchez-Portal, and R. Berndt, Nat. Nanotechnol. **6**, 23 (2011).

[26] G. Schulze, K. J. Franke, and J. I. Pascual, New Journal of Physics **10**, 065005 (2008).

[27] J. Bardeen, Phys. Rev. Lett. **6**, 57 (1961).

[28] L. Gross *et al.*, Phys. Rev. Lett. **107**, 086101 (2011).

[29] Q. Zhong, D. Inniss, K. Kjoller, and V. Elings, Surface Science Letters **290**, L688 (1993).

[30] L. Gross *et al.*, Nat. Chem. **2**, 821 (2010).

[31] M. Nicklaus, A. Pignolet, C. Harnagea, and A. Ruediger, Appl. Phys. Lett. **98**, 162901 (2011).

[32] Z. X. Sun, M. P. Boneschanscher, I. Swart, D. Vanmaekelbergh, and P. Liljeroth, Physical Review Letters **106**, 046104 (2011).

[33] F. J. Giessibl, S. Hembacher, H. Bielefeldt, and J. Mannhart, Science **289**, 422 (2000).

[34] M. Herz, F. J. Giessibl, and J. Mannhart, Phys. Rev. B **68**, 045301 (2003).

[35] A. N. Chaika and A. N. Myagkov, Chemical Physics Letters **453**, 217 (2008).

[36] A. N. Chaika, V. N. Semenov, V. G. Glebovskiy, and S. I. Bozhko, Applied Physics Letters **95**, 173107 (2009).

[37] A. N. Chaika *et al.*, Europhysics Letters **92**, 46003 (2010).

[38] A. N. Chaika *et al.*, Applied Surface Science **267**, 219 (2013).

[39] J. Loos, Advanced Materials **17**, 1821 (2005).

[40] J. H. A. Hagelaar, C. F. J. Flipse, and J. I. Cerda, Physical Review B **78**, 161405 (2008).

[41] A. D. Gottlieb and L. Wesoloski, Nanotechnology **17**, R57 (2006).

[42] N. Moll, L. Gross, F. Mohn, A. Curioni, and G. Meyer, New Journal of Physics **14**, 083023 (2012).

[43] C. A. Wright and S. D. Solares, Journal of Physics D: Applied Physics **46**, 155307 (2013).

[44] F. Mohn, B. Schuler, L. Gross, and G. Meyer, Applied Physics Letters **102**, (2013).

[45] S. Grimme, J. Chem. Phys. **124**, 034108 (2006).

[46] R. E. Schlier and H. E. Farnsworth, J. Chem. Phys. **30**, 917 (1959).

[47] K. Takayanagi, Y. Tanishiro, S. Takahashi, and M. Takahashi, Surface Science **164**, 367 (1985).

[48] K. D. Brommer, M. Needels, B. E. Larson, and J. D. Joannopoulos, Physical Review Letters **68**, 1355 (1992).

[49] M. A. Lantz *et al.*, Science **291**, 2580 (2001).

[50] A. M. Sweetman, Unpublished STM/AFM images .

[51] P. J. Moriarty, Surface Science Reports **65**, 175 (2010).

[52] K. J. Franke and J. I. Pascual, Journal of Physics-condensed Matter **24**, 394002 (2012).

[53] J. A. Gardener, G. A. D. Briggs, and M. R. Castell, Physical Review B **80**, 235434 (2009).

[54] G. Li *et al.*, Applied Physics Letters **100**, 013304 (2012).

[55] S. I. Bozhko *et al.*, Physical Review B **84**, 195412 (2011).

[56] L.-L. Wang and H.-P. Cheng, Phys. Rev. B **69**, 165417 (2004).

[57] T. Bohler, A. Edtbauer, and E. Scheer, Physical Review B **76**, 125432 (2007).

[58] X. H. Lu, M. Grobis, K. H. Khoo, S. G. Louie, and M. F. Crommie, Physical Review Letters **90**, 096802 (2003).

[59] S. W. Cho *et al.*, Synthetic Metals **157**, 160 (2007).

[60] M. Casarin *et al.*, Journal of Physical Chemistry C **111**, 9365 (2007).

[61] J. G. Hou *et al.*, Physical Review Letters **83**, 3001 (1999).

[62] R. Rurali, R. Cuadrado, and J. I. Cerda, Phys. Rev. B **81**, 075419 (2010).

[63] X. L. Du *et al.*, Applied Physics Letters **97**, 253106 (2010).

[64] I. D. Hands, J. L. Dunn, and C. A. Bates, Phys. Rev. B **81**, 205440 (2010).

[65] B. W. Heinrich, M. V. Rastei, D. J. Choi, T. Frederiksen, and L. Limot, Phys. Rev. Lett. **107**, 246801 (2011).

[66] I. D. Hands, J. L. Dunn, and C. A. Bates, Phys. Rev. B **82**, 155425 (2010).

[67] J. L. Dunn, A. J. Lakin, and I. D. Hands, New J. Phys. **14**, 083038 (2012).

[68] A. Lakin, H. Alqannas, and J. Dunn, Journal of Physics: Conference Series **428**, 012001 (2013).

[69] A. Wachowiak *et al.*, Science **310**, 468 (2005).

[70] Y. Y. Wang *et al.*, Physical Review Letters **99**, 086402 (2007).

[71] Y. Y. Wang, R. Yamachika, A. Wachowiak, M. Grobis, and M. F. Crommie, Nature Materials **7**, 194 (2008).

[72] J. I. Pascual *et al.*, Chem. Phys. Lett. **321**, 78 (2000).

[73] C. P. Huang, C. C. Su, and M. S. Ho, Applied Surface Science **254**, 7712 (2008).

[74] F. Loske, P. Rahe, and A. Kuhnle, Nanotechnology **20**, 264010 (2009).

[75] C. Chiutu, A. Stannard, A. M. Sweetman, and P. Moriarty, Chemical Communications **47**, 10575 (2011).

[76] R. Pawlak, S. Kawai, S. Fremy, T. Glatzel, and E. Meyer, Journal of Physics-condensed Matter **24**, 084005 (2012).

[77] J. Tersoff and D. R. Hamann, Phys. Rev. B **31**, 805 (1985).

[78] C. J. Chen, Phys. Rev. B **42**, 8841 (1990).

[79] A. Stone, *The Theory of Intermolecular Forces* (OUP Oxford, 2013).

[80] J. E. Sader and S. P. Jarvis, Applied Physics Letters **84**, 1801 (2004).

[81] M. B. Hall and R. F. Fenske, Inorganic Chemistry **11**, 768 (1972).

[82] R. Hoffmann, The Journal of Chemical Physics **39**, 1397 (1963).

[83] R. S. Mulliken, C. A. Rieke, D. Orloff, and H. Orloff, Journal of Chemical Physics **17**, 1248 (1949).

[84] C. C. J. Roothaan, Journal of Chemical Physics **19**, 1445 (1951).

[85] D. Willock, *Molecular Symmetry* (Wiley, 2009).

[86] L. Hallam, *Theory of Jahn-Teller effects in orbital triplet systems*, PhD thesis, University of Nottingham, 1991.

[87] J. L. Dunn, Journal of Physics-condensed Matter **1**, 7861 (1989).

[88] D. Lide, *CRC Handbook of Chemistry and Physics, 85th Edition* (Taylor & Francis, 2004).

[89] E. Clementi and D. L. Raimondi, Journal of Chemical Physics **38**, 2686 (1963).

[90] H. A. Skinner and H. O. Pritchard, Trans. Faraday Soc. **49**, 1254 (1953).

[91] C. Chiutu *et al.*, Phys. Rev. Lett. **109**, 079901 (2012).

[92] Q. Qiu, *Studies of vibronic interactions in tetrahedral and icosahedral systems*, PhD thesis, University of Nottingham, 1998.

[93] C. Chancey and C. O'Brien, *The Jahn-Teller Effect in C60 and Other Icosahedral Complexes* (Princeton University Press, 1997).

[94] N. Hauptmann *et al.*, New J. Phys. **14**, 073032 (2012).

[95] L. Gross, Nat. Chem. **3**, 493 (2011).

[96] E. Clementi, D. L. Raimondi, and W. P. Reinhardt, The Journal of Chemical Physics **47**, 1300 (1967).

[97] L. A. Girifalco, J. Phys. Chem. **95**, 5370 (1991).

[98] P. Rahe *et al.*, Review of Scientific Instruments **82**, (2011).

[99] G. Schull and R. Berndt, Physical Review Letters **99**, 226105 (2007).

[100] J. Cervenka and C. F. J. Flipse, Nanotechnology **21**, 065302 (2010).

[101] M. Cummings *et al.*, Surface Science **605**, 72 (2011).

[102] J. A. Theobald, N. S. Oxtoby, N. R. Champness, P. H. Beton, and T. J. S. Dennis, Langmuir **21**, 2038 (2005).

[103] H. S. Alqannas, A. J. Lakin, J. A. Farrow, and J. L. Dunn, Physical Review B **88**, 165430 (2013).

[104] C. J. Chen, Journal of Vacuum Science & Technology A: Vacuum, Surfaces, and Films **9**, 44 (1991).